Biomechanics of Spinal Manipulation Using a Cat Model

Allyson Ianuzzi

Dissertation Proposal
Department of Biomedical Engineering
Advisor: Partap Khalsa

Dissertation Committee: Dr. Stefan Judex (chair), Dr. Yi-Xian Qin, Dr. Glenn Gaudette, Dr. Joel Pickar

Abstract

Spinal manipulation (SM) is an effective treatment for low back pain, though the mechanisms by which it is effective remain elusive. It has been theorized that SM initiates a beneficial neurophysiological response by stimulating mechanically sensitive neurons in the facet joint capsule (FJC). The neurophysiological response during SM-like loads has been investigated in cat models, while the biomechanics of SM have been studied mostly in humans during in vivo or cadaveric studies. These data are not easily related because little is known about how the biomechanical response of the human lumbar spine during SM relates to that of the cat. The specific aim of the proposed dissertation is to determine the mathematical relationship between the mechanical states of human and cat lumbar FJCs during SM. Cat cadaveric spines will be mechanically tested during simulated physiological motions and SM. A mathematical relationship will be established to relate cat lumbar FJC strain magnitudes to those obtained from prior studies in human cadaveric lumbar spines. Using this scaling relationship, the neurophysiological data obtained from cat models in future studies can be used to estimate how biomechanically similar motions would affect human FJC afferents.

List of Figures

Table of Contents

A. Specific Aims

Lumbar spinal manipulation is an effective treatment for low back pain (LBP) (Bronfort, 1999), although the mechanisms by which it is effective remain elusive (Bronfort, 1999). It has been theorized that high velocity, low amplitude (HVLA) spinal manipulation (SM) induces a beneficial neurophysiological effect by stimulating mechanically sensitive neurons in the facet joint capsule (FJC) (Pickar, 2002). In feline lumbar spines, FJC and paraspinal mechanoreceptors respond in a graded fashion to physiological and SM-like loading (Pickar and McLain, 1995; Pickar and Wheeler, 2001). In human spines, applied loads during SM have been characterized in cadaveric (Gal *et al.*, 1994; Gal *et al.*, 1997) and in vivo (Cramer *et al.*, 2002; Lee and Evans, 1997; Nathan and Keller, 1994; Triano and Schultz, 1997) studies. The data from human and cat lumbar spine studies are difficult to compare or integrate because it is unknown how the loads applied to the cat during neurophysiological studies are related to the biomechanical response of the human spine during SM.

The long-term goal of the proposed study is to determine the FJC's role in the proposed beneficial neurophysiological effect of SM. Because a majority of the experiments that investigate the neurophysiology of SM are conducted in cat models, a better understanding of the relationship between the biomechanics of cat and human lumbar spines is required to achieve this goal. The short-term goal of the study is to determine a scaling relationship between the biomechanics of the human and cat lumbar spines during SM. This relationship will allow for the estimation of how human FJC afferents might respond during SM, which will provide a framework for the generation of hypotheses aimed at determining the FJC's specific role during SM. To that end, the specific aim of the project is as follows:

Specific Aim: Determine the mathematical relationship between the mechanical states of human and cat lumbar facet joint capsules during spinal manipulation.

Hypothesis 1. A linear relationship exists between the physiological limit for vertebral joint torque for cat and human cadaveric lumbar spines.

Hypothesis 2. During physiological motions, the L_{6-7} FJC strains in cat cadaveric lumbar spines are linearly scalable to the L_{4-5} FJC strains in human cadaveric lumbar spines.

Hypothesis 3. During simulated SM, the L_{6-7} FJC strains in cat cadaveric lumbar spines will be linearly scalable to the L_{4-5} FJC strains in human cadaveric lumbar spines.

B. Background and Significance

SM is a popular treatment for LBP, yet the underlying physiological mechanisms are unclear. In a recent survey on patient patterns and perceptions of care (Wolsko *et al.*, 2003), patients experiencing back pain sought conventional therapy (such as physical therapy) more often than chiropractic therapy (37% versus 20%, respectively). However, patients who sought chiropractic therapy more often viewed the treatment as "very helpful" (61% versus 27% seeking conventional therapfy) (Wolsko *et al.*, 2003). Recent meta-analyses of clinical trials indicate that SM was an effective treatment for LBP with rare incidence of adverse effects (Bronfort, 1999; Assendelft *et al.*, 2003; Koes *et al.*, 1996). However, little is known about the physiological mechanisms by which SM is effective. It has been theorized that SM induces a beneficial neurophysiological effect by stimulating FJC mechanically sensitive neurons (Pickar, 2002).

The biomechanics of HVLA SM have been studied in vivo (Hessell *et al.*, 1990; Triano, 2000). A patient is positioned side-lying with varying degrees of pelvic rotation. The practitioner administers a preload force targeted on a single vertebral process (e.g.,

lumbar mamillary process) to rotate the vertebra near the limits of its active range of motion. Then, an impulse load is applied such that the resultant displacement does not exceed the passive range of motion of the joint (Triano, 2000). The preload force transmitted through the trunk approximates 100 N, and the transmitted force during the impulse, which is maintained for approximately 200 ms, ranges from 50 to 400 N (Triano and Schultz, 1997; Hessell *et al.*, 1990; Harms and Bader, 1997; Harms *et al.*, 1999). SM induced relatively small intervertebral motions in vivo; mean intervertebral angles and translations ranged from 0.13-0.9° and 0.25-1.62 mm, respectively, in response to a posteroanterior load (Nathan and Keller, 1994).

The FJC is loaded during SM; the application of a HVLA SM can result in “gapping” of the facet joints (Cramer *et al.*, 2002), and the audible “crack” that often accompanies HVLA SM is believed to originate from a rapid distention of the facet joint surfaces causing cavitation within the synovial fluid (Brodeur, 1995). In a human cadaveric study, FJC strain magnitudes during SM were at the high end of the range that occurred during physiological motions ((Ianuzzi and Khalsa, 2004), see Section C.2 & Appendix II). The human FJC is innervated with mechanoreceptors and mechano-nociceptors (Cavanaugh *et al.*, 1989), and FJC strains (or stresses) during SM may be sufficient to stimulate these neurons. Mechanoreceptors innervating paraspinal tissues in cats responded in a graded fashion to the direction of an innocuous load applied to a lumbar vertebra (Pickar and McLain, 1995). Simulated SM can either increase or decrease the discharge of neurons innervating paraspinal tissues (Pickar and Wheeler, 2001). Large strains during SM may stimulate FJC mechano-nociceptors. Alternatively, high FJC strain rates could provide a novel stimulus for FJC mechanoreceptors (Avramov *et al.*,

1992).

Though the data from human spines and cat models provide useful information that characterizes the biomechanics and neurophysiology of SM, it is unknown how the biomechanical response of the human spine during SM is related to that of the cat lumbar spine. The purpose of the proposed study is to develop a scaling relationship so that the data obtained by others during on-going neurophysiological studies of the cat spine during vertebral loading (PI: J.G. Pickar, D.C., Ph.D. – funded by NCCAM/NIH at the Palmer Center for Chiropractic Research) can be extrapolated to the human.

C. Preliminary Studies

The methods described in this proposal are similar to those used in the advisor's (Khalsa) laboratory for the mechanical testing of human lumbar spines. The following sections briefly review the pertinent published and preliminary studies regarding: **C.1 Human lumbar FJC strains during physiological motions** ((Ianuzzi *et al.*, 2004), see Appendix I), **C.2 Human lumbar FJC strains during simulated spinal manipulations** ((Ianuzzi and Khalsa, 2004), see Appendix II), **C.3 Determination of cat lumbar spine torque-limit during axial rotation**, **C.4 Determination of human lumbar spine torque-limit during extension**, and **C.5 Validation of three-dimensional image correlation software**.

C.1. Human lumbar facet joint capsule strains during physiological motions (not included in this dissertation).

Human cadaveric lumbar spine specimens (n=7) were actuated at T_{12} during displacement-controlled physiological motions of extension, flexion, and lateral bending (Fig. 1). Biaxial inclinometers were attached to the anterior aspects of adjacent vertebral bodies to measure intervertebral angle (IVA). Capsule plane strains (Lagrangian large

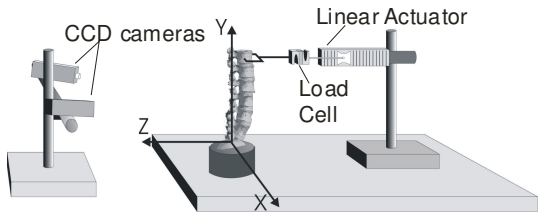

Figure 1. Lumbar spine specimens were mechanically tested during displacement-controlled physiological motions. Two CCD cameras tracked markers on facet joint capsule surfaces for plane strain measurements.

strain formulation) were measured by optically tracking, with two CCD cameras, the displacements of infrared reflective markers (1.16 mm radius) glued to capsule surfaces. Principal strains E1 and E2 (whose orientations were closest to the X- and Y-axis, respectively) were organized as maximum and minimum strains (denoted $\hat{E}_1$ and $\hat{E}_2$, respectively). Statistical differences ($p<0.05$) in moment, IVA, and strain were assessed across joint levels and displacement using ANOVA with post-hoc Tukey tests and pair-wise comparison of linear regression lines (CLRL, $\alpha=0.05$).

Results: Joint moments and IVAs increased monotonically with increasing global displacements (Fig. 2A & B, respectively). Mean joint moment-displacement and IVA-displacement relationships were highly correlated ($R^2>0.90$) during all motion types. During extension and flexion, FJC principal strain magnitudes increased with increasing global displacements (Fig. 2C). During extension, mean $\hat{E}_2$ was larger in absolute magnitude at the L_5-S_1 capsules compared to the more cephalic joint capsules (CLRL, $p<0.05$). During flexion, $\hat{E}_1$ was significantly larger at the more caudal joint capsules

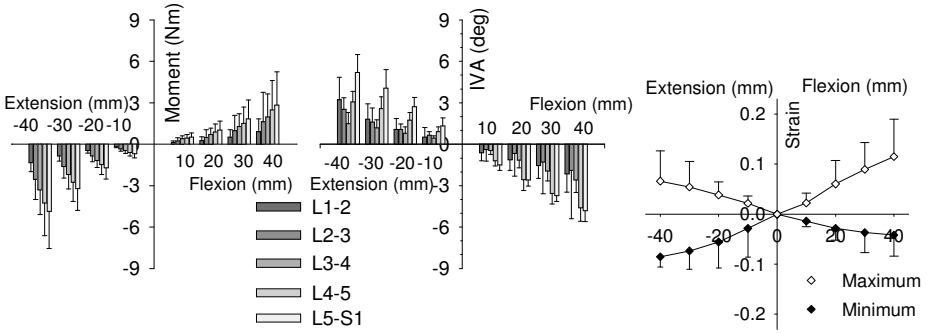

Figure 2. Moment, IVA, and strain during extension and flexion. **A)** Joint moments and **B)** intervertebral angles (IVA) increased monotonically with increasing displacements during physiological motions of extension and flexion. **C)** Facet joint capsule strain magnitudes increased in absolute magnitude with increasing displacements during physiological motions of extension and flexion (L5-S1 shown). n=7.

compared to the more cephalic capsules (CLRL, $p<0.05$). FJC strains during left and right lateral bending exhibited mirror symmetry, though they were more complex. The types of motion that generated the largest IVA were the same motion types that created the largest principal strains at all joints.

Discussion: FJC strain magnitudes were substantial (over 20% from full extension to full flexion) during physiological motions. Unlike other joint capsules during physiological motions (e.g., knee (Khalsa and Grigg, 1996)), the FJC is partially unloaded only at certain physiological motion limits (e.g., full extension). Given that capsule mechanoreceptors have relatively low thresholds (~5 kPa) (Khalsa *et al.*, 1996) and their neural responses are linearly proportional to global motions (Khalsa and Grigg, 1996), it is likely that human FJC afferents are stimulated during large portions of the physiological ranges of motion (ROMs) of the spine. Assuming that FJC mechanoreceptors do respond to lumbar ROMs, then the strain data also suggest a possible mechanism by which these neurons could encode motion. Specifically, given the relative symmetry of FJC strains, the neural population response of stimulated mechanoreceptors could unambiguously differentiate between motions and their relative magnitudes. The distinct patterns in IVA and FJC strains during physiological spine motions provide biomechanical evidence supporting the theory that the FJC could function proprioceptively.

C.2. Human lumbar facet joint capsule strains during simulated HVLA SM.

Human cadaveric lumbar spine specimens (n=7) were mechanically tested during displacement-controlled physiological motions of extension, flexion, and lateral bending using methods described previously ((Ianuzzi *et al.*, 2004), see Section C.1 & Appendix

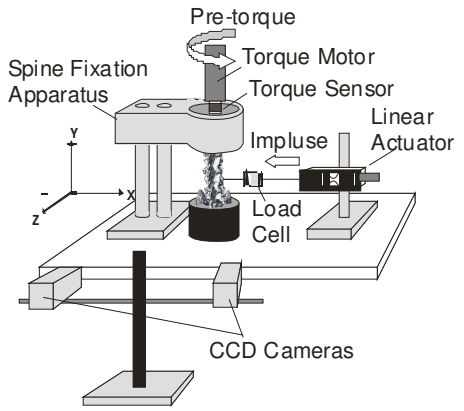

Figure 3. Impulse loading experimental setup. Lumbar spine specimens were tested during axial rotations using a torque motor oriented along the Y-axis. The setup was modified to test specimens during simulated spinal manipulations using the linear actuator to apply a load to the vertebra of interest. Two CCD cameras tracked the displacements (in 3D) of markers placed on the facet joint capsule surfaces and the transverse processes.

I). Then, specimens were potted at T_{12} and tested during displacement-controlled motions of axial rotation, within the physiological range, using a torque motor that was attached to the epoxy at T_{12} (Fig. 3). Next, SM was simulated using a variety of pre-torque magnitudes (applied at T_{12} to simulate patient positioning; 0, 5, and 10 Nm), manipulation site (L_3, L_4, or L_5), and impulse speed (5, 20, and 50 mm/s). SM was simulated using a linear actuator that simultaneously caused translation and rotation of the vertebra of interest (Fig. 3). Vertebral kinematics were assessed in three dimensions (3D) by optically tracking the displacements of sets of three non-collinear infrared reflective markers attached to the transverse processes, and the vertebral motions were computed with six degrees of freedom (DoF) (Soderkvist and Wedin, 1993). FJC strains were measured as described previously ((Ianuzzi *et al.*, 2004), see Section C.1 & Appendix I). Significant differences in load were assessed using 3-way ANOVA with post-hoc Tukey tests ($\alpha = 0.05$; factors: impulse speed, manipulation site, pre-torque magnitude; SigmaStat V. 2.03, SPSS, Inc.). As preliminary analyses indicated that impulse speed did not have a significant effect on FJC strain or vertebral motion, significant differences were detected using 2-way ANOVA ($\alpha=0.05$; factors: manipulation site, pre-torque magnitude; SigmaStat V. 2.03, SPSS, Inc.).

Results: The mean loads that developed during simulated SM (range: 100-250 N)

were within the range transmitted in vivo (Triano and Schultz, 1997). Load magnitudes significantly increased inferiorly, and larger pre-torque magnitudes resulted in significantly larger loads (ANOVA, $p<0.05$). Vertebral translations occurred predominantly in the direction of the applied impulse (-X-axis) and did not vary significantly with pre-torque magnitude or manipulation site (ANOVA, $p>0.05$). Site-specific manipulations produced systemic biomechanical responses in the lumbar spine; vertebral rotations (Fig. 4A) were induced distal to the manipulation site. L_3, L_4, & L_5 Y-axis rotations were significantly larger with 5 & 10 Nm versus 0 Nm pre-torque (ANOVA $p<0.05$). FJC strains were induced distal to the manipulation site (Fig. 4B), and there were no significant differences in $\hat{E}_1$ or $\hat{E}_2$ at a given FJC with manipulation site. At all joint levels, SM produced FJC strain magnitudes that were within the range that occurred during physiological motions.

Discussion: FJC strain magnitudes were within the range that occurred during physiological motions. As strain magnitudes during SM were within the range that occurred during physiological motions (albeit the high end of the range), SM was biomechanically "safe". The capsule loading that occurs during SM is likely to provide a mechanical stimulus that is sufficient to stimulate capsule mechanoreceptors.

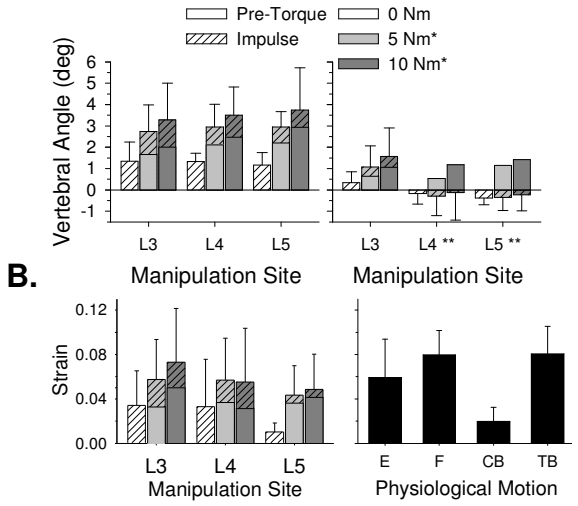

Figure 4. Vertebral kinematics and facet joint capsule (FJC) strains during simulated spinal manipulations (SM). Vertebral rotations (**A**, L3 Y-axis, left; Z-axis, right) during SM were induced distal to the manipulation site. FJC strains were also induced distal to the manipulation site (**B**, left), and strain magnitudes were within the range that occurred during physiological motions (**B**, right; E-extension; F-flexion; CB-compressive bending; TB-tensile bending). *Significantly different from 0 Nm. **Significantly different from L3.

However, given the strain magnitudes and that SM in vivo usually does not cause acute pain (Bronfort, 1999), it is also likely that SM provides a stimulus that is sub-threshold for FJC mechano-nociceptors. The high strain rates that occur during SM probably induce a “non-physiological” pattern of mechanoreceptor firing, which may contribute to the theorized beneficial neurophysiological effect of SM. The data suggest that successful management of patients with LBP using SM may not require precise segmental specificity, as strain magnitudes at a given FJC during SM did not depend upon manipulation site.

C.3. Determination of cat lumbar spine torque-limit during axial rotation.

Cat lumbar spines specimens (n=6) were mechanically tested to failure during axial rotation. Spine specimens were procured 1 hour post mortem and dissected free of superficial tissues while keeping the interspinous, capsular, and the posterior & anterior longitudinal ligaments intact. The experimental setup for testing the cat spines during axial rotation was similar to that used for human spines ((Ianuzzi and Khalsa, 2004), see Appendix II). As the cat lumbar spine has 7 vertebrae, the cat spines were coupled to the torque motor at the L_2 vertebra (i.e., the vertebral level corresponding with T_{12} in human spines).

The first trial consisted of 10 cycles to a peak displacement (5º at 5º/s). Peak displacement was incremented 5º for each subsequent trial, and the mean peak moment (measured by the torque transducer along the Y-axis) for the last five cycles contributed to the moment-displacement relationship used to determine stiffness and yield point (see below). Once failure occurred (indicated by a decrease in moment with an increase in displacement), the spine specimen was tested at two additional peak

displacement magnitudes.

Joint moment (L_{5-6} through L_7-S_1) was estimated as the moment measured by the torque sensor at L_2, and L5, L6, & L7 vertebral kinematics were measured as described previously ((Ianuzzi and Khalsa, 2004), Section C.2). Whole spine stiffness (Fig. 5) and vertebral stiffness at L_5, L_6, & L_7 were computed as the slope of the linear portion of the moment-torque motor displacement and moment-vertebral angle relationships, respectively. Joint stiffnesses at L_{5-6} through L_7-S_1 were computed as the slope of the linear portion of the respective moment-IVA relationships. A line parallel to the linear portion of the relationship used to determine whole spine stiffness, which was offset by 5% from the linear portion, was computed; its intersection with the moment-displacement plot was the yield point (Fig. 5; (Gunning *et al.*, 2001)). A conservative torque-limit was defined as the 10th percentile of the yield point.

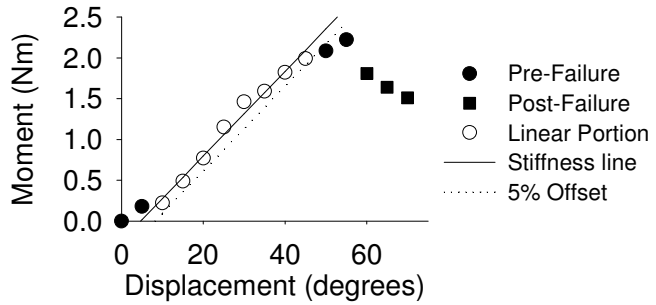

Figure 5. Whole cat spine stiffness during the test to failure in axial rotation was computed as the slope of the linear portion of the moment-displacement relationship. This line was offset 5% of the total displacement, and its intersection with the moment-displacement plot was the yield point.

Results: During axial rotation, mean yield point for cat lumbar spines was 2.29 ± 0.63 Nm, and torque-limit was 1.42 Nm. Similar to human spines (Panjabi *et al.*, 1994), cat lumbar spines underwent coupled intervertebral motions during axial rotation (Fig. 6). About all three axes, IVAs at L_{5-6} were highly variable and relatively small in absolute magnitude. At L_{6-7} and L_7-S_1, IVA occurred predominately about the Y-axis, and Y-axis IVA increased in magnitude with increasing displacements.

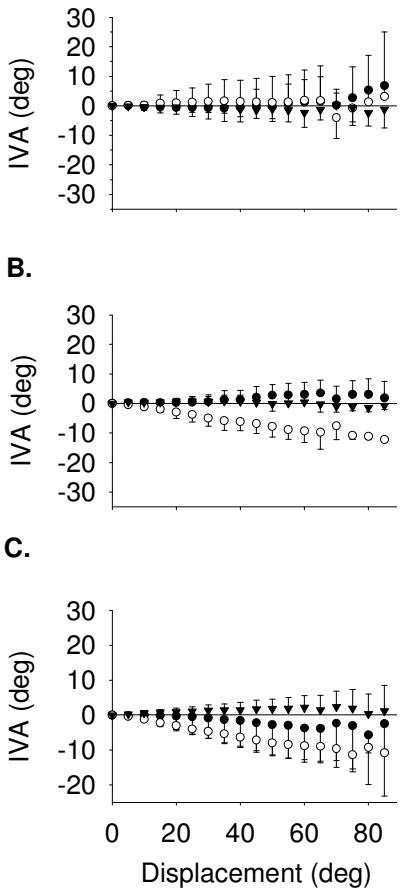

Figure 6. Intervertebral angles (IVA) at **A**. L5-6 **B**. L6-7 and **C**. L7-S1 of cat lumbar spine specimens during mechanical testing to failure in axial rotation (-Y-axis rotation). Mean and standard deviations shown.

There were significant differences among vertebral stiffness magnitudes (ANOVA, p = 0.007). Though whole spine stiffness appeared smaller in magnitude compared to vertebral stiffness at the more caudal vertebrae, these differences were only significant at L_7 (Tukey, $p < 0.05$; Fig. 7). Joint stiffness magnitudes at L_{5-6}, L_{6-7}, and L_7-S_1 were similar in magnitude and did not differ significantly (Fig. 7; ANOVA, p = 0.795).

Discussion: A conservative torque-limit of 1.42 Nm was computed for mechanical testing of cat lumbar spines during axial rotation. This torque-limit will be used in future studies, the aim of which is to measure FJC strains during axial rotation within the sub-failure range (Section D.2.2).

The 1.42 Nm torque-limit computed for cat lumbar spines during axial rotation is smaller in magnitude compared to the 15 Nm limit estimated by Panjabi et al. for human lumbar spines (Panjabi *et al.*, 1994). This may be due to anatomical differences between the two species. For instance, the lumbar facets restrict

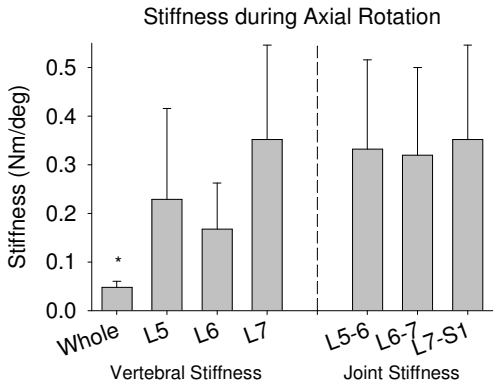

Figure 7. Vertebral stiffness (left) of cat lumbar spine specimens during axial rotation was smaller in magnitude at the point of load application (L2) compared to the more caudal levels. Joint stiffness magnitudes (right) at the caudal joint levels were similar in magnitude. *Significantly smaller than L7 (Friedman's test w/Tukey, p<0.05).

intervetebral motions during axial rotation in both species, but cat lumbar vertebrae contain accessory processes lateral to the facets. The accessory processes present in the cat lumbar spine may result in different biomechanics during these motions, causing different structures to fail. The difference in torque-limit may also be due to differences in yield strength of the paraspinal tissues that fail during axial rotation. An extension of this work will be aimed at determining the scaling relationship between torque limits of cat and human lumbar spines (Section D.2.1).

C.4 Determination of human lumbar spine torque-limit during extension.

Human lumbar spine specimens (n = 6) were mechanically tested to failure during extension. Spine specimens were procured within 24 hours post mortem and dissected free of superficial tissues while keeping the interspinous, capsular, and the posterior & anterior longitudinal ligaments intact. Prior to the test to failure, specimens were used in another study where they were subjected to 20 minutes of static lumbar flexion. Specimens were prepared and tested using the same experimental setup described for the testing of human lumbar spine specimens during physiological motions ((Ianuzzi *et al.*, 2004), see Sections C.1 and Appendix I).

The kinematics of the three most caudal vertebrae (L_3 - L_5) were measured as described previously ((Ianuzzi and Khalsa, 2004), Section C.2). Joint moment was computed as the product of the load (measured at T_{12} by the load cell) and the moment arm (i.e., the distance between the point of load application and the center of the FJC). Joint and whole-spine stiffnesses were determined as the slope of the linear portion of the joint moment-IVA & load-global displacement relationships, respectively. Torque-limit was defined conservatively as the 10^{th} percentile of the largest moment (at L_5-S_1,

computed as product of L_5-S_1 moment arm and force at T_{12}).

After the spines failed, they were re-tested during extension, flexion, and lateral bending. Whole spine and joint stiffness of the failed human spines during extension, flexion, and lateral bending were compared to the respective values obtained for intact spines in a prior study (Little *et al.*, 2004) to determine whether failure during extension significantly affected stiffness during other motions (Mann-Whitney Rank Sum Test, $\alpha = 0.05$; SigmaStat V. 2.03, SPSS, Inc.).

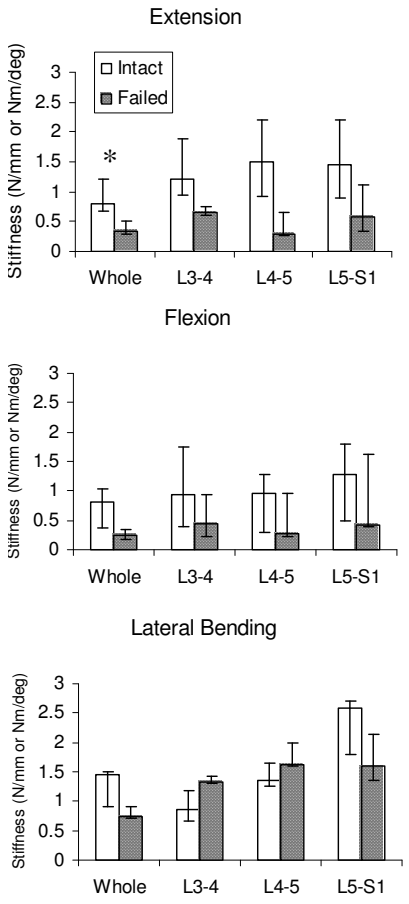

Figure 8. Human spine stiffness during physiological motions before and after failure in extension. During extension and flexion, whole spine and joint stiffness magnitudes of human lumbar spines failed in extension were smaller in magnitude compared to those of intact spines. During lateral bending, joint and whole-spine stiffnesses intact and failed spines were similar in magnitude. *Intact vs. failed significantly different, Mann-Whitney, $p<0.05$. Median, 25th, and 75th percentiles shown.

Results: During extension, the yield point for the human spines was 116.4 ± 16.5 N. Mean torque at the yield point at L_5-S_1 (i.e., the largest moment) was 20.3 ± 2.3 Nm. The torque-limit, which was computed as the 10th percentile of the yield point at L_5-S_1, was 17.8 Nm.

Joint and whole spine stiffness magnitudes of the failed human spine specimens did not differ substantially from those obtained from intact spines (Fig. 8). During lateral bending, median whole-spine and joint stiffness magnitdes of the failed specimens were not significantly different from those of intact spines (Mann-Whitney, Whole spine: $p = 0.534$; L_{3-4}: $p = 0.174$; L_{4-5}: $p = 0.725$; L_5-S_1: $p = 0.414$). Although median stiffness during flexion appeared smaller in magnitude post-failure

compared to the intact spines, these differences were not significant (Whole spine: $p = 0.366$; L_{3-4}: $p = 0.428$; L_{4-5}: $p = 0.308$; L_5-S_1: $p = 0.689$). The apparent differences were likely due to the fact that the failed specimens were subjected to 20 minutes of static lumbar flexion prior to failure. Median whole-spine stiffness of the failed specimens during extension was significantly smaller in magnitude than whole-spine stiffness of the intact specimens (Mann-Whitney, $p = 0.025$). Although median joint stiffness magnitudes during extension for the failed specimens appeared smaller than for intact specimens, these differences were not significant (L_{3-4}: $p = 0.071$; L_{4-5}: $p = 0.119$; L_5-S_1: $p = 0.321$).

Discussion: Prior observations by Panjabi et al. suggest that during static, torque-controlled testing of lumbar spines, torques larger than 15 Nm result in load-displacement curves suggestive of soft-tissue damage (Panjabi *et al.*, 1994). This is smaller in magnitude than the torque-limit computed in the current study (17.8 Nm). The data suggest that compared to torque-controlled testing, a higher torque limit can be used during displacement-controlled testing of lumbar spines in extension. This is most likely because of the inherent viscoelasticity of the spine, which “creeps” under a constant load, but “relaxes” under constant displacement. It is also likely that during displacement-controlled testing the torque-limit during other motion types (lateral bending, flexion, and axial rotation) is larger as well. Future studies will include the determination of torque-limit for human spines during these motion types (Section D.2.1).

Failure of human lumbar spines in extension caused a significant decrease in spine stiffness during extension, though stiffnesses during other motion types (flexion and

lateral bending) were not significantly altered. This indicated that failure in extension may not affect the structures restricting these motions. The results of this study also suggest that the human spine specimens that were failed in extension can be re-tested to determine the yield point of human spines during lateral bending. Re-testing the human lumbar spines used in this study was of interest because fresh-frozen, cadaveric human spines are relatively expensive and difficult to obtain. However, it should be noted that even though the statistical analyses indicated that there were no significant differences in stiffness during lateral bending of the failed spines versus the intact spines, due to the small number of spines tested significant differences may in fact exist.

An extension of this work will include the failure of additional cat and human lumbar spines to determine yield points during flexion, extension, lateral bending, and axial rotation. The results of these studies will establish the mean torque limits for cat lumbar spines. These limits will be used during biomechanical tests of cat lumbar spines (Section D.2.2) ensure that applied loads will be within the sub-failure range. In addition, a scaling relationship between torque limits for cat and human lumbar spines will be computed (Section D.2.1).

C.4 Validation of three-dimensional image correlation software.

A custom program was written in Matlab to track the 3D displacements of subregions on a material within a region of interest (ROI). Three noncollinear markers, which defined a plane containing the ROI, were attached to a piece of cardboard covered in white paper. Axis orientation of the object space coordinate system chosen to be the same as that used previously (Fig. 1). Stochastic patterns were created on the

material surface by randomly sprinkling the surface with silicone carbide particles and illuminating it with a fiber optic light. The cardboard was attached to a linear actuator (Model ME2130-198B, Galil, Inc., Rocklin, CA), and two high-speed, high-resolution, complementary metal oxide semiconductor (CMOS) cameras (MotionPro Model 500) with 50 mm lenses were focused on the material.

The space volume containing the material was calibrated using direct linear transform (DLT) calibration (see Section D.1.3 and Appendix III). Briefly, a calibration frame with 6 markers whose centroid locations were known was imaged by both cameras. From the calibration images, the 11 calibration parameters that related the object space coordinates and image coordinates were computed. To determine the accuracy of the calibration, the object space coordinates of the calibration markers were reconstructed using the 11 calibration parameters. Accuracy was determined as the absolute value of the difference between the known marker positions and computed marker positions. Root mean square errors (RMS) of the calibration points were computed as:

$$rms = \left[\sum_{N} (q_i - \overline{q}_i)^2 / N \right]^{1/2} \qquad \text{Eq. C4.1}$$

where N is the number of calibration points (six), q_i is the reconstructed value of the calibration point, and $\overline{q}_i$ is the actual value of the calibration point (Hatze, 1988).

Once the space volume was calibrated, the material was imaged while displacing it 5 mm in the –X direction. A custom 3D image correlation program was used to compute the 3D displacements of subregions on the material (Fig. 9 and see Section D.1.3). Briefly, for the first image from each camera, the three noncollinear markers were

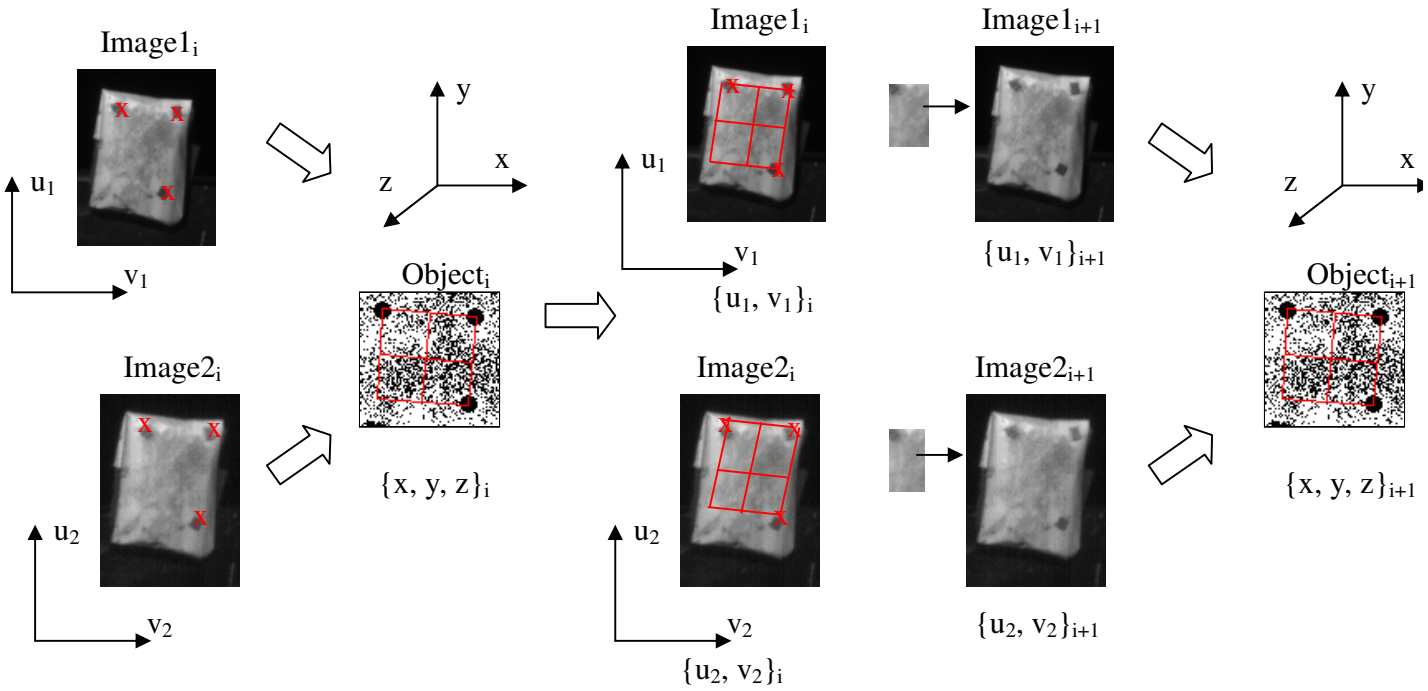

Figure 9. Three-dimensional (3D) vector displacements of material subregions were determined using a combination of direct linear transform (DLT) and image correlation functions. **A.** A region of interest (ROI) on the material was defined using three noncollinear markers which defined the surface plane of the material. Stochastic patterns were created on the material by sprinkling it with silicone carbide particles and illuminating it with a fiber optic light. The material was viewed by two cameras, generating a set of images (i = 1-n) from each camera ($\{Image1_i\}$ in u_1-v_1 coordinate system; $\{Image2_i\}$ in u_2-v_2 coordinate system). The image pixel coordinates of the marker centroids were determined for both cameras. **B.** For image i, a DLT transform was performed to compute the object space coordinates (x-y-z coordinate system) of the marker centroids from the image pixel coordinates (u_1-v_1 and u_2-v_2 coordinate systems). In object space, the ROI was defined as the plane containing the three marker centroids. This plane was then divided into 2x2 subregions, and the set of object space coordinates of the lower right corner of each subregion were determined ($\{x, y, z\}_i$). **C.** The image pixel coordinates of the lower right corner of each subregion were computed for each camera using DLT. For each camera, each subregion from image i was used as a template to determine the new pixel location of the subregion in the subsequent image (image i+1). **D.** The location of each subregion at time i+1 was computed from the image pixel coordinates obtained from each camera. The locations at time i+1 were used to compute the 3D vector displacements.

identified and each marker's 3D spatial coordinates were computed from the pixel coordinates using DLT reconstruction. The plane containing the ROI was subdivided into 4 subregions (2x2 array), and the image pixel coordinates of each subregion were computed for both cameras. For both cameras, each subregion was used as a template to identify that subregion in the subsequent image taken from that camera. The new locations (i.e., pixel coordinates) of the subregions were determined via image correlation functions in Matlab using an algorithm previously described for measuring

strain in 2D (Little *et al.*, 2003; Little and Khalsa, 2004). The new pixel coordinates of each subregion were used to compute the new 3D spatial coordinates, again using DLT reconstruction. The process was repeated for each of the subsequent images, using the previous image as the template.

Results: Accuracy of the calibration procedure was better than 0.04 mm along the X, Y, and Z-axes (mean X-axis: 0.0093 ± 0.0055 mm, mean Y-axis: 0.0260 ± 0.0193 mm, mean Z-axis: 0.0255 ± 0.0169 mm). RMS for the calibration was 0.0108, 0.0314, and 0.0297 along the X-, Y-, and Z-axis, respectively. Mean subregion peak displacement along the X-axis was 4.94 ± 0.09 mm, and mean subregion total peak displacement was 4.91 ± 0.07 mm (Fig. 10). Mean percent error ((computed – actual)/actual) was 1.93% (range: 0.24-2.65%).

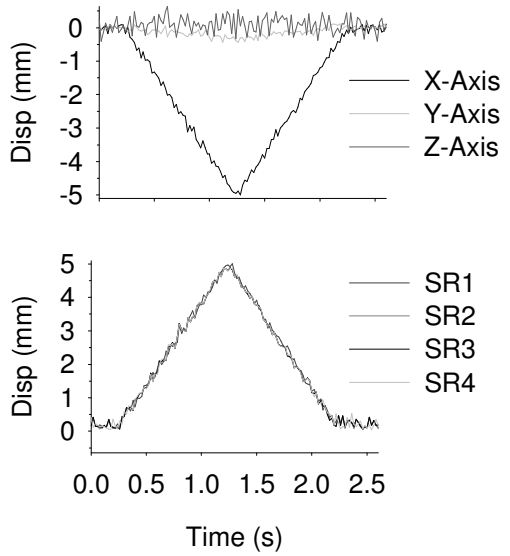

Figure 10. A rigid material was imaged while displacing it 5 mm at 5 mm/s. The displacements of four subregions (SR) on the material were computed using a custom 3D image correlation program. **A.** Representative X-, Y-, and Z-axis displacements (disp) of a single SR. Minor axis (Y,Z) displacements were relatively small in magnitude. **B.** The total displacement of all four SRs peaked at 5 mm, and the displacement-time profile of each SR closely resembled that of the actuator.

Discussion: Mean accuracy of the custom 3D image correlation software was better than 0.09 mm in the X-direction, and percent error was relatively low. RMS for the calibration were small in magnitude compared to the values reported by Hatze (Hatze, 1988) for small control point distributions (range: 0.9-3.9). The difference in RMS between the two studies may be due to the fact that the current study utilized high-resolution cameras for imaging the calibration frames (1024x1280). In the prior study, images were acquired using 16 mm

cameras, which required digitization of the images that introduced an error of ±0.1 mm. Either of which could have increased RMS in the prior study.

The custom program computed subregion displacements in 3D with relatively high accuracy along the X-axis. An extension of this work will include validation of the program using images taken of the material which displacing it along the Y-axis, and then along the Z-axis. As the X- and Y-axes are located within the plane of focus of the two cameras, it is expected that validation along the Y-axis will be similar to that of the X-axis. Although the scaling factors relating the object and image coordinates for the height and width of an object are not necessarily the same (see Appendix III), it is expected that percent error and accuracy will be similar in range. Accuracy along the Z-axis (i.e., motion in and out of the plane of focus for both cameras), however, may not be as high because large displacements along this axis may result in relatively small changes in image pixel locations. If this is the case, modifications to the current experimental setup can be made (e.g., increase focal length of the lenses) so that the object appears larger in the images and small displacements are easier to resolve.

D. Research Design and Methods

This section of the proposal is divided into two sub-sections. ***Section D.1. Research Methods*** contains the details of the experimental procedures that will be performed. ***Section D.2. Research Design*** explains the experimental approach for each of the hypotheses, as well as how the data will be analyzed and interpreted.

D.1. Research Methods

D.1.1. Preparation of human and cat cadaveric lumbar spine specimens. Human lumbar spine specimens will be obtained and prepared as previously reported (Ianuzzi *et al.*, 2004; Little *et al.*, 2004). Briefly, specimens will be shipped frozen from the

National Disease Research Interchange (Philadelphia, PA). Specimens (T_{12}-sacrum) will be unembalmed, procured within 24 hours post-mortem from donors without history of spine pathology, and free of gross pathology and scoliosis (determined by anterior-posterior and lateral view x-rays). Using an operating microscope (6x), the spines will be dissected free of all superficial musculature, including insertions of multifidi muscles (keeping the posterior ligaments intact), to expose the FJCs.

Cat lumbar spine specimens will be obtained within one hour post mortem from previously healthy adult cats (3.6 - 4.5 kg) of either sex. All cats will be treated in accordance with the Guiding Principles in the Care and Use of Animals approved by the American Physiological Society. After administration of anesthesia (gaseous mixture of oxygen (5 liters/min) and halothane (5%) in a sealed plastic induction chamber) and euthanasia (overdose of anesthetic), gross dissection will be performed to remove the lumbar spine (T_{10}-sacrum). The multifidi will be kept intact to preserve the FJCs. After removal of the spine, fine dissection will be performed to expose the FJCs as described above for the human spines.

During dissection and mechanical testing, both human and cat spine specimens will be kept moist by periodic spraying with phosphate buffered saline (PBS, pH=7.4) and by wrapping them in PBS-soaked gauze. Specimens will be oriented vertically such that the vertebral endplates of the second-most caudal joint (human: L_{4-5}, cat: L_{6-7}) are parallel to the testing surface and then potted at the sacrum using a quick-setting epoxy (Bondo ©). Specimens will then be double-bagged, stored at -80° C until ready to test, and thawed at room temperature for 12 hours prior to testing. These storage procedures do not affect the material properties of human cadaveric lumbar spine specimens

(Panjabi *et al.*, 1985), and it is assumed that they will not alter those of the cat spines.

D.1.2. Physiological loading of cat and human lumbar spine specimens. Cat and human lumbar spine specimens will be loaded vertically in an apparatus developed to emulate in vivo physiological motions of the lumbar spine (see Fig. 1 in Section C.1 & Appendix I) (Ianuzzi *et al.*, 2004; Little *et al.*, 2004). Specimens will be tested using a linear actuator consisting of a sled moving on a precision screw, which is fit with an anti-backlash nut and coupled to a torque motor (Model 317, Galil, Inc., CA) and optical encoder (MX21-559, Duncan Electronics, Tustin, CA; resolution 0.8 μm, repeatability better than 5.0 μm). A potted specimen will be locked to the testing surface and coupled to the actuator such that the actuator is horizontal at a given peak displacement. The coupling will consist of a rod in series with a force transducer (human: Model 9363-D1-50-20P1, Revere Transducers, CA; range ±220 N; cat: Model LSB200-10, Futek, Irvine, CA; range ±44 N), and it will be connected to the actuator via a low-friction universal joint. To connect the rod to the specimen creating a single degree of freedom, a U-shaped collar will be attached to the most inferior thoracic vertebral body (T_{12}) in the human spine. As cat lumbar spines have seven lumbar vertebrae (compared to five lumbar vertebrae in humans), the corresponding vertebral level in the cat spine (L_2) will be coupled to the U-shaped collar. Vertebral kinematics of the lower three lumbar vertebrae (human: L_3-L_5, cat: L_5-L_7) will be computed for all six DoF using methods described previously (Section C.2). Joint moments will be computed as the product of the applied load (measured by the force transducer) and the moment arm (distance from the point of load application to each joint).

D.1.3. Plane strain measurements. Because the FJCs in the cat spine are

substantially smaller than those in the human spine, FJC strains in the cat spine will not be measured by optically tracking markers attached to the capsule surfaces (as was done for the human spines). Instead, cat FJC strains will be measured using an extension of an optical image correlation technique recently developed in the advisor's laboratory (Section C.4, (Little *et al*., 2003; Little and Khalsa, 2004)). Briefly, stochastic patterns will be created on the FJC surface by sprinkling it with silicone carbide particles and illuminating it with a fiber optic light source. The ROI on the capsule will be identified using three small markers (1.1 mm) attached to the capsule. The markers will be arranged non-collinearly and they will identify the plane in which the ROI on the FJC is located. The capsule will be optically tracked using a system (Del Imaging Systems, LLC, Cheshire, CT) consisting of two high-speed cameras (MotionPro Model 500), frame grabbers, and data acquisition software. This system has improved spatial (1024x1280 pixels) and temporal (50-500 Hz) resolution compared to the system used for strain measurements in the human lumbar spine studies (model 50, Qualisys, Inc., Gothenberg, Sweden).

Prior to testing, the space volume will be calibrated by imaging a calibration frame with six markers having known object space coordinates (x, y, z). The calibration frame will be placed in the field of view and imaged by both cameras for one second. The image pixel coordinates of the calibration markers will be computed for both cameras as the mean position over time [camera 1: (u_1, v_1); camera 2: (u_2, v_2)]. Publicly available Matlab programs (Pribanic, 1999) were used to compute the relationship between the markers' object space coordinates (x, y, z) and image pixel coordinates (u_1, u_2, v_1, v_2). The program computes the 11 calibration parameters using a direct linear transform

(DLT) algorithm (Appendix III). Publicly available Matlab programs were also used to reconstruct 3D object space coordinates from image pixel coordinates (Reinschmidt, 1994). Using the latter program as a template, a custom program was written to compute image pixel coordinates from known object space coordinates.

During mechanical testing, a single FJC will be imaged by the two cameras (oriented at 45°). Post hoc, the images of the FJC will be processed to determine strain within the ROI (Section C.4, Fig. 9). First, using the three noncollinear markers attached to the capsule surface, the ROI will be identified in the first image of the capsule from each camera. Then, the ROI will be subdivided into an array of subregions (A x B; the optimal number of subregions will be determined in a convergence study) in the object space coordinate system. The image pixel coordinates of the subregions will be computed for each camera by performing a DLT, using the 11 DLT parameters computed during the calibration procedure.

Once the subregions are located in the first image for each camera, the stochastic pattern (i.e., formed by the silicone carbide particles) that identifies each subregion will serve as a template to identify its location in the subsequent image using optical image correlation functions in Matlab (Version 6.5, Mathworks, Inc., Natick, MA). The new object space coordinates and 3D vector displacements of the FJC subregions will be computed from these image pixel coordinates, again using DLT. The entire process (identification of the ROI and subregions in object space coordinate system, computation of image pixel coordinates for each subregion for both cameras, location of subregions in next image, computation of displacement vectors) will be repeated for all subsequent images, using the previous image as the template. FJC plane strains (ε_{xx},

ε_{yy}, and ε_{xy}) will be computed from the 3D vector displacements of each subregion using an algorithm described previously in detail ((Ianuzzi *et al.*, 2004), see Section C.1 & Appendix I)

D.1.4. Impulse loading of cat lumbar spine specimens. Cat lumbar spine specimens will be mechanically tested under displacement control to simulate the loads applied during SM. These methods will be identical to those previously described for human spine specimens ((Ianuzzi and Khalsa, 2004), see Section C.2 & Appendix II), with the exception that the L_5 through L_7 vertebrae (cat lumbar spines have 7 vertebrae) will be manipulated (to correspond with the lower three lumbar vertebrae, L_3 - L_5, tested on the human cadaveric specimens). Briefly, a torque motor (Model ME2130-198B, Galil, Inc., Rocklin, CA), in series with a torque sensor (Model TTD400, Futek, Irvine, CA), will be oriented along the Y-axis of the specimen to position the spine with increasing pre-torques (to simulate positioning with pelvic rotation). The linear actuator and force transducer described in Section D.1.2 will be coupled to the anterior portion of a single vertebra using a Synthes Small Fragment Locking Compression Plate. When displaced, the actuator will induce translation and rotation of the vertebrae and the applied load will be measured. Vertebral kinematics for all six DoF will be computed as in Section C.2, and FJC strains will be computed using the methods described in Section D.1.3. The applied moment will be computed as the product of the applied force and the distance between the point of load application and the estimated center of rotation of the vertebra (Mansour *et al.*, 2004; Pearcy and Bogduk, 1988).

D.2. Research Design

This section includes the research design of the proposed study, how the data will

be analyzed and interpreted, and the statistical tests that will be performed. The research questions and hypotheses presented in this section were designed to address the specific aim of the study: Determine the mathematical relationship between the mechanical states of human and cat lumbar facet joint capsules during spinal manipulation.

D.2.1. What is the torque-limit for physiological motions of human and cat lumbar spines?

Rationale: In biomechanical studies of human cadaveric lumbar spine specimens, Panjabi et al. reported (via unpublished observations) that moments applied to the lumbar spine that exceeded 15 Nm resulted in load-displacement relationships suggestive of soft tissue damage (Panjabi *et al.*, 1994). This torque-limit has been observed in biomechanical studies of the lumbar spine during physiological motions (Ianuzzi *et al.*, 2004; Little *et al.*, 2004; Panjabi *et al.*, 1994). In order to test cat lumbar spine specimens during physiological motions, the torque-limit for the cat lumbar spine should be determined to identify load magnitudes that could be considered within the sub-failure range. A mathematical relationship can then be established between the torque-limits for the cat and human lumbar spines.

The 15 Nm torque limit established by Panjabi for physiological motions of the human lumbar spine (Panjabi *et al.*, 1994) may not be appropriate when determining this scaling relationship; in the prior study, the human spines were tested during static, moment-controlled motions, while in the current proposed study the spine specimens will be tested cyclically during displacement-controlled motions. Preliminary data (Section C.4) demonstrated that the torque-limit during extension was larger in

magnitude during dynamic, displacement-controlled testing versus static, torque-controlled testing, and it is likely that this is also the case during other motion types. Hence it will be necessary to determine the torque limit for both human and cat lumbar spine specimens in order to establish the scaling relationship.

Hypothesis 1: A linear relationship exists between the physiological limit for vertebral joint torque for cat and human cadaveric lumbar spines.

Experimental Variables and Response Measures: Variables will include the motion itself (flexion, extension, lateral bending, and axial rotation) and global displacement (controlled at T_{12} in human spines and at L_2 in cat spines). Response measures include applied force, moment at each joint level, the maximum torque (which will always occur at the most caudal joint), and IVA (at the three most caudal lumbar joints).

Protocols: Spine specimens will be prepared and mechanically tested during flexion, extension, lateral bending, and axial rotaiton as described in Sections D.1.1 and D.1.2, respectively. During the test to failure for a given motion, a given trial will consist of 10 cycles to a peak displacement at 10 mm/s or 5°/s. The number of cycles was chosen based on prior studies on human cadaver specimens, where load equilibrium was established after approximately 5 cycles (Ianuzzi *et al.*, 2004; Little *et al.*, 2004). For cat spines, the peak displacement of the first trial will be 5 mm or 5°, and for each subsequent trial the peak displacement will be increased by 5 mm or 5°. For human spines, the peak displacement magnitudes will start at 10 mm or 5° and will be increased by 10 mm or 5° for each trial. Specimens will be tested until failure occurs (i.e., the load-displacement curves are no longer reproducible). Whole spine and joint stiffness, as well as yield point, will be computed as in Section C.3.

Sample Size Determination: Based on preliminary data from cat lumbar spines and from extensive testing of human spines (Ianuzzi *et al.*, 2004; Little *et al.*, 2004; Panjabi *et al.*, 1994), it is likely that a change in yield point on the load-displacement curves of 100 mN of force with 50 mN standard deviation can be detected with 90% power using 6 specimens (SigmaStat V. 2.03, SPSS, Inc.). Hence, to test the specimens during physiological motions of extension, flexion, lateral bending, and axial rotation, a total of 24 cat lumbar spine specimens will be tested. Preliminary studies indicated that failing the human spines in extension did not significantly affect stiffness during lateral bending (see Section C.4). As fresh-frozen, human cadaver specimens are relatively expensive and difficult to obtain, human spines will be re-used where possible. The six human spines that were failed in extension for the preliminary study will be re-tested to determine torque-limit in lateral bending. An additional six human spines will be tested to failure during flexion, and then the spines will be tested in the sub-failure range during axial rotation to determine if the stiffness of the failed spines differs significantly from intact spines. If there are no significant differences, these spines will be re-used to determine the torque-limit during axial rotation. Hence it is expected that a total of 12 human lumbar spines will be tested.

Data Analysis and Interpretation: The largest moment (Nm) at the yield point for each specimen will be computed by multiplying the yield point (N) by the moment arm for the most caudal joint (m). The mean and the 10th percentile for the moments across all specimens will be calculated for each motion. A conservative torque limit for each motion will be taken as the 10th percentile.

The scaling relationship will take the general form: $PL_{Ci} = f(M_C/M_H, PL_{Hi})$, where PL is

the physiological limit of the motion i, M is the mass, and the subscripts C and H designate cat and human data, respectively. An appropriate relationship will be determined using the method of incremental sum of squares (Glantz and Slinker, 2004). Briefly, the scaling factor for a linear fit will be determined using multiple linear regression analysis (Glantz and Slinker, 2004). Then, a higher order term will be added to the relationship and its coefficient tested to determine whether it is significantly different from zero. If the new coefficient is significantly different from zero, then the higher order term significantly contributes to the relationship; addition of higher order terms will continue until the new coefficient is not significantly different from zero (i.e., the new term does not significantly contribute to the relationship) (Glantz and Slinker, 2004). Hypothesis 1 will be supported if it is possible to establish a linear relationship between the torque limit for the cat and human lumbar spines. It will not be supported if a non-linear relationship is required to explain the relationship. In either case, some scaling relationship can be established.

Once the human spines have been failed in flexion, they will be examined to determine whether stiffness of the failed specimen during axial rotation differs significantly from intact specimens (see Section C.4, Appendix II). Stiffness will be compared using unpaired t-tests (α=0.05, SigmaStat, v. 2.03; SPSS, Inc.). If there are no significant differences between stiffness of the failed spines versus the intact spines, then the specimens used to determine torque-limit during flexion will be re-tested to determine torque-limit during axial rotation. If they are significantly different, then the specimens cannot be re-tested.

Justifications and Limitations: The proposed experiments are necessary to

determine the physiological limits of the cat and human lumbar spines during displacement-controlled motions. Without knowing these limits, it will not be possible to interpret or extrapolate the strain data obtained from future neurophysiological experiments in cat models. The proposed experiments are sufficient to determine the physiological torque limit so long as enough specimens are tested to achieve satisfactory statistical power (i.e., >80%).

Due to the small sample size, significant differences between the stiffnesses of intact and failed spines may not be detected. If significant differences do go undetected, then the torque-limit during axial rotation may be computed incorrectly. Given the relative expense and rarity of the fresh-frozen cadaver spines, this is an accepted limitation of the study. If no significant differences are detected but the means appear to be different, then the results of this study can be used as preliminary data in future grant applications, where more human spines can be tested.

D.2.2. What is the scaling relationship for FJC strains between cat and human lumbar spines during physiological motions?

Rationale: In order to extrapolate afferent response to FJC loading in the cat model to the human, a biomechanical relationship should be established during physiological motions. Mechanoreceptors in joint capsules respond to strain (Khalsa *et al.*, 1996), and hence FJC strain is an appropriate quantity to examine. Once the scaling relationship between cat and human FJC strains is established, the afferent response during FJC loading in the cat can be extrapolated to estimate how human afferents might respond during biomechanically similar motions.

Hypothesis 2: During physiological motions, the $L_{6\text{-}7}$ FJC strains in cat cadaveric

lumbar spines will be linearly scalable to the L_{4-5} FJC strains in human cadaveric lumbar spines.

Experimental Variables and Response Measures: The experimental variables are motion type (extension, flexion, lateral bending, and axial rotation), displacement magnitude (controlled at T_{12} in human spines and at L_2 in cat spines), and the side and joint level of the FJC for which strain will be measured. Response measures will be the applied force, applied moments at each joint level, joint motion (6 DoF), and FJC strain.

Protocols: Cat lumbar spine specimens will be prepared (Section D.1.1) and tested (Sections D.1.2 & C.1; Appendix I) during physiological motions of extension, flexion, lateral bending, and axial rotation using methods described earlier (Ianuzzi and Khalsa, 2004; Ianuzzi *et al.*, 2004). As was done in the prior study on human spines, the spinous processes and associated ligaments will be removed to enable viewing of the FJCs. Specimens will be tested to four peak displacements during all four motion types while imaging a single FJC and markers attached to the transverse processes of the vertebrae comprising the joint of interest. Peak displacement magnitudes for the cat spines will be selected as those that reliably produce torques at L_7-S_1 that are smaller in magnitude than the torque limit for that motion (determination of torque limit: see Section D.2.1). As was done for human spines, a single trial will consist of 10 cycles to peak displacement at 10 mm/s, and an intertrial interval of 3 minutes will be used to allow the specimen to return to its physiological state ((Ianuzzi *et al.*, 2004), see Appendix I). After all peak displacements are tested for all motion types, the cameras will be shifted to the next FJC and the protocol repeated. Joint moments will be computed as the product of the applied load and the moment arm (the distance

between the point of load application and the joint). FJC strains will be measured by tracking the 3D displacements of stochastic patterns formed on FJC surfaces by sprinkling them with silicone carbide particles (see Section D.1.3).

Sample Size Determination: As for the previously outlined experiment (Section D.2.1), there is limited data available from which to perform a sample size estimate for cat lumbar FJC strains. However, in prior studies on human lumbar spine specimens, significant trends in FJC strains were identified using comparison of linear regression lines when other parametric tests (ANOVA) fell short of the desired statistical power (Ianuzzi *et al.*, 2004; Little *et al.*, 2004). Assuming that mean FJC strain-global displacement relationships are similarly correlated in the cat, the number of cat lumbar spine specimens to perform similar analyses would be 8 specimens to achieve R^2=0.85 with 80% power (α=0.05; SigmaStat Ver. 2.03, SPSS, Inc.). It is likely that the number of cat specimens will be sufficient because the sample size estimate was performed using data from human lumbar spines, which were not matched for age and size and hence probably more variable.

Data Analysis and Interpretation: Load, joint moment, intervertebral angle, and FJC strain data will be analyzed using the same methods described in detail for human lumbar spines ((Ianuzzi *et al.*, 2004), see Section C.1 & Appendix I). Statistical analyses will be performed using comparison of regressions (linear or nonlinear) (Glantz and Slinker, 2004). The scaling relationship between the biomechanics of the cat and human lumbar spines will take the general form: $CS_H = f(CS_C, GD_H/GD_C, IVA_H/IVA_C, JM_H/JM_C)$, where CS is capsule strain, GD is the global displacement, IVA is the intervertebral angle, and JM is the joint moment. The subscripts C and H represent cat

and human data, respectively. As described in the previous section (Section D.2.1, Data Analysis and Interpretation), incremental sum of squares will be performed to determine the power of the fit (Glantz and Slinker, 2004). If the data can be described using a linear relationship, then Hypothesis 2 is true. If the data cannot be described using a linear relationship, then Hypothesis 2 is not true. In either case, a scaling relationship can be established to describe the data.

Justifications and Limitations: The proposed experiments are necessary to determine the mathematical relationship between the biomechanics of the human and cat lumbar spines during physiological motions. This scaling relationship can be used to interpret neurophysiological data from future studies in the cat model to estimate how human afferents might respond to biomechanically similar motions. Again, there are no experimental constraints to the proposed study per se because the experimental setup/procedures for the biomechanical testing of human cadaveric lumbar spine specimens are well established in the advisor's (Khalsa) laboratory.

The strain data for the human lumbar spines were collected by optically tracking (at 50 Hz) infrared reflective markers (1.16 mm diameter) glued to capsule surfaces. The relatively large marker sizes tended to decrease the resolution of the strain measurements (~0.5% strain). An optical image correlation technique (see Section D.1.3), using a high-speed camera system with improved spatial resolution, will be utilized in the current proposed study to overcome this limitation.

D.2.3. What is the scaling relationship for FJC strains between cat and human lumbar spines during simulated SM?

Rationale: Measurement of afferent response from a single neuron during SM would

be difficult, if not impossible, in human subjects. FJC strains during SM were at the high end of the range that occurred during physiological motions (Section C.2, Appendix II); hence it is likely that the FJC strain magnitudes during SM are sufficient to stimulate capsule mechanoreceptors. Studies have been performed on cat models, where SM-like loads were administered while simultaneously measuring the response of afferents innervating the paravertebral tissues (Pickar and Wheeler, 2001; Pickar, 1999), including neurons with receptive fields in or around the facet (Pickar and McLain, 1995). Human biomechanical data and cat neurophysiological data are difficult to compare because the relationship between the biomechanics of the human and cat lumbar spines is unknown. Knowledge of this relationship would allow for the estimation of how human FJC afferents might respond to biomechanically similar motions.

Hypothesis 3: During simulated SM, the $L_{6\text{-}7}$ FJC strains in cat cadaveric lumbar spines will be linearly scalable to the $L_{4\text{-}5}$ FJC strains in human cadaveric lumbar spines.

Experimental Variables and Response Measures: Experimental variables will include the displacement vector, level of the manipulated vertebra (L_5, L_6, L_7), pre-torque magnitude (applied at L_2 to simulate positioning), and the side and level of the FJC for strain measurements. The response variables include the applied impulse force, the applied impulse moment, vertebral motion (6 DoF), and FJC strain.

Protocols: The experimental setup and protocol will be identical to that described in Section D.1.4 and in detail for human lumbar spines ((Ianuzzi and Khalsa, 2004), see Appendix II). HVLA-SM will be simulated using all combinations of manipulation site and pre-torque magnitude (to simulate positioning with increasing degrees of pelvic rotation) while simultaneously measuring strains at a single FJC, as well as the vertebral

kinematics at the vertebrae comprising the joint of interest. The cameras will then be refocused and the protocol repeated until all of the lumbar FJCs are imaged.

Displacement magnitudes for SM simulations in the cat spine will be determined in preliminary studies using methods similar to those described for the human spine, where a range of displacement magnitudes were tested to determine which resulted in loads typical of SM in vivo (Ianuzzi, 2003). For the cat spines, however, the desired load magnitudes will be smaller than those applied to the human spine. For humans (Triano and Schultz, 1997) and cats (Pickar and Wheeler, 2001), SM loads have varied from 30 – 100% body weight, so displacement magnitudes and impulse speeds will be determined as those that reliably produce loads less than 100% body weight. The displacement profile will be similar to that described for human spines ((Ianuzzi and Khalsa, 2004), see Section C.2 & Appendix II), and it will consist of a preload phase, a quick impulse load, and return to neutral position. Unlike the prior study in human spine, a single impulse speed will be used as speed did not have a significant effect on applied load, vertebral kinematics, or FJC strain magnitudes ((Ianuzzi and Khalsa, 2004), see Appendix II).

Sample Size Determination: FJC strain magnitudes during SM in the cat lumbar spine have never been measured using the experimental setup described here. Hence, sample size was determined based on prior studies on human lumbar spine specimens. Seven cat lumbar spine specimens should be sufficient to attain 80% power using ANOVA while detecting 2% difference in strain (1% standard deviation, α=0.05, 5 groups; SigmaStat Ver. 2.03, SPSS, Inc.). As described in Section D.2.2, higher power is expected from the cat lumbar spine specimens because they are matched according

to age and weight while the human spines were not.

Data Analysis and Interpretation: FJC strains will be measured (Section D.1.3) and calculated (Ianuzzi *et al.*, 2004) as previously described. As has been done for in the human cervical (Winkelstein *et al.*, 2000) and lumbar (Ianuzzi *et al.*, 2004; Little *et al.*, 2004) spines, FJC strains will be reported as the respective mean of the maximum and minimum regional principal strains. Total (i.e., the sum of that which occurred during the application of the pre-torque and at peak impulse) mean FJC strains and all six degrees of freedom of vertebral motions will be reported. Significant differences in total mean strain, total mean vertebral motion, mean applied load, and mean applied moment will be assessed using 2 way repeated measures ANOVA (factors: manipulation site and pre-torque; SigmaStat Version 2.03, SPSS Inc.). The scaling relationship between cat and human FJC strains (for a given combination of pre-torque magnitude and manipulation site) will be determined using methods described for physiological motions (Section D.2.2, Data Analysis and Interpretation). The hypothesis will be supported if a linear fit is sufficient, and it will not be supported if a nonlinear fit is required to describe the data. In either case, it can be assured that some relationship can be formulated.

Justifications and Limitations: The methods proposed for the biomechanical testing of cat lumbar spines during simulated SM are well established in the advisor's (Khalsa) laboratory for testing of human lumbar spines. To repeat what was done for the human spine specimens, the tissues overlying the FJCs, as well as the spinous processes and its associated ligaments, will be removed to enable viewing of FJCs. Because the protocol will be run under displacement control, this will not affect the measurement of FJC strains or vertebral motions, but removal of these supporting structures could result

in smaller loads than would develop in vivo. In human spines, however, vertebral motions using the same experimental setup were similar in magnitude to those that occur during SM in vivo (Triano and Schultz, 1997), and as the magnitudes of intervertebral motion and FJC strain are related ((Ianuzzi *et al*., 2004), see Appendix I), it is likely that the FJC strains obtained using these methods will be similar to those that occur in vivo.

E.1. Estimated timeline for the dissertation

	2004						2005							
Task	**July**	**Aug**	**Sept**	**Oct**	**Nov**	**Dec**	**Jan**	**Feb**	**Mar**	**Apr**	**May**	**Jun**	**Jul**	**Aug**
Write 3D image correlation software	X													
Validate 3D image correlation software	X	X												
Human failure – extension	X													
Cat failure – extension	X													
Write/submit 3D image correlation manuscript		X	X											
Cat & human failure – flexion		X	X											
Cat & human failure – lateral bending		X	X											
Cat & human failure – axial rotation			X	X										
Write/submit cat/human torque-limit manuscript				X	X									
Cat physiological motions					X	X								

	2004						2005							
Task	**July**	**Aug**	**Sept**	**Oct**	**Nov**	**Dec**	**Jan**	**Feb**	**Mar**	**Apr**	**May**	**Jun**	**Jul**	**Aug**
Determine scaling relationship for physiological motions						X	X							
Write/submit physiological motions scaling relationship manuscript							X	X						
Cat impulse loading								X	X					
Determine scaling relationship for impulse loading									X	X				
Write/submit impulse loading scaling relationship manuscript										X	X			
Write dissertation			X	X	X	X	X	X	X	X	X	X		
Defend dissertation													X	
Revisions													X	X
Graduate														X

Reference List

Assendelft,W.J., Morton,S.C., Yu,E.I., Suttorp,M.J., and Shekelle,P.G. (2003) Spinal manipulative therapy for low back pain. A meta-analysis of effectiveness relative to other therapies. *Ann.Intern.Med.* 138**,** 871-881.

Avramov,A., Cavanaugh,J., Ozaktay,A., Getchell,T., and King,A. (1992) The Effects of Controlled Mechanical Loading on Group-II, III, and IV Afferent Units from the Lumbar Facet Joint and Surrounding Tissue. *Journal of Bone and Joint Surgery* 74-A**,** 1464-1471.

Brodeur,R. (1995) The audible release associated with joint manipulation. *J.Manipulative Physiol Ther.* 18**,** 155-164.

Bronfort,G. (1999) Spinal manipulation: current state of research and its indications. *Neurol.Clin.* 17**,** 91-111.

Cavanaugh,J.M., el Bohy,A., Hardy,W.N., Getchell,T.V., Getchell,M.L., and King,A.I. (1989) Sensory innervation of soft tissues of the lumbar spine in the rat. *J.Orthop.Res.* 7**,** 378-388.

Cramer,G.D., Gregerson,D.M., Knudsen,J.T., Hubbard,B.B., Ustas,L.M., and Cantu,J.A. (2002) The effects of side-posture positioning and spinal adjusting on the lumbar Z joints: a randomized controlled trial with sixty-four subjects. *Spine* 27**,** 2459-2466.

Gal,J., Herzog,W., Kawchuk,G., Conway,P., and Zhang,Y. (1994) Biomechanical studies of spinal manipulative therapy (SMT): quantifying the movements of vertebral bodies during SMT. *Journal of the Canadian Chiropractic Association* 38**,** 11-24.

Gal,J., Herzog,W., Kawchuk,G., Conway,P.J., and Zhang,Y.T. (1997) Movements of vertebrae during manipulative thrusts to unembalmed human cadavers. *J.Manipulative Physiol Ther.* 20**,** 30-40.

Glantz,S.A. and Slinker,B.K. (2004) Regression with two or more independent variables. In *Primer of applied regression and analysis of variance* Pp. 54-107. McGraw-Hill, Inc., New York.

Gunning,J.L., Callaghan,J.P., and McGill,S.M. (2001) Spinal posture and prior loading history modulate compressive strength and type of failure in the spine: a biomechanical study using a porcine cervical spine model. *Clin.Biomech.(Bristol., Avon.)* 16**,** 471-480.

Harms,M.C. and Bader,D.L. (1997) Variability of forces applied by experienced therapists during spinal mobilization. *Clin.Biomech.(Bristol., Avon.)* 12**,** 393-399.

Harms,M.C., Innes,S.M., and Bader,D.L. (1999) Forces measured during spinal manipulative procedures in two age groups. *Rheumatology.(Oxford)* 38**,** 267-274.

Hatze,H. (1988) High-precision three-dimensional photogrammetric calibration and object space reconstruction using a modified DLT-approach. *J.Biomech.* 21**,** 533-538.

Hessell,B.W., Herzog,W., Conway,P.J., and McEwen,M.C. (1990) Experimental measurement of the force exerted during spinal manipulation using the Thompson technique. *J.Manipulative Physiol Ther.* 13**,** 448-453.

Ianuzzi,A. (2003) Comparison of human lumbar facet joint capsule strains during impulse loading versus physiological motions. M.S. Stony Brook University.

Ianuzzi,A. and Khalsa,P.S. (2004) Human Lumbar Facet Joint Capsule Strains during Simulated Spinal Manipulation. *Sumitted to The Spine Journal*.

Ianuzzi,A., Little,J.S., Chiu,J.B., Baitner,A., Kawchuk,G., and Khalsa,P.S. (2004) Human lumbar facet joint capsule strains: I. During physiological motions. *Spine J.* 4**,** 141-152.

Khalsa,P.S. and Grigg,P. (1996) Responses of mechanoreceptor neurons in the cat knee joint capsule before and after anterior cruciate ligament transection. *J.Orthop.Res.* 14**,** 114-122.

Khalsa,P.S., Hoffman,A.H., and Grigg,P. (1996) Mechanical states encoded by stretch-sensitive neurons in feline joint capsule. *J.Neurophysiol.* 76**,** 175-187.

Koes,B.W., Assendelft,W.J., van der Heijden,G.J., and Bouter,L.M. (1996) Spinal manipulation for low back pain. An updated systematic review of randomized clinical trials. *Spine* 21**,** 2860-2871.

Lee,R. and Evans,J. (1997) An in vivo study of the intervertebral movements produced by posteroanterior mobilization. *Clin.Biomech.(Bristol., Avon.)* 12**,** 400-408.

Little,J.S., Ianuzzi,A., Chiu,J.B., Baitner,A., and Khalsa,P.S. (2004) Human lumbar facet joint capsule strains: II. Alteration of strains subsequent to anterior interbody fixation. *Spine J.* 4**,** 153-162.

Little,J.S., Ianuzzi,A., and Khalsa,P.S. (2003) Material Properties: Optically measuring facet joint capsule plane strain using image correlation., Biomedical Engineering Society.

Little,J.S. and Khalsa,P.S. (2004) Material properties of the human lumbar facet joint capsule. *Journal of Biomechanical Engineering, In Review*.

Mansour,M., Spiering,S., Lee,C., Dathe,H., Kalscheuer,A.K., Kubein-Meesenburg,D., and Nagerl,H. (2004) Evidence for IHA migration during axial rotation of a lumbar spine segment by using a novel high-resolution 6D kinematic tracking system. *J.Biomech.* 37**,** 583-592.

Nathan,M. and Keller,T.S. (1994) Measurement and analysis of the in vivo posteroanterior impulse response of the human thoracolumbar spine: a feasibility study. *J.Manipulative Physiol Ther.* 17**,** 431-441.

Panjabi,M.M., Krag,M., Summers,D., and Videman,T. (1985) Biomechanical time-tolerance of fresh cadaveric human spine specimens. *J Orthop.Res.* 3**,** 292-300.

Panjabi,M.M., Oxland,T.R., Yamamoto,I., and Crisco,J.J. (1994) Mechanical behavior of the human lumbar and lumbosacral spine as shown by three-dimensional load-displacement curves. *J Bone Joint Surg.Am.* 76**,** 413-424.

Pearcy,M.J. and Bogduk,N. (1988) Instantaneous axes of rotation of the lumbar intervertebral joints. *Spine* 13**,** 1033-1041.

Pickar,J.G. (1999) An in vivo preparation for investigating neural responses to controlled loading of a lumbar vertebra in the anesthetized cat. *J Neurosci.Methods* 89**,** 87-96.

Pickar,J.G. (2002) Neurophysiological effects of spinal manipulation. *The Spine Journal* 1**,** 357-371.

Pickar,J.G. and McLain,R.F. (1995) Responses of mechanosensitive afferents to manipulation of the lumbar facet in the cat. *Spine* 20**,** 2379-2385.

Pickar,J.G. and Wheeler,J.D. (2001) Response of muscle proprioceptors to spinal manipulative-like loads in the anesthetized cat. *J.Manipulative Physiol Ther.* 24**,** 2-11.

Pribanic,T. mdlt1.m. http://www.isbweb.org/software/movanal.html. Version 1.0, 1999.

Reinschmidt,C. reconfu.m. http://www.isbweb.org/software/movanal.html. Version 1.1, 1994.

Soderkvist,I. and Wedin,P.A. (1993) Determining the movements of the skeleton using well-configured markers. *J.Biomech.* 26**,** 1473-1477.

Triano,J. (2000) The Mechanics of Spinal Manipulation. In *Clinical Biomechanics of Spinal Manipulation* (Edited by Herzog,W.) Pp. 92-190. Churchill Livingstone, New York.

Triano,J. and Schultz,A.B. (1997) Loads transmitted during lumbosacral spinal manipulative therapy. *Spine* 22**,** 1955-1964.

Winkelstein,B.A., Nightingale,R.W., Richardson,W.J., and Myers,B.S. (2000) The cervical facet capsule and its role in whiplash injury: a biomechanical investigation. *Spine* 25**,** 1238-1246.

Wolsko,P.M., Eisenberg,D.M., Davis,R.B., Kessler,R., and Phillips,R.S. (2003) Patterns and perceptions of care for treatment of back and neck pain: results of a national survey. *Spine* 28**,** 292-297.

Appendix I. Human lumbar facet joint capsule strains: I. During physiological motions

Published in The Spine Journal, March 2004

ELSEVIER

The Spine Journal 4 (2004) 141–152

THE SPINE JOURNAL

Human lumbar facet joint capsule strains: I. During physiological motions

Allyson Ianuzzi, MS[a], Jesse S. Little, MS[a], Jonathan B. Chiu, MS[a], Avi Baitner, MD[b], Greg Kawchuk, DC, PhD[c], Partap S. Khalsa, DC, PhD[a,*]

[a]*Department of Biomedical Engineering, HSC T18-030, Stony Brook University, Stony Brook, NY 11794-8181, USA*
[b]*Department of Orthopaedics, Stony Brook University, Stony Brook, NY 11794-8181, USA*
[c]*Faculty of Kinesiology, University of Calgary, 2500 University Drive, Calgary, Alberta T2N 1N4, Canada*

Received 3 February 2003; accepted 6 July 2003

Abstract

BACKGROUND CONTEXT: The lumbar facet joint capsule is innervated with nociceptors and mechanoreceptors, and is thought to play a role in low back pain as well as to function proprioceptively.
PURPOSE: In order to examine the facet capsule's potential proprioceptive role, relationships between intracapsular strain and relative spine position were examined.
STUDY DESIGN/SETTING: Lumbar facet joint capsule strains were measured in human cadaveric specimens during displacement-controlled motions.
METHODS: Ligamentous lumbar spine specimens (n=7) were potted and actuated without inducing a moment at the point of application. Spines were tested during physiological motions of extension, flexion, left and right lateral bending. Intervertebral angulations (IVA) were measured using biaxial inclinometers mounted on adjacent vertebrae. Joint moments were determined from the applied load at T12 and the respective moment arms. Capsule plane strains were measured by optically tracking the displacements of infrared reflective markers glued to capsule surfaces. Statistical differences ($p<.05$) in moment, IVA and strain were assessed across facet joint levels using analysis of variance and comparison of linear regressions.
RESULTS: The developed moments and IVAs increased monotonically with increasing displacements; the relationships were highly correlated for all four motion types. Although highly variable among specimens, principal strains also increased monotonically in magnitude with increasing displacements during extension and flexion, but were more complex during lateral bending. At a given joint level, the absolute magnitudes of principal strains and IVA were largest during the same motion type.
CONCLUSIONS: Distinct patterns in principal strains and IVA were identified during physiological motions, lending biomechanical support to the theory that lumbar facet joint capsules could function proprioceptively.

Keywords: Plane strain; Lumbar spine; Facet joint capsule; Biomechanics

Introduction

The lumbar facet joint capsule can be a source of low back pain and may also serve proprioceptive functions. Whereas the former is relatively well established [1–3], the proprioceptive role of the facet capsule is largely theoretical [4]. The facet capsule is innervated by low threshold mechanoreceptors [1,5,6], similar to other peripheral joints [7,8]. The presence of low threshold, slowly and rapidly adapting mechanosensitive neurons imply that these afferents could provide information regarding joint movement and/or position [9]. In the knee [8], the neural response of capsule mechanoreceptors during motions is proportional to suprathreshold capsule tension. Hence, for facet capsule afferents to function proprioceptively during physiological motions of the spine, the capsules would have to be loaded such that their intracapsular strains would be proportional, in some fashion, to the spine's position.

FDA device/drug status: not applicable.

Support in whole or in part was received from National Institutes of Health (NIH)/National Center for Complementary and Alternative Medicine/Palmer under Grant SU01AT001701-01 and NIH/National Institute of Arthritis and Musculoskeletal and Skin Diseases under Grant 1R03AR46865. Nothing of value received from a commercial entity related to this research.

* Corresponding author. Department of Biomedical Engineering, HSC T18-030, Stony Brook University, Stony Brook, NY 11794-8181, USA. Tel.: (631) 444-2457; fax: (631) 444-6646.
E-mail address: partap.khalsa@stonybrook.edu (P.S. Khalsa)

1529-9430/04/$ – see front matter
doi:10.1016/j.spinee.2003.07.008

Afferents innervating the facet joint capsule and the surrounding tissue in the cat [10] and rabbit [11] are responsive to direct capsule loading (ie, strains). Measuring in vivo facet capsule strains in humans with current technology is impractical and unethical, because of the invasive nature of the procedures. However, in situ strains can be measured using human cadaveric spines. During motions of flexion, extension, lateral bending or rotation, using cadaveric, intact, human lumbar spine specimens, consistent patterns of stretch were not found in the extension ratios of lumbar facet joint capsules [12]. In isolated human cervical spine motion segments (eg, C3–C4 motion segment) after flexion and extension, intracapsular principal plane strains were complex, without a clear pattern [13]. In isolated human lumbar motion segments (eg, L4–L5), increasing flexion moment produced increasing uniaxial strain of capsule ligaments [14], but these data were not from direct measurements of the capsule itself. Thus, the biomechanical data in the literature do not yet provide substantive support for the theory of facet capsules functioning proprioceptively.

The current study examined a component of this proprioceptive theory by determining whether strains of lumbar facet joint capsules, during physiological motions of flexion, extension and lateral bending, were proportional to spine motion. A displacement-controlled apparatus was constructed that could repeatedly and reliably create the desired motions. A commercial kinematic system was used to obtain optical measurements of three-dimensional (3D) displacements of small markers glued to the capsule surfaces. Intracapsular plane strains were calculated from these displacements, accounting for the movement of the capsule plane by using an extension of the method of Hoffman and Grigg [15]. Preliminary data have been previously reported in abstract and thesis form [16,17].

Methods

Spine specimens

Human lumbar spine specimens (n=7; mean age, 50 years±12.96 SD; range, 38 to 64 years; sex: 6 men, 1 woman) were shipped frozen from National Disease Research Interchange (Philadelphia, PA). Specimens (T12 to sacrum) were unembalmed and procured within 24 hours postmortem from donors without history of spine pathology. Before testing, the spines were dissected free of all superficial tissue (including insertions of multifidi muscles) to expose the facet joint capsules, thus resulting in a "ligamentous" specimen. Specimens were kept moist with periodic misting of phosphate buffered saline (PBS, pH 7.4) and wrapped in PBS-soaked gauze. A specimen was first oriented vertically by visual inspection such that the L3 and L4 endplates were parallel to the testing surface; and then the sacrum was potted in a quick-setting epoxy (Bondo, Bondo Corporation, Atlanta, GA). After dissection, or at the completion of partial testing, spines were wrapped in plastic, double-bagged, and frozen (−80C). Specimens were allowed to undergo no more than five freeze-thaw cycles, because further cycles may have compromised the tissue's biomechanical properties [18].

Loading apparatus

Physiological motions of the specimens were tested using a custom, displacement-controlled loading apparatus (Fig. 1). The linear actuator consisted of a sled moving on a precision screw, which was fitted with an antibacklash nut and coupled to a torque motor (Model 317; Galil, Inc., Rocklin, CA) and optical encoder (MX21-559; Duncan Electronics, Tustin, CA). Actuator movement was controlled by a digital, programmable, proportional, integrative and derivative (PID) controller (Model 1704; DMC, Galil, Inc., CA; resolution 0.8 μm, repeatability better than 5.0 μm). A program (LabVIEW, version 6.0; National Instruments, Inc., Austin, TX) was written for implementation of a variety of dynamic loading protocols [17].

The entire apparatus sat on a flat steel slab (78 cm×76 cm×2.5 cm). A potted specimen was locked into the slab and coupled to the actuator such that the actuator was horizontal at a given peak displacement. The coupling consisted of a rod in series with a force transducer (Model 9363-D1-50-20P1; Revere Transducers, Tustin, CA; range, ±220 N, resolution 0.02 N), which was connected to the actuator by means of a low-friction universal joint. To connect the rod to the specimen, a U-shaped collar was attached to the T12 vertebral body, creating a single degree of freedom and eliminating off-axis loading of the force transducer. Intervertebral angulation (IVA) at a given joint segment was measured using two biaxial inclinometers (Model UI113077; CFX Technologies, West Chester, PA; range±90 degrees, resolution 0.2 degrees) attached to the respective anterior vertebral bodies. All analog signals (displacement, load, four angles) were collected at 1,000 Hz by an A/D converter (Model PCI-MIO16-E1; National Instruments, Inc., TX) to synchronize collection, low-pass filtered (Model 3905B

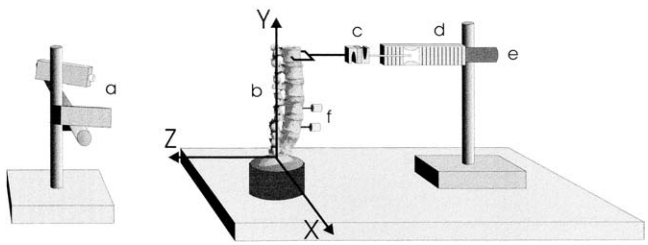

Fig. 1. The schematic of the experimental setup. (a) Two charge coupled device (CCD) cameras were used for optically tracking the markers glued to the facet joint capsule surface for subsequent strain calculations. (b) A human cadaveric lumbar spine specimen was fixed to the testing surface, with coordinate axes as shown. (c) A force transducer was used to measure the applied load. The loading apparatus consisted of (d) a displacement controlled linear actuator with (e) an optical position encoder for the determination of actuator position. (f) Biaxial inclinometers were attached to the facet joint capsule's respective anterior vertebral bodies for measurement of intervertebral angle.

Multichannel Filter; Krohn-Hite Corporation, Brockton, MA) using a cutoff frequency of 700 Hz and streamed to disk.

Plane strain calculations

Plane strains of a facet joint capsule were measured by optically tracking infrared markers (1.16 mm radius) fixed to the capsule surface. Markers were typically arranged in a 3×3 array, although occasionally for narrow capsules a 3×2 array was used. After calibration of the space volume, markers were imaged at 50 Hz using a commercially available kinematic system (Model 50; Qualisys, Inc., Glastonbury, CT), which consisted of two charge coupled device (CCD) cameras fitted with infrared light emitters and filters, appropriate lens, two video processors and software. The 3D coordinates of the resultant centroids were determined post hoc from the two-dimensional (2D) coordinates provided by each of the two video processors (resolution 10 μm in the x, y and z directions).

Capsular plane strains, relative to the vertical neutral position of the spine specimen, were calculated using an algorithm that was an extension of a 2D isoparametric finite element method (FEM) [15]. This algorithm accounted for the rotation of the plane (see Appendix 1), which typically occurred during the physiological spine motions. Each of the nine markers on a given capsule defined a node, from which four quadrilateral regions (or elements) were defined. Plane strains (ε_{xx}, ε_{yy} and ε_{xy}) were calculated for each node, and the strains for an element were calculated as the means of its respective four nodes.

Principal strains E1 and E2 (defined as the principal strains the directions of which were closest to the x-axis and y-axis, respectively) were calculated for each element using the mean element plane strains. Preliminary experiments indicated that for most of the capsular elements, the magnitudes of the principal strains (E1 and E2) typically had opposite signs (ie, one was positive, or tensile, and the other negative, or compressive, for a given motion). Thus, as has been done by others for cervical spine facet capsule strains [13], E1 and E2 were similarly organized as either "maximum" (positive) or "minimum" (negative) principal strains (hereafter denoted as $\hat{E}_1$ and $\hat{E}_2$, respectively) regardless of their respective absolute magnitudes.

Testing protocol

Each specimen was subjected to four motions: flexion, extension, left bending and right bending. For a given motion and facet joint, a trial consisted of 10 consecutive cycles to a given displacement of the spine specimen (10, 20, 30 and 40 mm of horizontal displacement of the T12 vertebra) at 10 mm/second. Because this study was designed to examine physiological motions, displacements were constrained to those producing joint moments at L5–S1 (location of the largest moment arm) less than 10 Nm, a threshold beyond which can produce load–displacement relationships suggestive of damage to soft tissues of the spine [18]. Specimens were tested by imaging one of the L5–S1 joint capsules during all motions, then the contralateral joint and repeating for the next cephalad joint. The intertrial recovery time was 3 minutes to allow sufficient time for the specimen to return to its normal physiological state, as estimated from previous studies on isolated cat knee joint capsule [8,19].

Data analysis and statistics

IVA was calculated as the difference between the angles measured at the vertebral bodies adjacent to the joint capsule of interest and was reported as the mean of 10 cycles at maximum displacements. Joint moments were calculated from the mean peak loads of the last 5 of the 10 cycles (when the load relaxation had reached equilibrium, Fig. 2) and moment arms (ie, distance from the applied load at T12 to the center of each facet joint). Principal strains at maximum displacements were reported as the means of the respective element strains of the 10 cycles in each trial.

For a given parameter (moment, IVA, principal strain) and motion type (flexion, extension, left and right bending), one-way analysis of variance (ANOVA) and post hoc Tukey tests were used to determine if the parameter differed significantly at a given joint level among the four displacement trials (SPSS SigmaStat [Chicago, IL], version 2.03; IL; $\alpha=0.05$). Similarly, the data collected for a given displacement were compared across joint levels. For each motion type, the relationship between a parameter and displacement was regressed. These relationships were compared among joint levels using a pairwise comparison of two linear regression lines (CLRL, $\alpha=0.05$) [20]. At each joint level, the IVA–moment relationship was compared pairwise using comparison of polynomial regression lines (CPRL, $\alpha=0.05$) [21].

Results

Of the seven lumbar spine specimens tested, one exhibited a 9-degree scoliosis, whereas the other six had scolioses less

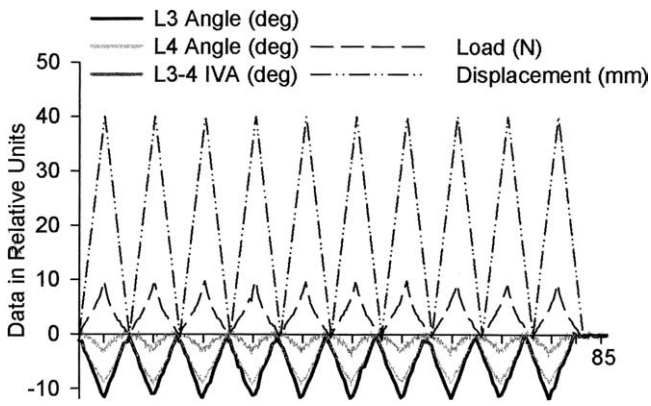

Fig. 2. Data for a representative trial, consisting of 10 cycles of flexion to 40 mm linear displacement (at T12). Load was measured at the point of application (at T12). The intervertebral angle (IVA) at L3–L4 was the difference between the rotations about the x-axis (Fig. 1) for L3 and L4.

than 5 degrees (as indicated by the X-rays of the specimens, obtained before dissection). No gross pathologies were evident by visual inspection or on plain film X-rays. Capsules were visually inspected at low-power magnification (×6) and were found to be intact, exhibiting characteristic gross normal appearance, including white color and a predominantly medial to lateral orientation of collagen fibrils [22].

Moment–displacement relationship

For the maximum displacements of the spine specimens (40 mm linear at T12), the joint moments were below the 10-Nm threshold (Fig. 3), and the largest average moment occurred during 40 mm of left bending (−5.33 Nm). For all motions, joint moment magnitudes significantly (ANOVA, $p<.001$) increased with increasing displacements, with the exception of L3–L4 during extension (Fig. 3). In trials where the difference in displacement was 20 mm or greater (eg, 10 mm vs 30 mm), a significantly greater moment was typically measured at the larger displacement (ANOVA, $p<.05$). The joint moments measured at a given motion and magnitude of displacement (with the exception of 40 mm right bending and left bending), were significantly larger in the more caudal facet joints (L4–L5 and L5–S1) than the cephalic joints (L1–L2 and L2–L3; ANOVA, $p<.05$).

The mean moment–displacement relationships for each joint were highly correlated (mean, $R^2=0.964$; range, 0.919 to 0.990). In all motion types, these relationships differed significantly among all joint levels; moments at a given joint level were significantly larger (ie, more positive in flexion, right bending, and more negative in extension, left bending) than those measured in the respective more cephalic joints (CLRL, $p<.05$).

Intervertebral angulation

During flexion and extension, the *x*-axis was the dominant axis of rotation for each of the vertebrae (Fig. 4, left), with the largest mean IVA measured at the L5–S1 joint for all displacements (greatest overall was 5.18 degrees, 40 mm of extension). In general, more positive angles were obtained with increasing displacements in extension, and more negative angles were measured with increasing displacements in flexion.

During extension, IVAs at a given joint level were significantly (ANOVA, $p<.02$) different from one another, although the trends varied at a given joint level (Fig. 4, left). At L1–L2, significantly different IVA were observed if the trials were separated by 30 mm displacement (ie, 40 mm vs 10 mm, $p=.01$). More caudal joints showed significant differences at smaller displacements, where significant trials were separated by 20 mm or greater displacement for both L4–L5 ($p<.03$) and L2–L3 ($p<.02$), and 10 mm or greater displacement for L5–S1 ($p<.03$); in all cases the angle measured at the larger displacement was greater. At a given displacement, the IVAs measured at L5–S1 were significantly larger than those measured at other joint levels ($p<.05$).

During flexion at a given joint level (Fig. 4, left), the IVA became larger for increasing displacements (ANOVA, $p<.05$); these differences were consistently significant for the caudal three motion units (L3–L4, L4–L5 and L5–S1; Tukey, $p<.005$). For a given displacement, significant differences were observed among IVAs across joint levels (ANOVA, $p<.001$); the angles measured at the more caudal joints (L4–L5 and L5–S1) were generally larger than those obtained at more cephalic joints (L1–L2, L2–L3 and L3–L4; Tukey, $p<.02$).

During left and right bending, the *z*-axis was the dominant axis of rotation (Fig. 4, right), with the largest angles obtained at the L3–L4 joint level for all displacements (largest mean IVA was 6.58 degrees, 40 mm left lateral bending). In general, angles became larger with increasing displacement (ie, more positive during left bending, more negative during right bending).

During left bending at a given joint level (Fig. 4, right), the IVAs were significantly different across displacement

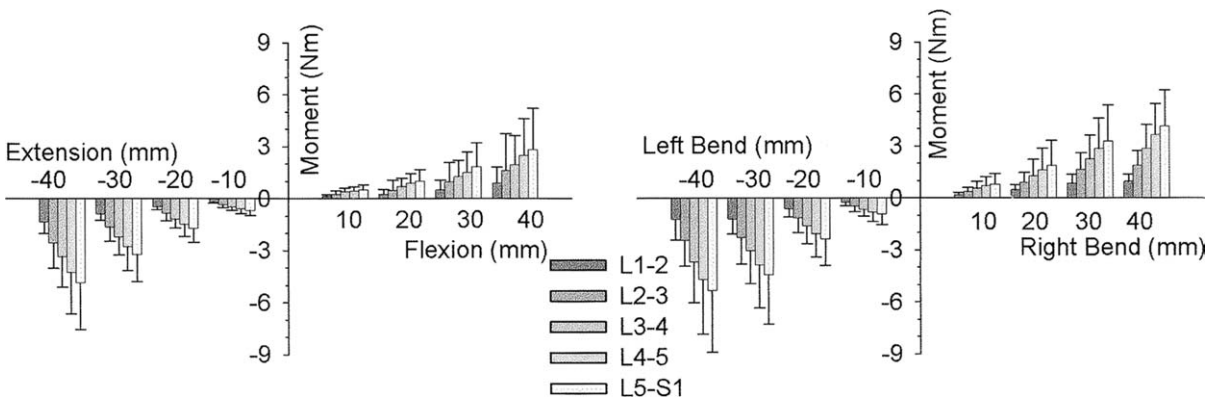

Fig. 3. Joint moments increased monotonically at a given joint level with increasing global displacements of the specimen during (left) extension and flexion, and (right) left and right lateral bending. At a given joint level, the mean moments were significantly larger (comparison of regression lines, $p<.05$) than those at the respective more cephalic joints. Error bars are standard deviations.

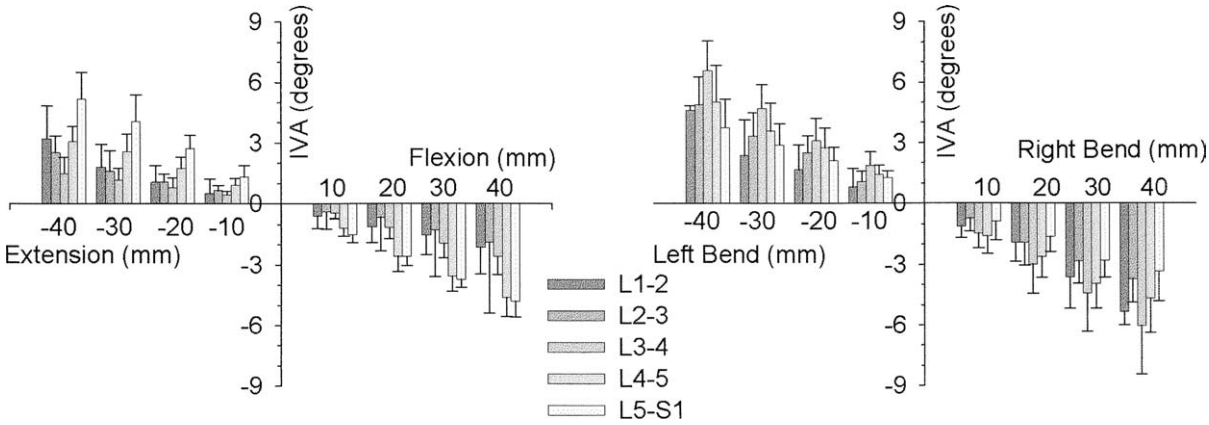

Fig. 4. Intervertebral angles (IVA) at a given joint level increased monotonically with increasing global displacements of the spine specimens. (Left) During extension and flexion, the IVA–displacement relationships at the more caudal vertebrae (L4–L5 and L5–S1) were significantly different compared with the more cephalic vertebrae (L1–L2, L2–L3 and L3–L4, comparison of regression lines, $p<.05$). (Right) During lateral bending, the IVA–displacement relationship at L3–L4 was significantly different compared with all other joints (comparison of regression lines, $p<.05$); at a given specimen displacement, larger IVAs occurred at L3–L4. Error bars show standard deviations.

(ANOVA, $p<.005$). IVA significantly increased at larger displacements at joint levels L2–L3, L3–L4 and L4–L5 (Tukey, $p<.05$). L1–L2 and L5–S1 exhibited similar trends, although these differences were not always significant. At a given displacement, significant differences were observed among the angles measured at each joint level (ANOVA, $p<.04$); the IVA obtained at L3–L4 for any given displacement was typically larger than those measured at L1–L2 and/or L5–S1 (Tukey, $p<.05$).

During right bending at a given joint level (Fig. 4, right), significant differences were observed among IVAs measured at different displacements (ANOVA, $p<.001$). Larger angles were measured at greater displacements if the difference between the displacements compared was greater than or equal to 20 mm (Tukey, $p<.05$). At a given displacement, there were significant differences among the IVAs measured across joint levels (ANOVA, $p<.05$), although there were no consistent trends or consistency in terms of which joint levels were different (Tukey, $p>.05$).

For each of the four motions, mean IVA–displacement relationships were highly correlated (mean, $R^2=0.984$; range, 0.927 to 1.0). The more caudal joints (L4–L5 and L5–S1) typically had significantly larger IVA than the more cephalic joints (L1–L2, L2–L3 and L3–L4) in both extension and flexion (CLRL, $p<.05$). In general, IVA measured during lateral bending at L3–L4 was significantly larger (CLRL, $p<.05$) than those measured at all other joint levels (with the exception of L4–L5 in right bending; CLRL $p>.05$). For each joint level, the mean IVA–moment relationship for extension–flexion was typically best fit using a regression of third-order polynomials (mean, $R^2=0.9856$; range, 0.975 to 0.999), and L1–L2 was the only joint level where this relationship was significantly different from the other motion units (CPRL, $p<.05$; Fig. 5, left). The mean IVA–moment relationships during lateral bending were typically best fit with second-order polynomials (mean, $R^2=0.978$; range, 0.945 to 0.991), although this relationship did not differ significantly among joint levels (CPRL, $p>.05$; Fig. 5, right).

Plane strains

For conciseness, only the two principal strains are reported; compared with ε_{xx}, ε_{yy} and ε_{xy}, they were typically largest in magnitude and, among the seven specimens, exhibited smaller variability. Data obtained from the right and left sides of the spines are reported separately, as they were significantly different (ANOVA, $p<.05$). Designating the principal strains as $\hat{E}_1$ and $\hat{E}_2$ was highly consistent with classification of the strains according to their directions (ie, E1 as closest to the *x*-axis and E2 as closest to the *y*-axis). During extension (where $\hat{E}_2$ was typically larger in absolute magnitude, although negative in sign), a larger percentage of $\hat{E}_2$ had their directions aligned closest to the *y*-axis (ie, were E2 82% on the left side of the spine, 75% on the right side of the spine). During flexion (where $\hat{E}_1$ was typically larger in absolute magnitude than $\hat{E}_2$), $\hat{E}_1$ was predominantly oriented closest to the *y*-axis (ie, were E2 83% on the left side of the spine and 77% on the right side of the spine). During left bending, 63% of $\hat{E}_1$ on the left side of the spine were oriented closest to the *x*-axis (ie, were E1) and 70% of $\hat{E}_1$ on the right side of the spine were oriented closest to the *y*-axis (ie, were E2). The opposite pattern was observed in trials of right bending, with E2 comprising 75% of $\hat{E}_1$ on the left side of the spine and E1 comprising 68% of $\hat{E}_1$ on the right side of the spine.

Intratrial strain data were highly repeatable in a pseudo-random selection of 40-mm trials encompassing all four motion types ($n=18$, average standard deviation of the peak strains and strain rates for 10 cycles were, respectively, 0.53% strain and 0.28% strain/second$\pm$1.2 SD with 95% confidence intervals of 5%). Regardless, with the relatively

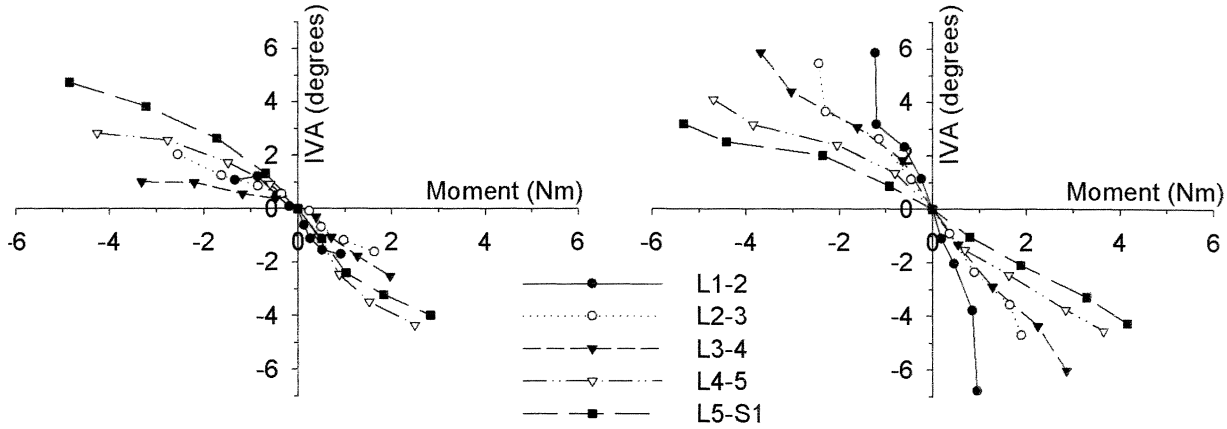

Fig. 5. Average intervertebral angle (IVA)–moment relationships were nonlinear. Although the moment is placed on the abscissa, for these experiments, displacement was the controlled parameter. (Left) Extension–flexion IVA–moment relationship. The largest extension moment (−4.8 Nm) occurred at L5–S1, which also exhibited the largest IVA (4.7 degrees). The largest flexion moment (2.8 Nm) also occurred at L5–S1, although the largest IVA (−4.4 degrees) occurred at L4–L5. (Right) Lateral bending IVA–moment relationship. All joints exhibited relative mirror symmetry during left bending (negative moments) and right bending (positive moments). IVA increased more substantially with increasing moments during lateral bending, especially in the more cephalic joints (L1–L2, L2–L3 and L3–L4). Error bars are not displayed here for clarity; refer to Figs. 3 (moment) and 4 (IVA) for *x* and *y* error bars, respectively.

large variability of regional capsule strains and the relatively small number of samples, ANOVA of the strain data fell short of the desired 80% power ($\hat{E}_1$ mean power 19.5%±23.7% SD, mode 5%; $\hat{E}_2$ mean power 25.3%±26.3%, mode 5%). The estimated sample size to achieve 80% power was 55 samples. Thus, comparisons of strain at a given displacement and/or joint level could not be analyzed for significance with a high degree of certainty. Because the linear regressions were not underpowered, only those results are reported.

In the vertical neutral position, the joint capsules appear to have been preloaded. Using visual observation during motions, no buckling of any of the capsules was ever observed. Because membranes in general do not support in-plane compression, it appears that the large negative principal strains observed, for example in extension, were the result of the capsule undergoing "relaxation" rather than in-plane compression per se. In general, the magnitudes of the strains increased with larger displacements (ie, $\hat{E}_1$ became more positive, $\hat{E}_2$ became more negative). Interspine mean regional principal strains were highly correlated with increasing displacements for all four motion types (mean R^2=0.86±0.23 SD, with only 22% of the trials having R^2<0.75). $\hat{E}_1$ was generally more highly correlated to displacement (mean R^2=0.86±0.23 SD, with only 18% of the $\hat{E}_1$ versus displacement relationships having R^2 less than 0.75) than was $\hat{E}_2$ (mean R^2=0.82±0.23, with approximately 28% of the $\hat{E}_2$ versus displacement relationships having R^2 less than 0.75).

Extension

In extension, mean $\hat{E}_2$ magnitude was largest in the L5–S1 capsule, decreased for more cephalic capsules and was smallest in the L1–L2 capsule (Fig. 6). The largest $\hat{E}_2$ occurred during 40-mm extension at the L5–S1 capsule (−11.0% strain). For increasing extension displacements, $\hat{E}_2$ strains (absolute magnitude) at the L5–S1 capsules were significantly larger compared with L1–L2 and L3–L4 capsules (CLRL, p<.05). The largest $\hat{E}_1$ occurred during 40 mm of extension at L2–L3 capsules (7.7% strain). Mean $\hat{E}_1$ strains at L5–S1 capsules were significantly greater than L1–L2 capsules (CLRL, p<.05).

Flexion

During flexion, $\hat{E}_2$ strains typically were significantly larger at the L4–L5 capsules than at L5–S1 (CLRL, p<.05). The largest $\hat{E}_2$ was measured during 40 mm of flexion at L3–L4 (−7.5% strain); at any given joint/displacement, $\hat{E}_2$ was generally smaller in absolute magnitude during flexion compared with extension. Typically during flexion, $\hat{E}_1$ magnitudes were largest in the most caudal capsules and decreased for more cephalic capsules (Fig. 6). At a given joint capsule, the absolute magnitude of $\hat{E}_1$ was larger than $\hat{E}_2$. Mean $\hat{E}_1$ strains in flexion were also larger than those during extension, and the largest mean $\hat{E}_1$ strain was during 40 mm flexion at the L4–L5 capsules (14.6% strain). Mean $\hat{E}_1$ strains at L1–L2 capsules were significantly smaller in magnitude than L4–L5 and L5–S1 capsules, and L2–L3 capsule strains were significantly smaller than L5–S1 capsule strains (CLRL, p<.05).

Lateral bending: left side

During lateral bending, on the left side of the spine, $\hat{E}_1$ strains of the capsules were typically larger in magnitude during right bending than during left bending (with the exception of L2–L3; Fig. 7, top). In right bending, L4–L5 $\hat{E}_1$ capsule strains were significantly larger than L1–L2 $\hat{E}_1$

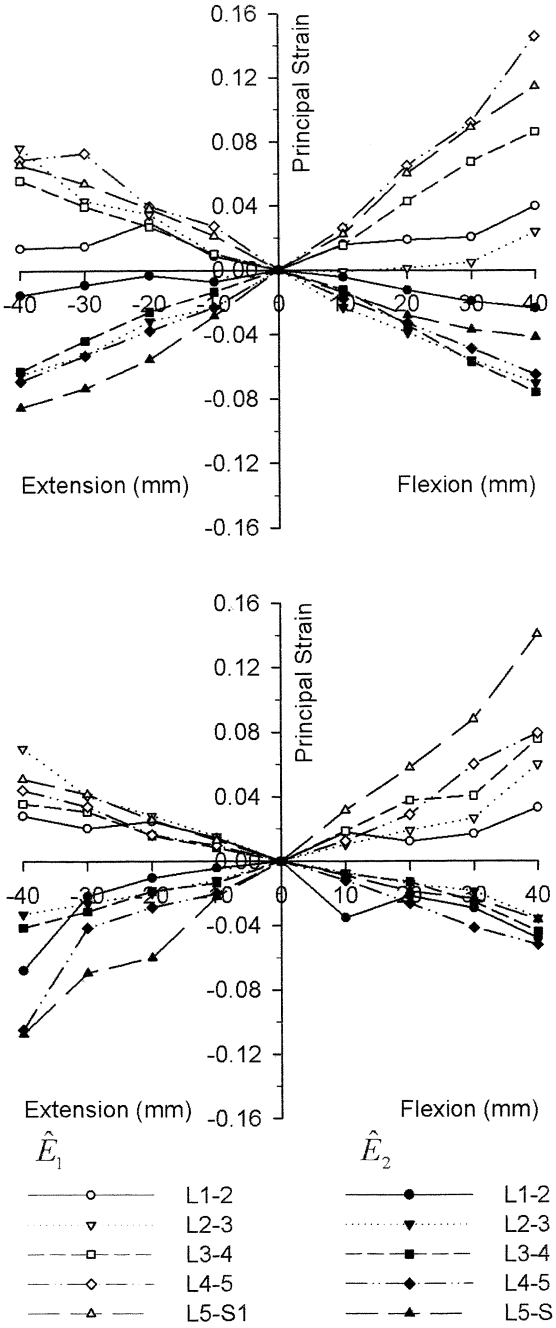

	Left Ext. $\hat{E}_2$ Std. Dev.					Left Ext. $\hat{E}_1$ Std. Dev.				
Displ (mm)	L1-2	L2-3	L3-4	L4-5	L5-S1	L1-2	L2-3	L3-4	L4-5	L5-S1
-40	0.01	0.03	0.01	0.01	0.02	0.01	0.06	0.05	0.06	0.04
-30	0.01	0.04	0.01	0.03	0.04	0.01	0.05	0.03	0.12	0.03
-20	0.01	0.06	0.02	0.04	0.05	0.05	0.03	0.02	0.05	0.02
-10	0.02	0.04	0.03	0.05	0.06	0.01	0.02	0.01	0.05	0.02
Ext. Sig.		*	*+	*	*		*	*	*	*
	Left Flex. $\hat{E}_2$ Std. Dev.					Left Flex. $\hat{E}_1$ Std. Dev.				
Displ (mm)	L1-2	L2-3	L3-4	L4-5	L5-S1	L1-2	L2-3	L3-4	L4-5	L5-S1
10	0.01	0.01	0.01	0.01	0.01	0.03	0.01	0.01	0.02	0.02
20	0.02	0.02	0.02	0.03	0.02	0.05	0.02	0.02	0.05	0.05
30	0.02	0.04	0.04	0.04	0.03	0.01	0.04	0.04	0.05	0.07
40	0.02	0.04	0.04	0.06	0.04	0.01	0.05	0.04	0.08	0.09
Flex. Sig.		*	*+	*+	*			*◦♦	*◦	*◦

	Right Ext. $\hat{E}_2$ Std. Dev.					Right Ext. $\hat{E}_1$ Std. Dev.				
Displ (mm)	L1-2	L2-3	L3-4	L4-5	L5-S1	L1-2	L2-3	L3-4	L4-5	L5-S1
-40	0.01	0.01	0.01	0.01	0.02	0.03	0.16	0.04	0.03	0.04
-30	0.02	0.02	0.01	0.02	0.03	0.03	0.05	0.03	0.03	0.03
-20	0.07	0.02	0.01	0.03	0.06	0.03	0.03	0.01	0.01	0.03
-10	0.15	0.03	0.01	0.21	0.06	0.02	0.02	0.01	0.01	0.01
Ext. Sig.			+	◦	*◦					*
	Right Flex. $\hat{E}_2$ Std. Dev.					Right Flex. $\hat{E}_1$ Std. Dev.				
Displ (mm)	L1-2	L2-3	L3-4	L4-5	L5-S1	L1-2	L2-3	L3-4	L4-5	L5-S1
10	0.02	0.01	0.01	0.01	0.01	0.01	0.01	0.03	0.02	0.03
20	0.03	0.02	0.03	0.02	0.02	0.02	0.01	0.08	0.03	0.06
30	0.04	0.03	0.04	0.03	0.03	0.02	0.03	0.17	0.05	0.07
40	0.05	0.05	0.07	0.04	0.04	0.04	0.08	0.03	0.07	0.09
Flex. Sig.				◦+				+	+	*+	*

Fig. 6. Maximum and minimum principal strains ($\hat{E}_1$ and $\hat{E}_2$, respectively; refer to text for definition) during extension (Ext) and flexion (Flex) on the (top) left and (bottom) right sides of the spine. At a given joint level, $\hat{E}_1$ was typically larger in absolute magnitude during flexion, whereas $\hat{E}_2$ was typically larger in absolute magnitude during extension. The inserted tables display standard deviations (Std Dev) for the mean strains at a given displacement (Displ) and indicate significant trends (Sig) among joint levels (comparison of regression lines, $p<.05$; the symbols *, ○, ♦, and + indicate significant differences from L1–L2, L2–L3, L4–L5 and L5–S1, respectively).

capsule strains (CLRL, $p<.05$). L2–L3 $\hat{E}_1$ capsule strains were significantly smaller than all other joint levels (CLRL, $p<.05$). There were fewer consistent trends in $\hat{E}_1$ during left bending. Overall, the largest $\hat{E}_1$ strains were measured at the L4–L5 capsules during 40 mm of right bending (8.6% strain).

$\hat{E}_2$ strains on the left side of the spine during lateral bending were typically larger in right bending than during left bending, with the exception of L5–S1 capsules. During right bending, the left L5–S1 capsule $\hat{E}_2$ strains were significantly (CLRL, $p<.05$) smaller in absolute magnitude than the three more cephalic joint capsules (L1–L2, L2–L3 and L3–L4); there were no significant differences in $\hat{E}_2$ among the joint capsules during left bending. The largest $\hat{E}_2$ capsular strains on the left side occurred at L2–L3 during 40 mm of right bending (−7.9% strain).

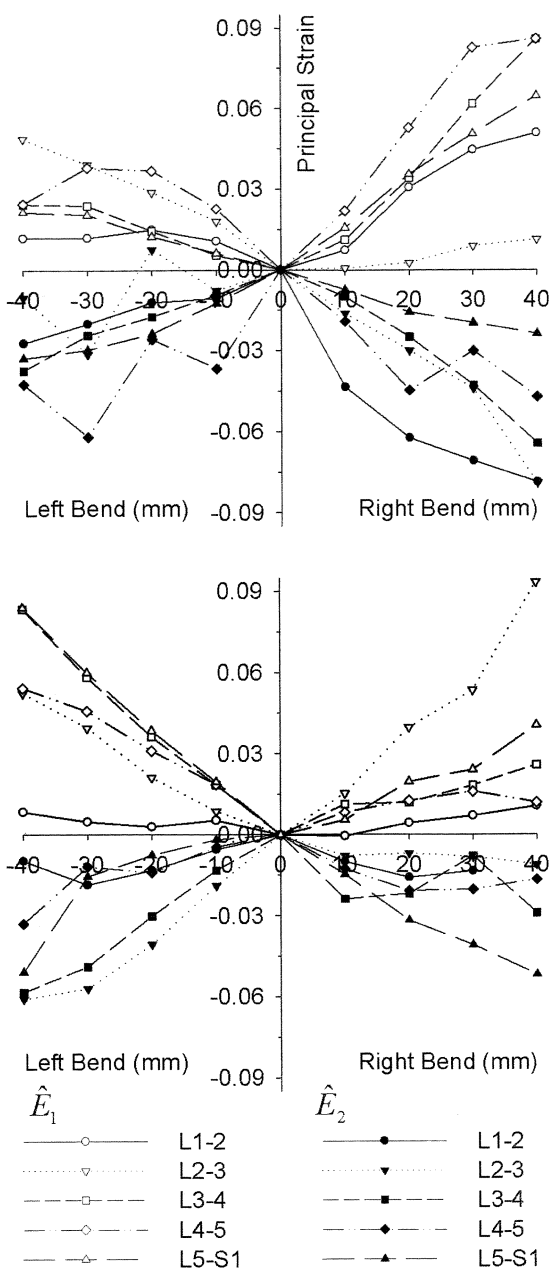

	Left LB $\hat{E}_2$ Std. Dev.					Left LB $\hat{E}_1$ Std. Dev.				
Displ (mm)	L1-2	L2-3	L3-4	L4-5	L5-S1	L1-2	L2-3	L3-4	L4-5	L5-S1
-40	0.01	0.03	0.01	0.06	0.01	0.02	0.07	0.05	0.02	0.02
-30	0.04	0.02	0.02	0.02	0.02	0.02	0.05	0.03	0.10	0.02
-20	0.02	0.06	0.02	0.12	0.02	0.02	0.03	0.02	0.08	0.01
-10	0.04	0.04	0.02	0.03	0.03	0.01	0.02	0.01	0.05	0.01
LB Sig.							*			○
	Left RB $\hat{E}_2$ Std. Dev.					Left RB $\hat{E}_1$ Std. Dev.				
Displ (mm)	L1-2	L2-3	L3-4	L4-5	L5-S1	L1-2	L2-3	L3-4	L4-5	L5-S1
10	0.06	0.02	0.01	0.02	0.01	0.01	0.02	0.01	0.02	0.02
20	0.08	0.04	0.02	0.10	0.02	0.04	0.03	0.03	0.04	0.04
30	0.10	0.05	0.03	0.03	0.03	0.06	0.05	0.06	0.07	0.05
40	0.12	0.05	0.05	0.04	0.04	0.06	0.08	0.06	0.06	0.08
RB Sig	+	+	+				*	○	○ *	○

	Right LB $\hat{E}_2$ Std. Dev.					Right LB $\hat{E}_1$ Std. Dev.				
Displ (mm)	L1-2	L2-3	L3-4	L4-5	L5-S1	L1-2	L2-3	L3-4	L4-5	L5-S1
-40	0.01	0.02	0.01	0.01	0.01	0.01	0.04	0.07	0.05	0.07
-30	0.01	0.04	0.03	0.02	0.01	0.01	0.03	0.06	0.04	0.05
-20	0.03	0.05	0.04	0.04	0.01	0.01	0.02	0.04	0.03	0.03
-10	0.00	0.06	0.07	0.03	0.04	0.01	0.01	0.02	0.02	0.01
LB Sig.		*	♦	○	* ○		*	* +		
	Right RB $\hat{E}_2$ Std. Dev.					Right RB $\hat{E}_1$ Std. Dev.				
Displ (mm)	L1-2	L2-3	L3-4	L4-5	L5-S1	L1-2	L2-3	L3-4	L4-5	L5-S1
10	0.00	0.02	0.02	0.01	0.01	0.01	0.02	0.02	0.01	0.01
20	0.02	0.03	0.03	0.02	0.02	0.01	0.04	0.02	0.01	0.02
30	0.01	0.04	0.07	0.02	0.03	0.01	0.06	0.03	0.02	0.02
40	-	0.07	0.03	0.02	0.02	0.01	0.11	0.03	0.01	0.03
RB Sig		+	+	+			*	*	○ +	*

Fig. 7. Maximum and minimum principal strains ($\hat{E}_1$ and $\hat{E}_2$, respectively; refer to text for definition) during left bending (LB) and right bending (RB) on the (top) left and (bottom) right sides of the spine. At a given joint level, $\hat{E}_1$ was typically larger in absolute magnitude during tensile motions, whereas $\hat{E}_2$ was typically larger in absolute magnitude during compressive motions. The inserted tables display standard deviations (Std Dev) for the mean strains at a given displacement (Displ) and indicate significant trends (Sig) among joint levels (comparison of regression lines, $p < .05$; the symbols *, ○, ♦, and + indicate significant differences from L1–L2, L2–L3, L3–L4, L4–L5 and L5–S1, respectively).

Lateral bending: right side

On the right side of the spine, $\hat{E}_1$ strains of the joint capsules during left bending were typically larger in magnitude in the more caudal joints (L3–L4, L4–L5, L5–S1) than those measured during right bending, whereas the opposite was true for the more cephalic joint capsules (L1–L2 and L2–L3; Fig. 7). During right bending, $\hat{E}_1$ at the L1–L2 capsules was significantly smaller in magnitude compared with the caudal capsules (L2–L3, L3–L4 and L5–S1); L4–L5 $\hat{E}_1$ capsule strains were significantly smaller than those in the L2–L3 and L5–S1 capsules (CLRL, $p<.05$). During left bending, $\hat{E}_1$ strains of the L1–L2 capsule were significantly smaller than those in L2–L3 and L3–L4 capsules, and the L3–L4 capsule strains were significantly smaller in magnitude than those in the L5–S1 capsule (CLRL, $p<.05$). The largest $\hat{E}_1$ capsular strains were measured during 40 mm of right bending at the L2–L3 joint (9.4% strain).

During left bending, $\hat{E}_2$ strains were generally larger in the more cephalic joint capsules (L1–L2, L2–L3 and L3–L4) compared with the more caudal joint capsules (L4–L5

and L5–S1); the opposite was true during right bending. In left bending, $\hat{E}_2$ strains at L1–L2 capsules differed significantly from those in the L2–L3 and L5–S1 capsules (CLRL, $p<.05$). L2–L3 capsular strains were significantly larger than the L4–L5 and L5–S1 capsules, and L3–L4 capsular strains were significantly larger than L4–L5 capsules (CLRL, $p<.05$ for all). During right bending, $\hat{E}_2$ at L5–S1 capsules was significantly larger than all other joint capsules (CLRL, $p<.05$). The largest $\hat{E}_2$ strain (absolute value) was measured at L2–L3 capsules during 40 mm of left bending (−6.1% strain).

In general, at a given joint level, the motion (flexion/extension vs left bending/right bending) during which the joint experienced the largest IVA was the same motion during which the largest principal strain occurred (Table 1). In addition, if a comparison between the IVA-displacement regressions for two joints was statistically significant, then it was likely that a significant comparison of the same joints was observed in the principal strain-displacement regressions (particularly during motions producing strains of high magnitude, as in flexion).

Discussion

To our knowledge, this is the first report of in situ plane strains in lumbar facet joint capsules developed during physiological motions of ligamentous lumbar spine specimens (T12 sacrum). From full extension to full flexion of the lumbar spine, mean principal strains of the joint capsules increased monotonically with the largest strains occurring in the most caudal joint capsules. Capsule strains during left and right bending demonstrated relative mirror symmetry. These data provide support for the concept that joint capsule loading could provide a biomechanical signal for lumbar spine proprioception.

Using a displacement-controlled apparatus, the IVAs in the current study were similar to those obtained by Panjabi et al. [23] using a moment-controlled apparatus. In both studies, the maximum IVAs during flexion and extension trials were measured at L5–S1 and averaged approximately 5 degrees (compare Fig. 4, left, in current study with Fig. 3 in Panjabi et al. [23]). In the current study, the maximum IVA during lateral bending was at L3–L4 (6.6 degrees), whereas in Panjabi et al. [23] the maximum IVA was at L2–3 (5.3 degrees) (compare Fig. 4, right, in current study with Fig. 5 in Panjabi et al. [23]); however, in both cases these values were not significantly different from IVA measured at other joints. Indeed, the IVA for a given moment appears to be similar in both studies (ie, the mean IVAs in this study typically appeared within their respective standard deviations).

Table 1
Motions creating the largest intervertebral angle and principal strain for each joint level

Joint level	Maximum IVA (degrees)	Largest strain
L1–L2	RB (−6.77)	RB (0.050)
L2–L3	LB (5.44)	RB (0.090)
L3–L4	RB (−6.0)	RB (0.086)
L4–L5	F (−4.54)	F (0.146)
L5–S1	E (5.18)	F (0.140)

E=extension; F=flexion; IVA=intervertebral angle; LB=left bending; RB=right bending.

Despite high variability within the data, consistent patterns of strain related to specimen position were observed. Although intracapsular strains were heterogeneous, similar to those observed in the cervical spine [13], elemental strains systematically increased with increasing displacements of flexion/extension. For a given lumbar facet joint capsule, the motion during which the joint displaced the most (ie, a maximum IVA was measured) was the same type of motion during which the capsular ligament experienced the largest strains. When considering the lumbar spine as a whole, significant differences in the IVA–displacement relationships for motion segments usually meant that their strain–displacement relationships were significantly different as well. This was most strongly observed during flexion and less so during motions of extension, left and right bending, possibly because of differences in the mechanics of each motion. These trends were in contrast to the lack of consistent strain patterns observed in cervical spine facet joint capsules [13], which may be the result of the anatomical differences between the cervical and lumbar spines.

Lumbar facet capsule principal strains (tensile) in the current study were similar in magnitude to uniaxial facet capsule strains reported by Panjabi et al. [14], although the joint moments in the current study were much smaller. An explanation for this was the relative sigmoidal relationship between intervertebral angles and joint moment, as shown in the current study as well as by Panjabi et al. [23] and in cervical spine in vivo [24]. For larger moments, the IVAs plateau, and there was minimal increase in IVA with increasing moment [23]. The current study depicted similar nonlinear relationships (Fig. 5), although because the developed moments were smaller, there was less demonstration of a plateau. Because the facet joint capsule strains were related to the IVAs, then with similar IVAs in both studies it was reasonable that they would have comparable magnitudes of capsule strains.

Similar to observations in the cervical spine [13], the lumbar facet joint capsules often experience both in-plane tensile and compressive strains simultaneously in response to physiological motions (ie, in over 80% of the trials in the current study). Hence, when reporting plane principal strains in facet capsule, it was valuable to present both principal strains. For example, in lumbar facet capsules the maximum principal strains ($\hat{E}_1$ in the current study) were typically larger (more positive) during tensile motions (ie, flexion and lateral bending contralateral to the facet joint of interest) than in compressive motions (ie, extension and lateral bending toward the facet joint of interest); the opposite was generally

observed when considering the minimum principal strains ($\hat{E}_2$ in the current study), particularly during extension and flexion. For this reason, significant relationships or trends between motions and capsule strains were generally not apparent in $\hat{E}_1$ strains during compressive motions, whereas several trends were identified in $\hat{E}_2$ strains for the same motions. Thus, although presenting both principal strains was more complex, some significant relationships became apparent that might have otherwise been missed.

The organization of the principal strains as maximum ($\hat{E}_1$) and minimum ($\hat{E}_2$) was supported by the fact that a large percentage of the strains in either group had the same orientation (ie, were either E1 or E2). In addition, the dominant orientation of the principal strain largest in magnitude was logical when considering motion type and capsule location. For instance, during compressive motions one would expect that the capsule would compress along the *y*-axis and thus elongate along the *x*-axis. Conversely, during tensile motions, one would expect that the capsule would elongate along the *y*-axis and compress along the *x*-axis. The data were generally consistent with this reasoning for all four motion types.

There are a number of constraints that should be considered when interpreting the results from the current study. First, the specimens were obtained from older adults, and preliminary data (not shown) from our laboratory for younger spines, which generally are much more flexible, suggest that capsule strains in younger spines can be much larger for the same joint moment. Second, the variability in the data was relatively high, which was likely the result of a combination of factors, including age, gender and relative overall health of the donors. Furthermore, the variability in strain patterns may have been exaggerated by differences in marker placement, because in some cases it was necessary to place the array of markers in an irregular pattern or to use fewer markers because of capsule morphology. Although an irregularly shaped element would not have affected the accuracy of the strain measurement, a difference in marker placement could affect principal strain patterns from one capsule to the next (given the heterogeneity of strains on the capsular surface). Variability was also no doubt influenced by slight differences in collagen fiber orientation in different regions of the capsular surface and/or multiple points of insertion of the capsular ligament [22]. Orienting the spine in its neutral position using visual inspection alone may have increased the variability observed among the spine specimens as opposed to using other inspection techniques. However, these increases are likely to be small, as X-ray validation of the neutral position was shown to result in similar IVA variability [23]. Finally, in spite of precautions to keep the spine specimens moist, each capsule was exposed directly to air for significant periods of time, and each of the spine specimens underwent a few freeze-thaw cycles, all of which could have affected the measured strains.

It is well established that facet joint capsules are innervated with mechanoreceptors and nociceptors [1,6,10,11,25,26], and it follows that this system may serve proprioceptive functions [4,27]. It has been demonstrated in animal models that afferents innervating the lumbar facet capsule and surrounding tissue respond to capsular manipulation [10] and stretch [11]. The current study provides biomechanical evidence that there is a consistent pattern of facet capsule strains associated with lumbar motions, and thus provides support to this proprioceptive theory in human lumbar spines.

Appendix

Calculation of plane strains during plane rotation

To account for capsule plane rotation, four general modifications were necessary and made to the 2D isoparametric finite element method of Hoffman and Grigg [15] for calculating plane strains. First, all marker centroids were measured in 3D (*x*, *y*, *z*), rather than 2D (*x*, *y*). Second, isoparametric "brick" (eight-noded) elements were created rather than 2D quadrilateral (four-noded) planar elements. These brick elements consisted of the four "real" nodes defined from the measured centroids of four markers, and four "virtual" nodes, each of which was normal to the actual plane and respectively projecting from a real node at a constant arbitrary, but reasonable, distance of 1 mm (Fig. A1). Hence, brick elements of constant 1-mm thickness were created. Third, Lagrangian strains were calculated using a full 3D approach for each of the eight nodes of a brick element. The "real" quadrilateral and its virtual nodes were then mapped from Cartesian (*x*, *y*, *z*) to natural (*s*, *t*, *r*) coordinates using interpolation functions [28] (equations A1 to A8).

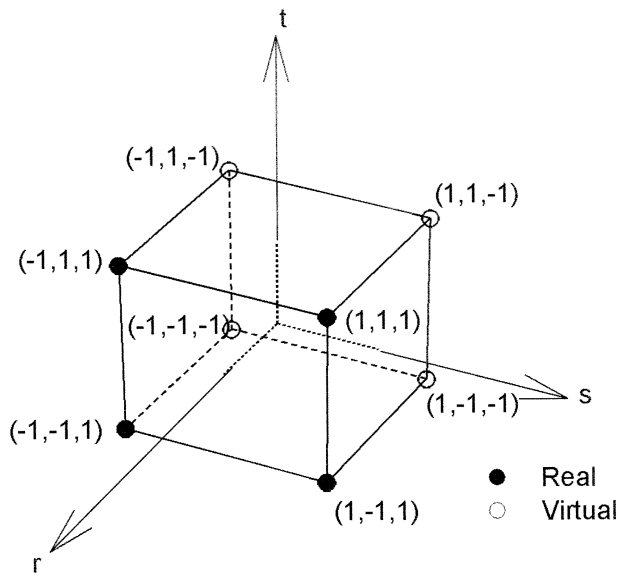

Fig. A1. Eight-noded "brick" element, created by the four front real nodes (ie, centroids of the markers fixed to the facet joint capsule surface) and the four virtual nodes, for plane strain calculations using a three-dimensional finite element method. Natural coordinate axes (*r*, *s*, *t*) are shown.

$$N_1 = \frac{1}{8}(1-s)(1-t)(1+r) \quad \text{(A1)}$$

$$N_2 = \frac{1}{8}(1+s)(1-t)(1+r) \quad \text{(A2)}$$

$$N_3 = \frac{1}{8}(1+s)(1+t)(1+r) \quad \text{(A3)}$$

$$N_4 = \frac{1}{8}(1-s)(1+t)(1+r) \quad \text{(A4)}$$

$$N_5 = \frac{1}{8}(1-s)(1-t)(1-r) \quad \text{(A5)}$$

$$N_6 = \frac{1}{8}(1+s)(1-t)(1-r) \quad \text{(A6)}$$

$$N_7 = \frac{1}{8}(1+s)(1+t)(1-r) \quad \text{(A7)}$$

$$N_8 = \frac{1}{8}(1-s)(1+t)(1-r) \quad \text{(A8)}$$

As was done in Hoffman and Grigg [15], these interpolation functions were used in calculating the spatial partial derivatives of the nodal initial positions (x, y, z) and displacements (u, v, w) (hence, this approach was an isoparametric finite element method). The chain rule then yields the partial derivatives expressions of the nodal displacements in the natural coordinate system for the 3D isoparametric element (equations A9 to A11).

$$\begin{Bmatrix} \frac{\partial u}{\partial s} \\ \frac{\partial u}{\partial t} \\ \frac{\partial u}{\partial r} \end{Bmatrix} = \begin{pmatrix} \frac{\partial x}{\partial s} & \frac{\partial y}{\partial s} & \frac{\partial z}{\partial s} \\ \frac{\partial x}{\partial t} & \frac{\partial y}{\partial t} & \frac{\partial z}{\partial t} \\ \frac{\partial x}{\partial r} & \frac{\partial y}{\partial r} & \frac{\partial z}{\partial r} \end{pmatrix} \begin{Bmatrix} \frac{\partial u}{\partial x} \\ \frac{\partial u}{\partial y} \\ \frac{\partial u}{\partial z} \end{Bmatrix} \quad \text{(A9)}$$

$$\begin{Bmatrix} \frac{\partial v}{\partial s} \\ \frac{\partial v}{\partial t} \\ \frac{\partial v}{\partial r} \end{Bmatrix} = \begin{pmatrix} \frac{\partial x}{\partial s} & \frac{\partial y}{\partial s} & \frac{\partial z}{\partial s} \\ \frac{\partial x}{\partial t} & \frac{\partial y}{\partial t} & \frac{\partial z}{\partial t} \\ \frac{\partial x}{\partial r} & \frac{\partial y}{\partial r} & \frac{\partial z}{\partial r} \end{pmatrix} \begin{Bmatrix} \frac{\partial v}{\partial x} \\ \frac{\partial v}{\partial y} \\ \frac{\partial v}{\partial z} \end{Bmatrix} \quad \text{(A10)}$$

$$\begin{Bmatrix} \frac{\partial w}{\partial s} \\ \frac{\partial w}{\partial t} \\ \frac{\partial w}{\partial r} \end{Bmatrix} = \begin{pmatrix} \frac{\partial x}{\partial s} & \frac{\partial y}{\partial s} & \frac{\partial z}{\partial s} \\ \frac{\partial x}{\partial t} & \frac{\partial y}{\partial t} & \frac{\partial z}{\partial t} \\ \frac{\partial x}{\partial r} & \frac{\partial y}{\partial r} & \frac{\partial z}{\partial r} \end{pmatrix} \begin{Bmatrix} \frac{\partial w}{\partial x} \\ \frac{\partial w}{\partial y} \\ \frac{\partial w}{\partial z} \end{Bmatrix} \quad \text{(A11)}$$

Solving for the right-most vectors in equations A9 to A11 then allows for plane strain calculations using the Lagrangian large strain formulation [29].

Fourth, strain artifacts resulting from plane rotation were eliminated by performing a coordinate transformation of the 3D strains relative to the original reference plane (ie, where the spine was in its neutral or reference position). The transformation matrix [T] was determined by the matrix operation necessary to transform the plane of the deformed nodes [n] such that it would be parallel to the reference plane [n'] [30]:

$$n' = [\mathrm{T}]n \quad \text{(A12)}$$

Then, the nodal strain tensor was multiplied by this transformation matrix:

$$E' = [\mathrm{T}]E \quad \text{(A13)}$$

Because the thickness was held constant, all out-of-plane shears became identically zero (ie, $\varepsilon_{yz}=\varepsilon_{xz}=\varepsilon_{zy}=\varepsilon_{zx}=0$) from the transformation, resulting in plane strains from a 3D strain calculation method.

Validation of this algorithm was performed as follows: 1) 3D coordinates of four reference nodes and their coordinates following known, arbitrary deformations, but without plane rotation, were input, and the algorithm correctly calculated the respective plane strains; 2) 3D coordinates of quadrilaterals at arbitrary planes of rotations, but without any internodal displacement, were input. This correctly resulted in zero strain; 3) nodal coordinates of known displacements and plane rotations were input, which resulted in correct calculation of plane strains.

References

[1] Cavanaugh JM, Ozaktay AC, Yamashita T, Avramov A, Getchell TV, King AI. Mechanisms of low back pain: a neurophysiologic and neuroanatomic study. Clin Orthop 1997;1:166–80.

[2] Yang KH, King AI. Mechanism of facet load transmission as a hypothesis for low-back pain. Spine 1984;9:557–65.

[3] Helbig T, Lee CK. The lumbar facet syndrome. Spine 1988;13:61–4.

[4] Pickar JG. Neurophysiological effects of spinal manipulation. Spine J 2002;2:357–71.

[5] Cavanaugh JM, Ozaktay AC, Yamashita HT, King AI. Lumbar facet pain: biomechanics, neuroanatomy, and neurophysiology. J Biomech 1996;29:1117–29.

[6] McLain RF, Pickar JG. Mechanoreceptor endings in human thoracic and lumbar facet joints. Spine 1998;23:168–73.

[7] Grigg P. Properties of sensory neurons innervating synovial joints. Cells Tissues Organs 2001;169:225.

[8] Khalsa PS, Hoffman AH, Grigg P. Mechanical states encoded by stretch-sensitive neurons in feline joint capsule. J.Neurophysiol 1996;76:175–87.

[9] Sjolander P, Johansson H, Djupsjobacka M. Spinal and supraspinal effects of activity in ligament afferents. J Electromyogr Kinesiol 2002;12:167–76.

[10] Pickar JG, McLain RF. Responses of mechanosensitive afferents to manipulation of the lumbar facet in the cat. Spine 1995;20:2379–85.

[11] Avramov A, Cavanaugh JM, Ozaktay AC, Getchell TV, King AI. The effects of controlled mechanical loading on group-II, III, and IV afferent units from the lumbar facet joint and surrounding tissue: an in vitro study. J Bone Joint Surg 1992;74A:1464–71.

[12] El-Bohy AA, Goldberg SJ, King AI. Measurement of facet capsular stretch. 1987 Biomechanics Symposium. Paper presented at: 1987 American Society of Mechanical Engineers Applied Mechanics, Bioengineering, and Fluids Engineering Conference, June 14–17, 1987, New York, NY. p. 161–4.

[13] Winkelstein BA, Nightingale RW, Richardson WJ, Myers BS. The cervical facet capsule and its role in whiplash injury: a biomechanical investigation. Spine 2000;25:1238–46.

[14] Panjabi MM, Goel VK, Takata K. Physiologic strains in the lumbar spinal ligaments. An in vitro biomechanical study. 1981 Volvo Award in Biomechanics. Spine 1982;7:192–203.

[15] Hoffman AH, Grigg P. A method for measuring strains in soft tissue. J Biomech 1984;17:795–800.

[16] Chiu J. Facet joint capsule strains of human lumbar spine specimens during physiological motions. 2001 Master's Thesis. State University of New York at Stony Brook.

[17] Saldanha A, Kawchuk G, Tateosian V, Khalsa PS. Control software for measuring physiological, dynamic facet capsule strains in human, lumbar spine specimens. Landover, MD: Biomedical Engineering Society, 2000:14671.

[18] Panjabi MM, Krag M, Summers D, Videman T. Biomechanical time-tolerance of fresh cadaveric human spine specimens. J Orthop Res 1985;3:292–300.

[19] Khalsa PS, Grigg P. Responses of mechanoreceptor neurons in the cat knee joint capsule before and after anterior cruciate ligament transection. J Orthop Res 1996;14:114–22.

[20] Glantz SA. How to test for trends: primer of biostatistics. 4th ed. New York: McGraw-Hill, 1997;238–41.

[21] Glantz SA, Slinker BK. Regression with two or more independent variables: primer of applied regression and analysis of variance. 2nd ed. New York: McGraw-Hill, 2001;54–107.

[22] Yamashita T, Minaki Y, Ozaktay AC, Cavanaugh JM, King AI. A morphological study of the fibrous capsule of the human lumbar facet joint. Spine 1996;21:538–43.

[23] Panjabi MM, Oxland TR, Yamamoto I, Crisco JJ. Mechanical behavior of the human lumbar and lumbosacral spine as shown by three-dimensional load-displacement curves. J Bone Joint Surg Am 1994; 76:413–24.

[24] McClure P, Siegler S, Nobilini R. Three-dimensional flexibility characteristics of the human cervical spine in vivo. Spine 1998;23:216–23.

[25] Yamashita T, Cavanaugh JM, El-Bohy AA, Getchell TV, King AI. Mechanosensitive afferent units in the lumbar facet joint. J.Bone Joint Surg [Am] 1990;72:865–70.

[26] McLain RF. Mechanoreceptor endings in human cervical facet joints. Spine 1994;19:495–501.

[27] Pickar JG. An in vivo preparation for investigating neural responses to controlled loading of a lumbar vertebra in the anesthetized cat. J Neurosci Methods 1999;89:87–96.

[28] Grandin H. Fundamentals of the finite element method. Prospect Heights, IL: Waveland Press, 1991.

[29] Malvern LE. Finite strain and deformation: introduction to the mechanics of a continuous medium. London: Prentice-Hall International, 1969:154–72.

[30] Chung TJ. Vectors and tensors: applied continuum mechanics. Cambridge: Cambridge University Press, 1996:4–15.

Appendix II. Human lumbar facet joint capsule strains during simulated high velocity, low amplitude spinal manipulation

Allyson Ianuzzi, M.S., Partap S. Khalsa, D.C., Ph.D.
Department of Biomedical Engineering, Stony Brook University

Submitted to The Spine Jounral, March 2004

Abstract

Background Context: Spinal manipulation (SM) is an effective treatment for low back pain (LBP), and it has been theorized that SM induces a beneficial neurophysiological effect by stimulating mechanically sensitive neurons in the lumbar facet joint capsule (FJC). *Purpose*: The purpose of this study was to determine whether human lumbar FJC strains during simulated SM were different from those that occur during physiological motions. *Study Design/Setting*: Lumbar FJC strains were measured in human cadaveric spine specimens during physiological motions and simulated SM in a laboratory setting. Methods: Specimens were tested during displacement-controlled physiological motions of flexion, extension, lateral bending, and axial rotations. SM was simulated using combinations of manipulation site (L3, L4, and L5), impulse speed (5, 20, and 50 mm/s), and pre-torque magnitude (applied at T12 to simulate patient position; 0, 5, 10 Nm). FJC strains and vertebral motions (using six degrees of freedom) were measured during both loading protocols. *Results*: During SM, the applied loads were within the range measured during SM in vivo. Vertebral translations occurred primarily in the direction of the applied load, and were similar in magnitude regardless of manipulation site. Vertebral rotations and FJC strain magnitudes during SM were within the range that occurred during physiological motions. At a given FJC, manipulations delivered distally induced capsule strains similar in magnitude to those that occurred when the manipulation was applied proximally. *Conclusions*: FJC strain magnitudes during SM were within the physiological range, suggesting that SM is biomechanically safe. Successful treatment of patients with LBP using SM may not require precise segmental specificity, because the strain magnitudes at a given FJC during SM do not

depend upon manipulation site. The theorized beneficial neurophysiological effect of SM may be due to the pattern of capsule mechanoreceptor stimulation, perhaps resulting from high strain rates.

Keywords: Manipulation, Spinal; Zygapophyseal Joint; Manipulation, Chiropractic; Low Back Pain; Strain; Joint Capsule; Facet Joint, Lumbar Spine

Introduction

Low back pain (LBP) affects 80% of the population at some point during their lifespan, with an expected recurrence rate of approximately 85% [1]. In a recent national survey on patterns and perceptions of care [2], more people afflicted with back pain sought conventional therapy (such as physical therapy) versus chiropractic care (37% versus 20%, respectively). However, patients who sought chiropractic therapy were more often satisfied with the treatment (61% versus 37% seeking conventional therapy). This is concurrent with recent meta-analyses of randomized clinical trials that indicated that spinal manipulation (SM) was an effective treatment for LBP, with rare incidence of serious adverse effects [3-5]. However, SM has evolved empirically and little is known about the physiological mechanisms by which it is effective [6]. It has been theorized that high velocity, low amplitude (HVLA) SM, induces a beneficial neurophysiological effect by stimulating the mechano-sensitive neurons of the facet joint capsule (FJC) [7].

The biomechanics of HVLA SM have been studied in vivo [6,8]. A patient is positioned side-lying with varying degrees of pelvic rotation. The practitioner administers a preload force on a single vertebral process (e.g., lumbar mamillary process) to rotate the

vertebra near the limits of its active range of motion. Then, an impulse load is applied such that the resultant displacement does not exceed the passive range of motion of the joint [6]. The preload force transmitted through the trunk approximates 100 N, and the transmitted force during the impulse, which is maintained for approximately 200 ms, ranges from 50 to 400 N [8-11].

Vertebral motions during SM are relatively small, as demonstrated by in vivo studies and predictive modeling. The application of a posteroanterior (PA) load of 150 N to the L4 spinous process produced intervertebral rotations of approximately 1 – 2.5° and intervertebral translations less than 2 mm at L1-2 through L5-S1; however, these measurements were of the anteroinferior and posteroinferior corners of the vertebral bodies taken from radiographs and were in two dimensions (2D) only [12]. A rigid body model has predicted segmental and intersegmental displacements of similar magnitude (range: 0.67-1.55 mm and 0.79-1.13 mm, respectively) in response to a PA impulse load of 100 N [13]. In a feasibility study [14], PA impulses were applied to the T11 through L3 spinous processes while measuring the intervertebral axial displacements, PA shear displacements, and flexion-extension rotations. The study was limited to three subjects (one normal and two undergoing spine surgery), and the magnitudes of the rotations and translations were relatively small (range: 0.13-0.9º and 0.25-1.62 mm, respectively). Although these studies provide useful information about the biomechanics of SM, the kinematics of the lumbar vertebrae using six degrees of freedom (DoF) during SM have never been quantified.

The vertebral motions that develop during SM load the FJC. The application of a HVLA SM in the L3 - L5 region can result in “gapping” of the L3-4, L4-5, and/or L5-S1 facet joints [15]. The audible “crack” that often accompanies HVLA SM is believed to originate from a rapid distention of the facet joint surfaces causing cavitation within the synovial fluid [16]. Both phenomena imply that the FJC undergoes deformation (strain) during SM, though this has never been observed nor quantified.

The FJC is innervated with mechanoreceptors and mechano-nociceptors [17], and FJC strains (or stresses) during SM may be sufficient to stimulate these neurons. Mechanoreceptors innervating paraspinal tissues in cats responded in a graded fashion to the direction of an innocuous load applied to a lumbar vertebra [18]. Simulated SM can either increase or decrease the discharge of neurons innervating paraspinal tissues [19]. Large strains during SM may stimulate FJC mechano-nociceptors. Alternatively, high FJC strain rates could provide a novel stimulus for FJC mechanoreceptors [20].

The purpose of the current study was to measure FJC plane strains during physiological motions and simulated SM. It was hypothesized that simulated SM would result in FJC strain magnitudes within the range that occur during physiological motions, which would indicate that SM was a “biomechanically safe” procedure. It was also hypothesized that FJC strain magnitudes would be independent of manipulation site, which would indicate that the effects of SM may also occur distal to the manipulation site. Preliminary data have been presented in abstract [21] and thesis [22] form.

Methods

Preparation of specimens

Intact human lumbar spine specimens (n = 7; mean age: 64.3 years ± 4.2 SD; range: 60-73; sex: 6 males, 1 female) were shipped frozen from the National Disease Research Interchange (Philadelphia, PA). Specimens (T12 - sacrum) were unembalmed and procured within 24 hours post-mortem from donors without history of spine pathology. All specimens were x-rayed (anterior-posterior and lateral views) to verify that they did not exhibit any gross pathology or substantial scoliosis (i.e., >9°). Prior to testing, the spines were dissected free of all superficial soft tissue (including insertions of multifidi muscles) to expose the FJC. Spinous processes were removed to facilitate the imaging of markers attached to FJC surfaces for plane strain measurements. Specimens were oriented such that the L3 and L4 endplates were horizontal to the testing surface, and were potted at the sacrum using a quick setting epoxy (Bondo©). Throughout testing, specimens were kept moist by periodic spraying with phosphate buffered saline (PBS, pH=7.4) and by wrapping them in PBS-soaked gauze.

Physiological motions

The spines were tested during physiological motions of extension, flexion, left lateral bending, and right lateral bending using methods previously described in detail [23,24]. Briefly, the sacrum was rigidly fixed to the testing surface, and the T12 vertebral body was connected to a rod via a rigid U-shaped coupling with a pin through the middle of the vertebral body, allowing a single degree of freedom (Fig. 1A). The coupling was in series with a force transducer (Model XLS1-150, Load Cell Central, Monroeton, PA;

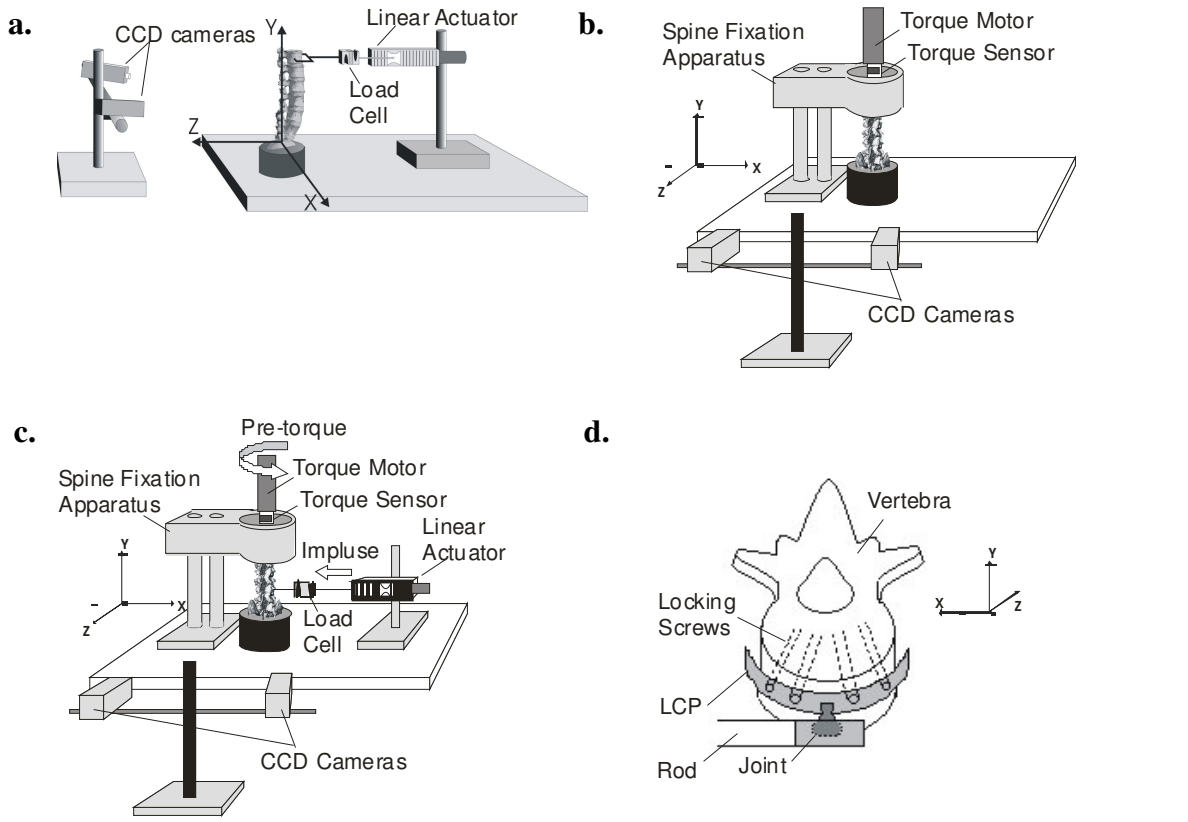

Figure 1 Schematics of the experimental setups. For all testing protocols, vertebral kinematics and facet joint capsule strains were measured by optically tracking infrared reflective markers using the two charge coupled device (CCD) cameras. The orientation axes of the system are shown for each view. **a)** Specimens were tested during physiological motions of extension, flexion, and lateral bending using a displacement-controlled linear actuator motor. A load cell was in series with the motor to measure the applied load. **b)** Spine specimens were tested during physiological motions of axial rotations using a torque motor, which was in series with a torque sensor to measure the applied torque. **c)** Spine specimens were tested during simulated spinal manipulation (SM) using both the torque motor and linear actuator motor. The torque motor was used to apply a pre-torque to the specimen to simulate patient position, and a custom-built spine fixation apparatus was used to hold the specimen in place during mechanical testing. During SM simulations, the linear actuator motor was used to deliver the impulse load to L_3, L_4, and L_5. The direction of the pre-torque and the manipulation are shown. **d)** During simulated SM, the linear actuator motor was attached to the anterior aspect of the vertebral body of interest using a Synthes Small Fragment Locking Compression Plate (LCP). The LCP was attached to a joint (allowing 30^0 of rotation), which was connected to the linear actuator via a rod.

range ±660 N, resolution 0.07 N) mounted to a linear actuator (Model ME3528-406C, Galil, Inc., Rocklin, CA) by a low friction universal joint. As the spine was actuated,

loads were applied without inducing a moment at the point of application. For all four motion types, a trial consisted of 10 cycles to 40 mm displacement (at T12) at 10 mm/s. The magnitude of global spine displacement was selected from the prior study [23] as that which was largest in magnitude while producing moments at L5-S1 below a predetermined limit of 10 Nm (a threshold beyond which can produce load-displacement relationships suggestive of damage to soft tissues of the spine [25]).

After specimens were tested during motions of extension, flexion, and lateral bending, the spine specimens were prepared for testing during physiological motions of left and right axial rotation (Fig. 1B). Specimens were potted at T12 using the same quick-setting epoxy used to pot the sacrum. Once the sacrum was locked to the testing surface, an aluminum plate (12 cm diameter, 0.6 cm thick) was secured to the epoxy at T12 using at least three self-tapping machine screws. The plate had a ¾", 3 cm high 6-point bolt soldered to its surface, and the bolt was connected to a ¾" socket that was in series with a torque transducer (Model TTD400, Futek, Irvine, CA) and a torque motor (ME2130-198B, Galil, Inc., Rocklin, CA). Mechanical testing consisted of 15 cycles to 20º left and right axial rotation (at T12) at 6º/sec. The magnitude of displacement was determined in preliminary studies [22] as the largest displacements that reliably produced torque measurements below the predetermined threshold of 10 Nm [25].

Impulse Loading

Preconditioning procedure

The lumbar spine is a viscoelastic structure, though its elastic properties have been studied more extensively [26]. In order to produce more reliable load-displacement curves, specimens were preconditioned before impulse loading. A 10 Nm torque was applied to T12 and held for 10 seconds, then released, and the angle of rotation was recorded. An intertrial interval of 3 minutes was used to allow the specimen to return to the physiological state [23,24]. The procedure was repeated until the angular displacement was the same for three consecutive torque applications (±0.1º). A torque of 10 Nm was chosen for the preconditioning procedure to ensure that the pre-torque magnitudes used to simulate patient positioning (5 and 10 Nm) would be within the pseudo-elastic range and that the specimen would not relax under the constant pre-torque during mechanical testing (see below).

Mechanical Testing

After preconditioning, the sacrum remained locked to the testing surface and the torque motor was used to apply a pre-torque (0, 5, or 10 Nm about the +Y-axis) to the specimen at T12 (Fig. 1C). The purpose of the pre-torque was to simulate different degrees of patient positioning, typical of in vivo lumbar SM [6]. The 0 Nm pre-torque simulated a side-lying patient, and the 5 and 10 Nm pre-torques simulated increasing degrees of pelvic rotation, respectively. After the pre-torque was applied, the superior portion of the specimen was locked into the spine fixation apparatus. Then, the linear actuator was attached to the anterior aspect of the L3 vertebral body using a Synthes Small Fragment Locking Compression Plate (LCP, Synthes, USA, Paoli, PA; Fig. 1D). The LCP was connected to a swivel-head joint (which allowed 30° rotation), and the

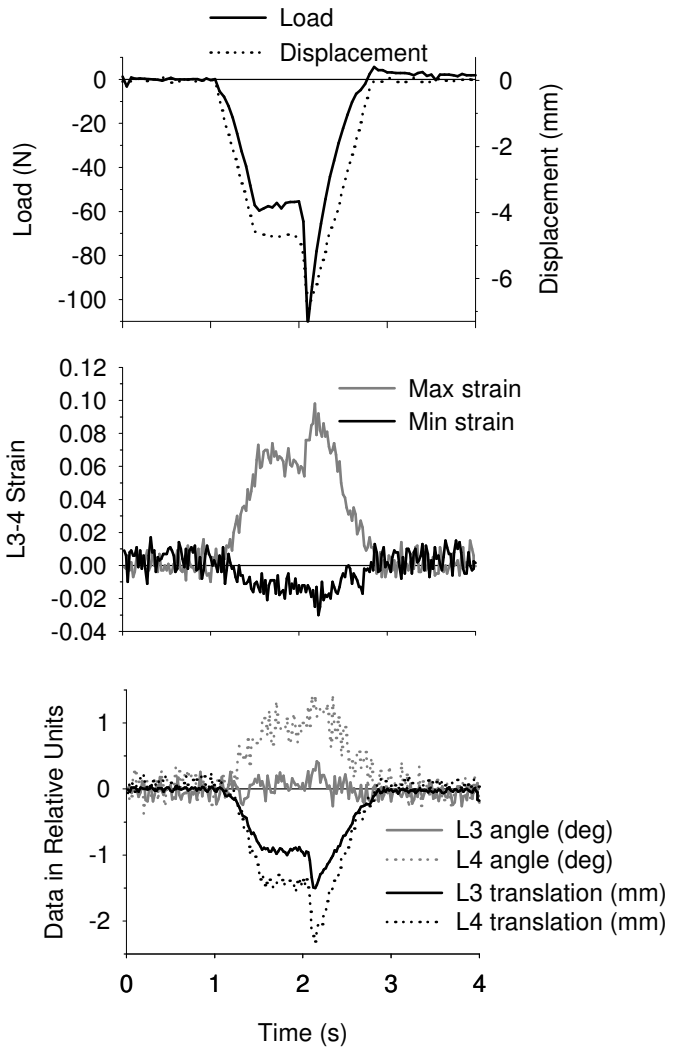

Figure 2 Representative data from a simulation of spinal manipulation applied to the anterior aspect of L4, which simultaneously produced rotation (+Y-axis) and translation (-X-axis) of the vertebrae (see Fig. 1 for orientation axes). a) A single trial consisted of 7 mm total displacement, which was comprised of a preload (maintained for 500 ms) and peak impulse. In the trial shown, the impulse was delivered at 50 mm/s. b) Facet joint capsule maximum (max) and minimum (min) principal strains (left L3-4 capsule strains shown) were typically opposite in sign. c) Vertebral kinematics (Y-axis rotations and X-axis translations of L3 and L4 are shown) were measured using six degrees of freedom, and the dominant vertebral motions occurred in the direction of the applied manipulation. Load-time, strain-time and vertebral motion-time

joint was attached to a threaded rod in series with the force transducer and the linear actuator. The spine was actuated at L3 by applying an impulse load parallel to the X-axis, creating simultaneously translation and rotation of the vertebrae.

SM simulations consisted of a pre-load phase (to simulate positioning of the joint near the limits of its range of motion) and a peak impulse (to simulate the impulse force administered) [8-11]; the entire simulation consisted of 7 mm total displacement (Fig. 2). During the preload phase, the actuator was displaced 2/3 the total displacement (4.66 mm) at 10 mm/s and held for 500 ms. Then, the peak impulse was applied by displacing the remaining 1/3 of the total displacement (2.44 mm) at 5, 20, or

50 mm/s, after which the actuator was returned to its initial position. The speed and displacement magnitudes were determined in preliminary studies [22] as those that were the best combination to achieve load magnitudes (50 – 400 N) and impulse durations (~200 ms) within the range that occur during SM in vivo [11], while considering the strength of the coupling to the vertebral body and the limits of the actuator motor.

The six DoF kinematics of the vertebrae (L3, L4, and L5) were optically measured, using a commercial kinematic system (Model 50, Qualisys, Inc., Gothenburg, Sweden), by imaging at 50 Hz (using two charge coupled-device cameras) the displacements of sets of three non-collinear markers fixed to the transverse processes (TP) of the vertebrae. Using the same cameras, the three dimensional (3D) displacements of markers attached to the FJC were tracked for subsequent plane strain calculations. The impulse was applied to L3 using all combinations of pre-torque and speed while imaging markers attached to the L3-4 through L5-S1 FJCs and the L3, L4, & L5 TPs on the right side of the spine. Next, the LCP was moved to the anterior aspect of the L4 vertebra and the protocol repeated, then the procedure was repeated again at the L5 vertebra. The right FJCs were then covered with PBS-soaked gauze and the left FJC's and TP's were imaged while applying the impulse to L5, L4, and finally to L3. The FJC plane strains (L3-4 through L5-S1) and vertebral motions (6 DoF, L3 through L5) at peak impulse were determined, both relative to the neutral and pre-torque positions of the spine.

Data Analysis and Statistics

Vertebral Kinematics

Using the method of Soderkvist and Wedin [27], vertebral angles and translations, relative to the vertical neutral or pre-torqued position of the spine, were computed using the 3D displacements of the markers attached to the TPs. Since the vertebrae were treated as rigid bodies, the vertebral angles and translations for a given combination of pre-torque, manipulation site, and speed were taken as the mean respective value measured while tracking the right and left sides of the spine. Motions for each degree of freedom were computed both relative to the neutral and pre-torqued position of the spine (to determine the amount of motion that occurred during the pre-torque application and during application of the impulse, respectively). The magnitudes of the total vertebral translations were computed by taking the square root of the sum of the squared displacements along the X-, Y-, and Z-axes for that vertebra.

Plane Strain Calculations

FJC plane strains were measured using methods previously described in detail [23,24]. Briefly, capsule plane strains (Lagrangian large strain formulation) were measured by optically tracking the displacements of infrared reflective markers (1 mm radius) glued to capsule surfaces. Capsule markers were typically placed as 3 x 3 arrays forming four quadrilaterals, from which plane (ε_{xx}, ε_{yy}, ε_{xy}) and principal strains (E1 and E2, defined as the principal strains whose directions were closest to the X-axis and Y-axis, respectively) were calculated for each quadrilateral element relative to the vertical neutral or pre-torqued position of the spine. As has been done in studies of FJC strains

in the cervical [28] and lumbar [23,24] spines, E1 and E2 were organized as either "maximum" (positive) or "minimum" (negative) principal strains (hereafter denoted as $\hat{E}_1$ and $\hat{E}_2$, respectively) regardless of their respective absolute magnitudes. Mean FJC $\hat{E}_1$ and $\hat{E}_2$ were computed as the mean of the respective values from the quadrilateral elements.

During physiological motions of extension, flexion, and lateral bending, strain data for the FJCs on both the right and left sides of the spine were computed for the first three specimens. Preliminary analyses indicated that there were no significant differences between the strains on the right and left FJCs (Mann-Whitney Rank Sum Test, $p>0.05$; SigmaStat Version 2.03, SPSS, Inc., Chicago, IL), so for the remaining spines, strain data was collected for the left FJCs only. Strain data from the right and left sides of the first three spines during flexion and extension were averaged. Similarly, strains during lateral bending were organized as tensile bending (left bending on the right FJCs and right bending on the left FJCs) and compressive bending (right bending on the right FJCs and left bending on the left FJCs) and then averaged. Because of the mirror symmetry observed during lateral bending in these preliminary analyses, as well as in prior studies [23], strain data on the left FJCs only were collected during axial rotations. During simulated SM, strain data on both sides of the spine were collected as described above. Total FJC strain during a given combination of pre-torque magnitude, speed, and manipulation site was computed as the sum of the strain that occurred during the pre-torque application and the strain at peak impulse.

Statistics

Mean loads during simulated SM were reported for the preload and the total (i.e., peak) load. Moments during the preload and at peak impulse of the simulated SM were calculated as the products of the respective load magnitudes and the moment arms. The moment arm was measured, using digital calipers (Model 14-648-17, Control Company, Friendswood, TX; 0.01 mm resolution), as the perpendicular distance between the point load application (i.e., at the joint on the coupling) to the estimated center of rotation of the manipulated vertebra [29,30]. All statistical analyses were performed using SigmaStat (Version 2.03, SPSS, Inc., Chicago, IL). Significant differences in preload and peak impulse load and moment were calculated using a three factor analysis of variance (ANOVA, factors: manipulation site, speed, and pre-torque magnitude; $\alpha=0.05$) with post-hoc Tukey tests ($\alpha=0.05$). Preliminary analyses demonstrated that there were no significant differences in FJC strains or vertebral kinematics across impulse speed, so for each combination of manipulation site and pre-torque magnitude the mean respective value was determined. A two factor repeated measures analysis of variance (RM-ANOVA) with post hoc Tukey tests ($\alpha=0.05$) was used to detect significant differences in total FJC strain, vertebral translation, and vertebral rotation across manipulation site and pre-torque magnitude.

Results

Spine Specimens

No gross pathologies of the spine specimens were evident by visual inspection or on plain film x-rays. Capsules were visually inspected at low power magnification (6x) and

were found to be intact, exhibiting characteristic gross normal appearance including white color and a predominantly medial to lateral orientation of collagen fibrils [31]. One spine specimen was potted at the sacrum such that it was difficult to attach the LCP to the anterior aspect of L5, so for this spine the manipulations were applied to L3 and L4 only. Because repeated measures statistical tests were used, this specimen was omitted from the analysis of the FJC strain and vertebral kinematics data (i.e., it was used in the analyses of load and moment data only).

Load and Moment

Loads during simulated SM (Fig. 3) were within the range measured in vivo [8-11]. Mean load magnitudes during the preload phase ranged from 61 - 152 N, while mean total load magnitudes ranged from 86 - 230 N. Load magnitudes during the preload and total (i.e., peak) load magnitudes varied significantly with manipulation site (ANOVA,

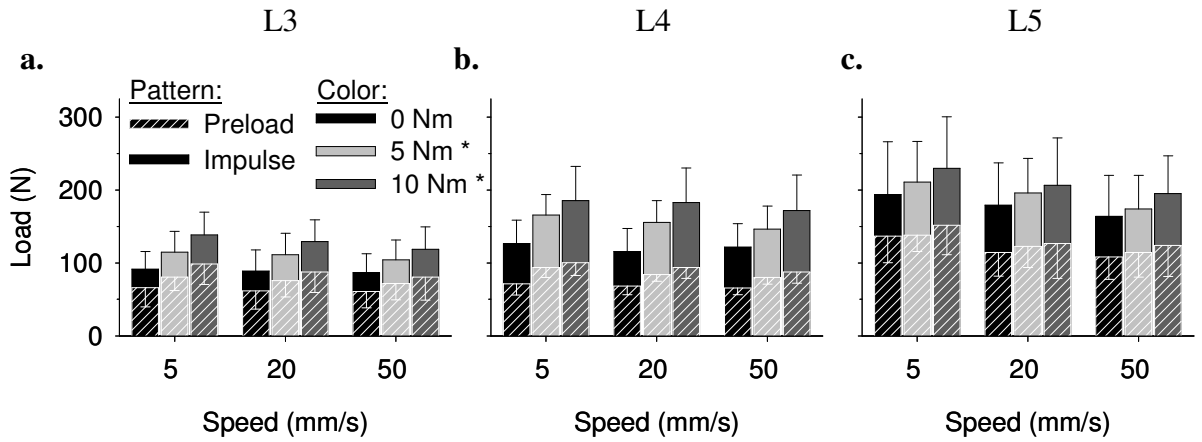

Figure 3. Load magnitudes during simulated manipulations of the lumbar spines (n=7) were site-specific (manipulation sites: **a**) L3, **b**) L4, **c**) L5). Both preload and total load magnitudes at L4 and L5 were significantly larger than those that occurred at the respective more superior vertebrae (3-way ANOVA, $p<0.001$). Preload and total load magnitudes did not vary significantly with speed (ANOVA, $p=0.075$). *Both preload and total load magnitudes were larger with 5 Nm and 10 Nm pre-torque versus 0 Nm pre-torque (3-way ANOVA, $p < 0.001$).

p<0.001), where loads at a given vertebra were significantly larger than those that occurred at the more superior vertebrae in both cases (Tukey, $p < 0.05$). Preload and total load magnitudes varied significantly with pre-torque magnitude (ANOVA, $p < 0.001$), and both preload and total load magnitudes were significantly larger with 5 Nm and 10 Nm pre-torque versus 0 Nm pre-torque (Tukey, $p < 0.05$). Impulse speed did not have a significant effect on preload or total load magnitude (ANOVA, $p > 0.07$). There were no significant interactions among manipulation site, pre-torque magnitude, and impulse speed (ANOVA, $p > 0.61$).

Mean moment during the preload ranged from 3.9 - 8.1 Nm, while the mean moments at peak impulse ranged from 5.2 - 11.5 Nm (Fig. 4). The applied moments during the preload phase and at peak impulse varied significantly with manipulation site (ANOVA,

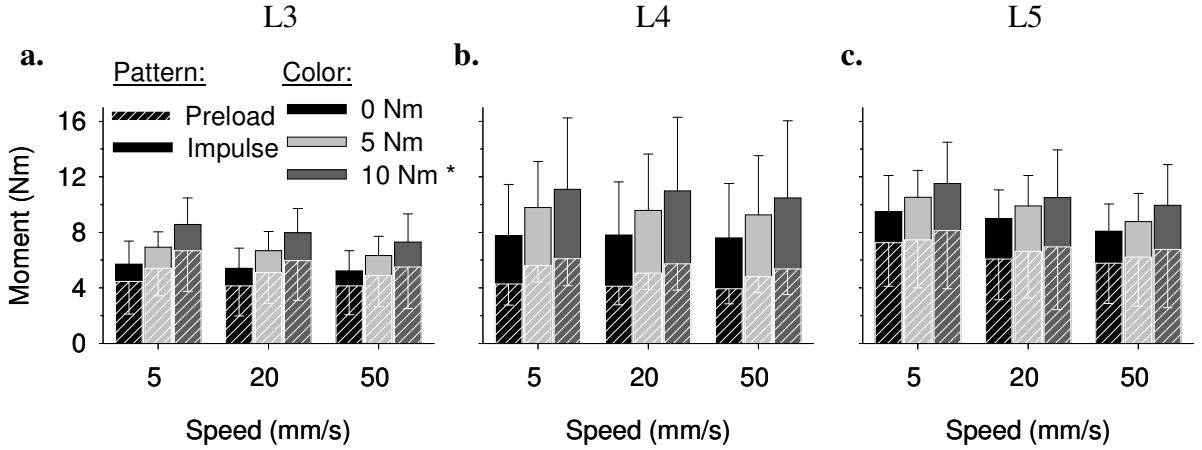

Figure 4. Preload and total moment magnitudes during simulated manipulations of the lumbar spines (n=7) were site-specific (manipulation sites: **a**) L3, **b**) L4, **c**) L5). L4 and L5 moments (both preload and total) were significantly larger than L3 moments (3-way ANOVA, $p < 0.001$). Preload and total moment magnitudes did not vary significantly with speed (ANOVA, $p > 0.07$). *Both preload and total moment magnitudes were larger with 10 Nm pre-torque versus 0 Nm pre-torque (3-way ANOVA, $p < 0.001$)

$p < 0.001$); the moments at L4 and L5 were significantly larger than those that occurred at L3 (Tukey, $p < 0.05$). Preload and total moment magnitudes varied significantly with pre-torque magnitude (ANOVA, $p < 0.02$), with larger moments occurring with 10 Nm pre-torque versus 0 Nm pre-torque (Tukey, $p < 0.05$). There were no significant differences in moment across impulse speeds (ANOVA, $p > 0.2$), nor were there any significant interactions among manipulation site, pre-torque magnitude, or impulse speed (ANOVA, $p > 0.92$).

Vertebral Translation

L3, L4, and L5 vertebral translations occurred predominantly in the direction of the applied impulse (-X-axis; Fig. 5). Translations along the other two axes were relatively small in absolute magnitude and were more variable than those along the dominant axis. Vertebral translations along a given axis and the total vertebral translations did not vary significantly with pre-torque magnitude or manipulation site (ANOVA, $p > 0.05$), and there were no significant interactions between pre-torque magnitude and manipulation site (ANOVA, $p > 0.10$).

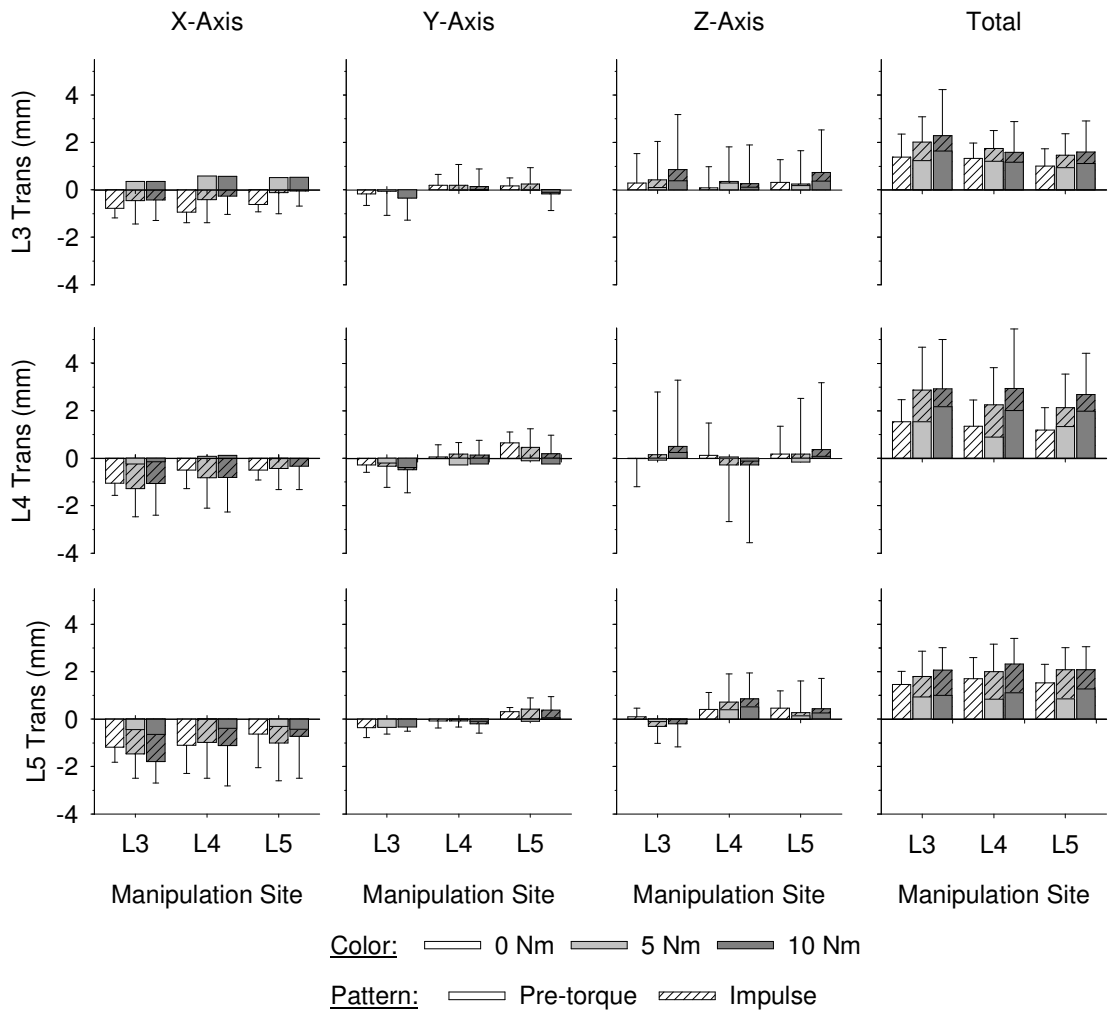

Figure 5. Vertebral translation (trans) magnitudes during simulated manipulations of lumbar spines (n = 6) were not site specific. Compared to the translations along the Y- and Z-axes, translations were larger in absolute magnitude along the X-axis (the direction of the applied impulse). Total vertebral translations were computed as the vector sum of the translations that occurred along the three axes. Total vertebral translations and the translations that occurred along a given axis were of similar magnitude, regardless of whether the manipulation was applied locally or distally (ANOVA, $p > 0.05$). Vertebral translations also did not vary with pre-torque magnitude (ANOVA, $p > 0.05$).

Vertebral Rotation

L3, L4, and L5 vertebral rotations during SM (Fig. 6) were within the range that occurred during physiological motions (Table 1). L3, L4, and L5 vertebral rotations were relatively small about the X-axis (Fig. 6). L3, L4, and L5 X-axis rotations did not vary significantly with pre-torque magnitude (ANOVA, $p > 0.3$) or manipulation site (ANOVA, $p > 0.25$).

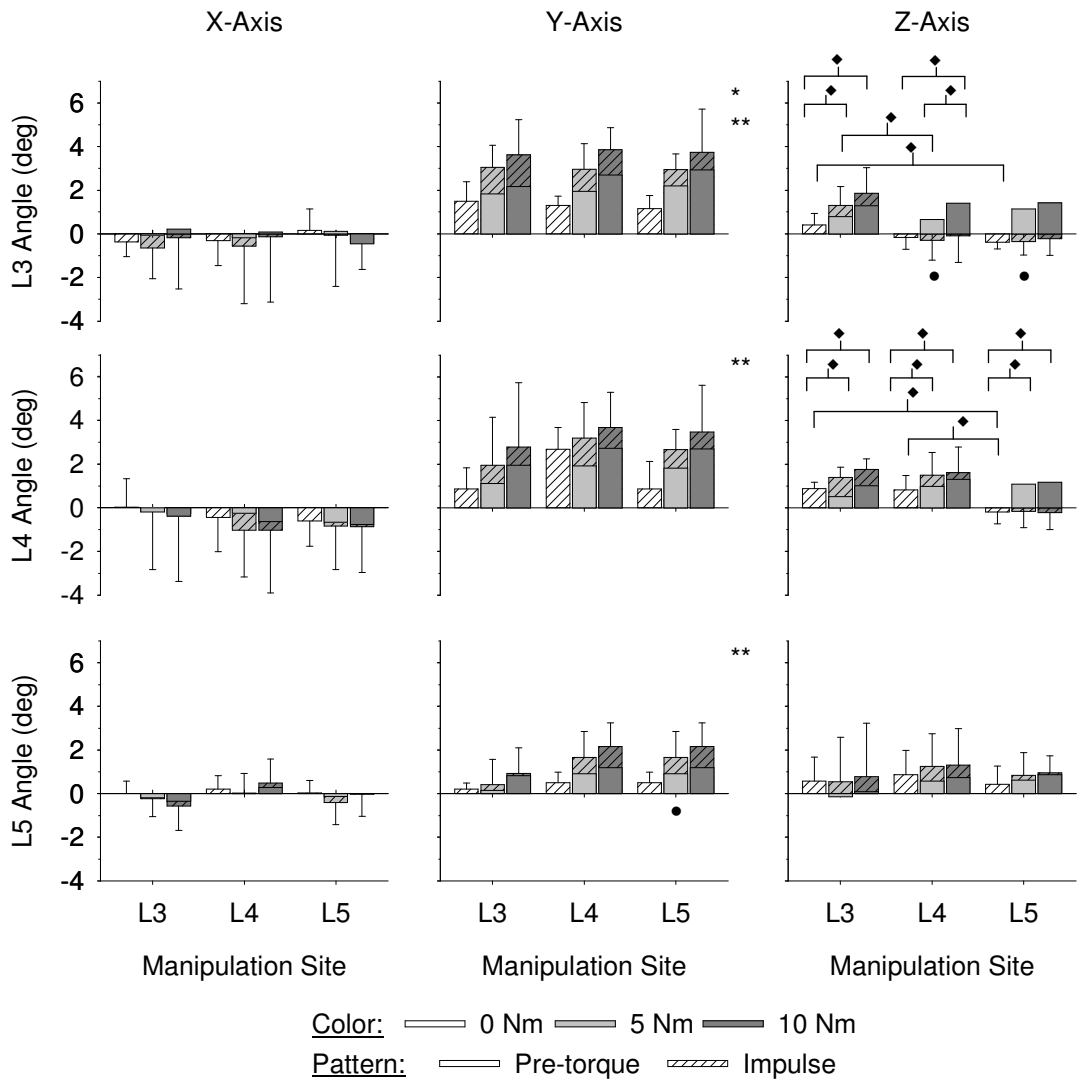

Figure 6. Site-specific lumbar spine manipulations (n = 6) induced vertebral rotations both locally and distally. X-axis rotations (see Fig. 1 for orientation axes) were relatively small in absolute magnitude and were highly variable. At a given vertebra, and for a given combination of manipulation site and pre-torque magnitude, rotations were typically largest in absolute magnitude about the Y-axis, which was the direction of the applied pre-torque and impulse load. Z-axis rotations were relatively small; at L_3 and L_4 the magnitude and direction of z-axis rotations were dependent upon pre-torque magnitude and manipulation site. *5 Nm pre-torque significantly larger than 0 Nm pre-torque (ANOVA, $p < 0.015$). **10 Nm pre-torque significantly larger than 0 Nm pre-torque (ANOVA, $p < 0.015$). •Significantly different versus L_3 manipulation site (ANOVA, $p < 0.03$). □Significant interactions between pre-torque and manipulation site (ANOVA, $p < 0.035$).

Axis	X			Y			Z		
Motion	L3	L4	L5	L3	L4	L5	L3	L4	L5
E	7.8 (4.2)	6.0 (3.1)	3.4 (1.7)	3.2 (2.8)	0.9 (1.1)	-0.2 (0.8)	3.1 (3.1)	1.6 (2.9)	0.5 (0.8)
F	-10.5 (3.8)	-6.6 (3.2)	-2.1 (3.1)	-2.1 (2.8)	-1.4 (1.9)	0.1 (1.1)	-0.9 (1.7)	-1.0 (1.5)	-0.8 (1.2)
LB	-4.2 (3.6)	-0.7 (1.8)	-0.4 (1.3)	1.0 (3.5)	0.0 (2.0)	-0.4 (1.3)	10.9 (1.6)	7.7 (1.0)	3.5 (1.0)
RB	0.8 (4.2)	1.0 (2.1)	0.0 (1.1)	0.4 (4.1)	0.2 (3.9)	0.5 (0.7)	-10.5 (2.8)	-7.0 (2.4)	-3.8 (1.1)
LA	0.9 (1.5)	-0.4 (3.8)	0.3 (0.5)	2.0 (2.7)	2.1 (2.2)	0.7 (1.3)	1.1 (2.2)	1.2 (1.6)	0.9 (0.9)
RA	-0.5 (1.7)	0.4 (3.3)	0.0 (0.3)	-1.7 (2.8)	-1.2 (1.5)	-0.7 (1.4)	-1.2 (1.3)	-1.4 (0.8)	-1.0 (0.8)

Table 1. Mean vertebral rotations (in degrees) of the lower lumbar vertebrae during physiological motions. Standard deviations shown in parentheses. Motions were as follows: E –extension, F – flexion, LB – left lateral bending, RB – right lateral bending, LA – left axial rotation, and RA – right axial rotation.

There were no significant interactions between manipulation site and pre-torque magnitude at L3, L4, or L5 (ANOVA, $p > 0.80$).

For a given combination of pre-torque magnitude and manipulation site, Y-axis vertebral rotations were typically largest in absolute magnitude compared to those that occurred about the other two axes (Fig. 6). Y-axis rotations at L3, L4, and L5 varied significantly with pre-torque magnitude (ANOVA, $p < 0.01$). L3 Y-axis rotations were significantly larger with 5 Nm and 10 Nm pre-torque versus 0 Nm pre-torque (Tukey, $p < 0.05$). At L4 and L5, Y-axis rotations were significantly larger with 10 Nm pre-torque versus 0 Nm pre-torque (Tukey, $p < 0.05$).

Y-axis rotations at L3 did not vary significantly with manipulation site (ANOVA, $p = 0.922$). L4 Y-axis rotations also did not vary significantly with manipulation site (ANOVA, $p = 0.213$), although at a given pre-torque the mean rotations appeared larger when the manipulation was applied to L4. At L5, Y-axis rotations varied significantly with

manipulation site (ANOVA, $p = 0.021$), and were larger in magnitude when the manipulation was applied at L5 versus at L3 (Tukey, $p < 0.05$). There were no significant interactions between manipulation site and pre-torque magnitude at L3, L4, or L5 (ANOVA, $p > 0.17$).

Although smaller in absolute magnitude, vertebral rotations about the Z-axis demonstrated more significant trends than did those about the Y-axis (Fig. 6). L3 and L4 Z-axis rotations varied significantly with pre-torque magnitude (ANOVA, $p < 0.001$); Z-axis rotations with 5 Nm and 10 Nm pre-torque were significantly larger than those with 0 Nm pre-torque (Tukey, $p < 0.05$). L5 Z-axis rotations were not significantly affected by pre-torque magnitude (ANOVA, $p = 0.148$). L3 Z-axis rotations varied significantly with manipulation site (ANOVA, $p = 0.027$), with larger angles occurring when the manipulation was applied at L3 versus at L4 or L5 (Tukey, $p < 0.05$). Manipulation site did not have a significant effect on L4 or L5 Z-axis rotations (ANOVA, $p > 0.06$).

While there were no significant interactions between pre-torque magnitude and manipulation site in L5 Z-axis rotations (ANOVA, $p = 0.820$), L3 and L4 Z-axis rotations exhibited significant interactions (ANOVA, $p < 0.03$). At L3, Z-axis rotations with 0 Nm pre-torque were significantly different when the manipulation was applied to L3 versus at L5 (Tukey, $p < 0.05$); although the absolute magnitudes of the angles were similar, they were opposite in sign (and hence direction). With 5 Nm pre-torque, L3 Z-axis rotations were significantly larger when the manipulation was applied to L3 versus at L4 (Tukey, $p < 0.05$). When the manipulation was applied at L4, L3 Z-axis rotations were

significantly larger with 10 Nm pre-torque versus 5 Nm and 0 Nm pre-torque (Tukey, $p < 0.05$). When the manipulation was applied at L3 and L5, the L3 Z-axis rotations were significantly larger with 5 Nm and 10 Nm pre-torque versus 0 Nm pre-torque (Tukey, $p < 0.05$).

L4 Z-axis rotations exhibited significant interactions at 0 Nm pre-torque and at all three manipulation sites (ANOVA, $p = 0.01$). With 0 Nm pre-torque, L4 Z-axis rotations were significantly larger when the manipulation was applied at L4 and L3 versus L5 (Tukey, $p < 0.05$). At all three manipulation sites, L4 Z-axis rotations were significantly larger with 5 Nm and 10 Nm pre-torque versus 0 Nm pre-torque (Tukey, $p < 0.05$).

Facet joint capsule plane strains

$\hat{E}_1$ *Strains (Maximum)*

Mean $\hat{E}_1$ FJC plane strains during simulated SM on the left and right sides of the spine were similar in magnitude (Fig. 7). On the left side of the spine, L3-4 $\hat{E}_1$ strains varied significantly with pre-torque magnitude (ANOVA, $p = 0.002$), where $\hat{E}_1$ FJC strains were larger with 5 Nm and 10 Nm pre-torque versus 0 Nm pre-torque (Tukey, $p < 0.05$). $\hat{E}_1$ strains in the left L4-5 and L5-S1 FJCs also varied significantly with pre-torque magnitude (ANOVA, $p < 0.03$), where larger strain magnitudes occurred with 10 Nm pre-torque versus 0 Nm pre-torque (Tukey, $p < 0.05$). There were no significant differences in $\hat{E}_1$ strain magnitudes with pre-torque magnitude on the right side of the spine (ANOVA, $p > 0.05$).

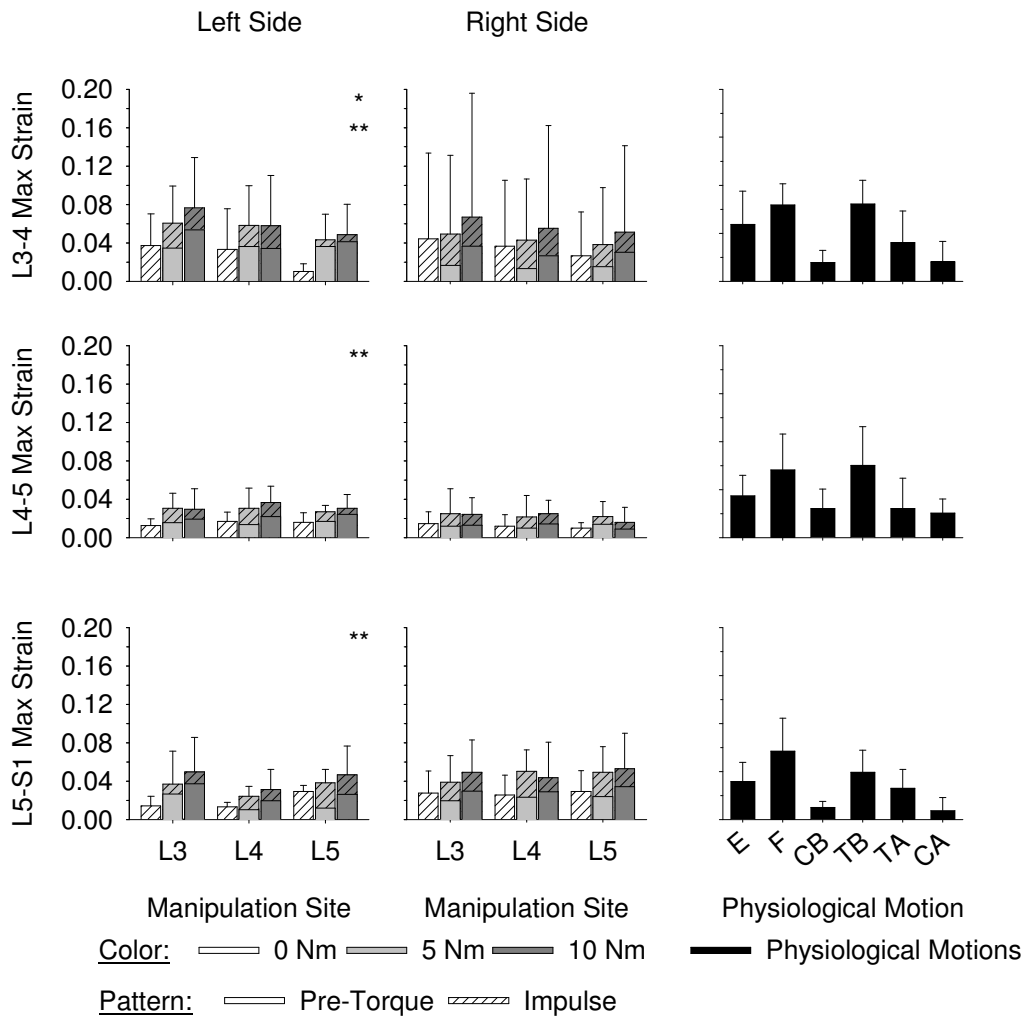

Figure 7. Facet joint capsule (FJC) maximum (max) principal strains ($\hat{E}_1$, n = 6) **a)** during simulated spinal manipulation (SM) were within the range that occurred **b)** during physiological motions of extension (E), flexion (F), lateral bending (CB – compressive bend, TB – tensile bend), and axial rotations (TA – tensile axial, CA – compressive axial). During SM, FJC strains on both sides of the spine were induced regardless of whether the manipulation was applied distally or locally (ANOVA, $p > 0.13$). On the left side of the spine, FJC strain magnitudes were larger with 5 Nm (*) and 10 Nm (**) pre-torque versus 0 Nm pre-torque (ANOVA, $p < 0.03$).

On both sides of the spine, simulated SM induced $\hat{E}_1$ FJC strains distally (Fig. 7). There were no significant differences in mean $\hat{E}_1$ strain magnitudes with manipulation site at L3-4, L4-5, or L5-S1 (ANOVA, $p > 0.12$). There were also no significant interactions between pre-torque magnitude and manipulation site at any of the FJCs (ANOVA, $p > 0.28$).

Mean $\hat{E}_1$ strains during simulated SM were well within the range that occurred during physiological motions (Fig. 7). The largest mean $\hat{E}_1$ strains occurred during physiological motions of lateral bending (L3-4 and L4-5 FJCs) and flexion (L5-S1 FJC). Mean $\hat{E}_1$ strains during simulated SM were well within the 95% confidence intervals of the largest mean $\hat{E}_1$ strains during physiological motions at L3-4, L4-5, and L5-S1 (upper limit: 10.4%, 11.3%, and 11.5% strain, respectively).

$\hat{E}_2$ Strains (Minimum)

Mean $\hat{E}_2$ strains on the left L3-4, L4-5, and L5-S1 FJCs did not vary significantly with pre-torque magnitude (Fig. 8, ANOVA, $p > 0.19$). On the right side of the spine, mean $\hat{E}_2$ strains at L3-4 varied significantly with pre-torque magnitude (ANOVA, $p = 0.043$), where L3-4 $\hat{E}_2$ strains were larger in absolute magnitude with 10 Nm pre-torque versus 0 Nm pre-torque (Tukey, $p < 0.05$). At the L4-5 and L5-S1 FJCs on the right side of the spine, $\hat{E}_2$ strains were not significantly affected by pre-torque magnitude (ANOVA, $p > 0.09$).

On both sides of the spine, FJC $\hat{E}_2$ strains were induced distal to the applied manipulation (Fig. 8). Applying the manipulation distally did not significantly increase or decrease FJC mean $\hat{E}_2$ strain magnitudes (ANOVA, $p > 0.14$). There were no significant interactions between pre-torque magnitude and manipulation site at L3-4, L4-5, or L5-S1 (ANOVA, $p > 0.10$).

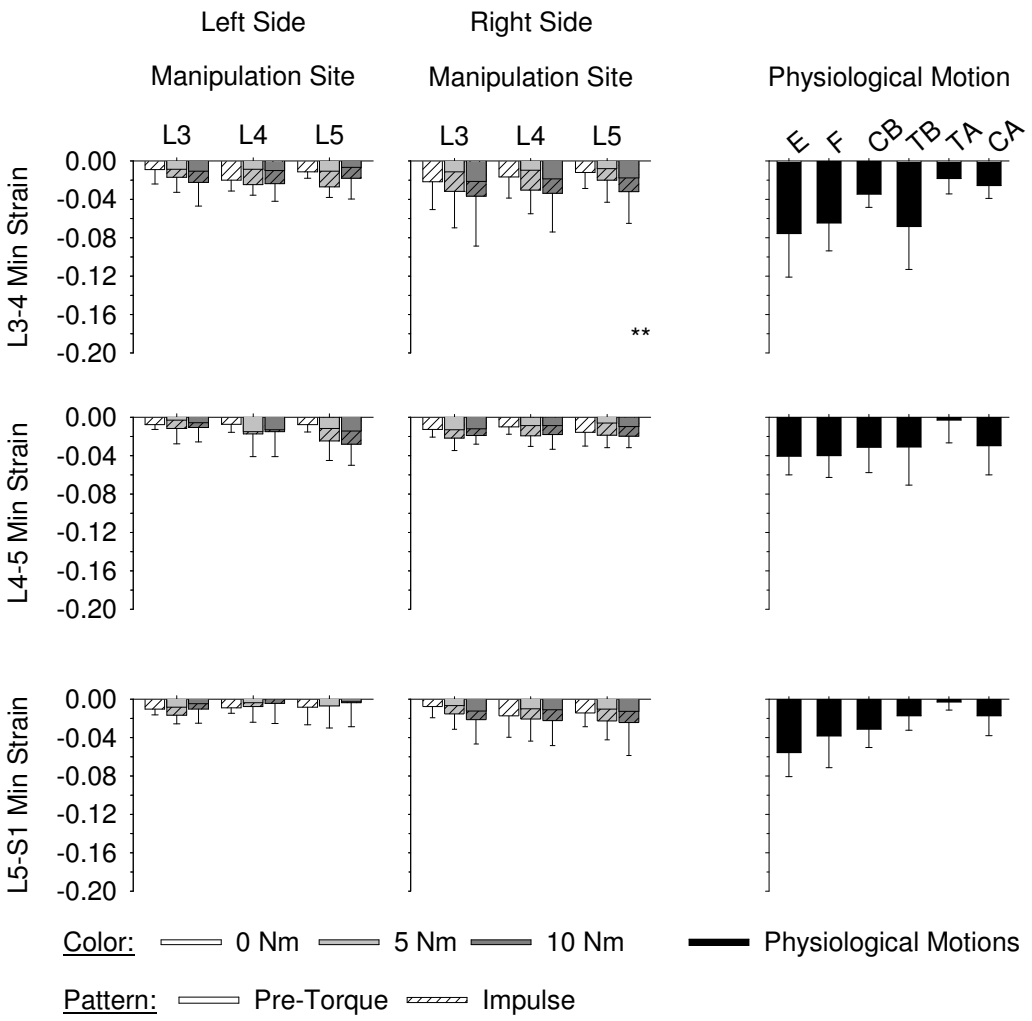

Figure 8. Facet joint capsule (FJC) minimum (min) principal strains ($\hat{E}_2$, n = 6) **a)** during simulated spinal manipulation were within the range that occurred **b)** during physiological motions of extension (E), flexion (F), lateral bending (CB – compressive bend, TB – tensile bend), and axial rotations (TA – tensile axial, CA – compressive axial). During SM, FJC strains on both sides of the spine were induced, regardless of whether the manipulation was applied distally or locally (ANOVA, $p > 0.14$). **10 Nm pre-torque significantly larger than 0 Nm pre-torque (ANOVA, $p < 0.05$).

Mean $\hat{E}_2$ strains during simulated SM were well within the range that occurred during physiological motions (Fig. 8). At all three joint levels, mean $\hat{E}_2$ strains were largest in absolute magnitude during physiological motions of extension. During simulated SM, mean $\hat{E}_2$ strains were always within the 95% confidence interval of $\hat{E}_2$ strains during

extension (upper limit: -11.8%, -6.4%, and -7.7% at L3-4, L4-5, and L5-S1, respectively).

Discussion

This is the first report of simulated SM in human cadaveric spine specimens while simultaneously measuring lumbar FJC plane strains and vertebral kinematics using six DoF. Loads and vertebral motions during simulated SM were similar in magnitude to those reported for in vivo SM [6,11,32]. SM FJC principal strains were within the range that occurred during physiological motions, implying that SM is biomechanically safe and provides an innocuous mechanical stimulus for FJC mechanically-sensitive neurons. FJC strains were induced distal to the manipulation site, indicating that the theorized neurophysiological effects of SM elicited by FJC neuron firing [7] may be initiated distally as well.

Load and Moment

The simulated SMs in this study applied forces within the range of in vivo SM [11]. However, the mean applied moments during the preload phase and at peak impulse were substantially smaller in magnitude (3.9 – 8.1 Nm, and 5.2 - 11.5 Nm, respectively) than those predicted for in vivo SM (30 – 50 Nm, and 100 – 150 NM, respectively) [11]. Studies in the thoracic spine suggest that a large percentage of the force applied during SM is transmitted to the soft tissues (which were absent in this study) and not to the manipulated segment, due to an increase in contact area associated with an increase in applied force [33]. If this is also the case in the lumbar spine, then forces developed in

this study probably exceeded those that would be transmitted in vivo to the manipulated segment. In part, the difference between the measured and predicted moments may be because in this study the sacrum was fixed to the testing apparatus whereas during in-vivo HVLA SM, the pelvis can be further rotated. Regardless, the forces generated in this study were sufficient to achieve relative vertebral movements similar in magnitude to those that have been estimated to occur during in vivo HVLA-SM [11].

Vertebral motion

This is the first report describing lumbar vertebral motions during simulated SM using all six possible DoF. Others have measured thoracic 2D intervertebral motions in two orthogonal planes during cadaver SM and reported similar ranges of translation and rotations as measured in the current study [34-36]. Assessment of vertebral motions using all six DoF using a similar technique would require imaging three bone pins, or perhaps three noncollinear points on two bone pins, utilizing two cameras positioned at a smaller angle (ideally at 45°).

Tracking the motion of the vertebrae in 3D overcame limitations associated with other methods for determining vertebral motions. Though imaging modalities such as MRI [15,37] or x-ray [12] are less invasive, the frequency of data acquisition is low compared to the rate at which the loads are applied during HVLA-SM, and they provide information in 2D only. While the results of the current study show that the translations during SM occur primarily along a single axis, tracking vertebral motions in 3D eliminates errors due to motion out of plane. More importantly, in the current study substantial vertebral

rotations occurred about two axes; this information would have been missed if only 2D measurements were taken. The use of accelerometers has allowed for the determination of vertebral translation, by twice integrating the acceleration-time profile, about all three axes during in-vivo [38,39] and cadaver SM [40]. While data acquisition rate can be increased substantially compared to MRI or x-ray, the accelerometers used in the prior studies did not differentiate between linear and angular accelerations. Any rotation of the accelerometer off of its primary axis decreases the sensitivity of the measurement. Gal et al. [34] determined that accelerometers significantly overestimated absolute vertebral translations and significantly underestimated relative vertebral translations compared to those measured using bone pins. The method used in the current study was sufficient to discriminate between translation and rotation, and the data acquisition rate was sufficient to identify the magnitude of motion at peak impulse.

Intervertebral motions during spinal mobilization (i.e., low velocity low amplitude, and no impulse loading) [12,37,41] were similar in magnitude to those in the current study. However, vertebral translations during spinal mobilization tended to be much larger (range: 8.8-11.5 mm compared to only 0-2.3 mm in the current studies) [12]. This difference may have partially been due to the much longer durations of the applied loads (3 minutes in Lee and Evans [12]), which allowed the viscoelastic structures of the spine to “creep”. Additionally, the prior studies measured vertebral displacements during spinal mobilizations using transducers applied to the surface of the skin overlying the spinous processes. The large vertebral translations measured could have been due to

compression of the skin and subcutaneous fat overlying the mobilized segment, which could be as large as 10 mm [41,42].

Vertebral motions during HVLA SM have been studied in the thoracic spine [35]. The absolute translations of the thoracic vertebrae were larger than those observed in the current study (3 - 12 mm versus 0 - 2.3 mm, respectively), while intervertebral rotations were slightly smaller (0.2 - 1.8º versus 0.2 - 2.2º, respectively). In the prior study, a PA load (which would be along the Z-axis in the current study) was applied to the right transverse process of a thoracic vertebra. The difference in translation magnitudes may have been due both to the difference in load direction, as well as the morphological differences between the lumbar and thoracic spines (and hence relative stiffness).

In the current study, site-specific manipulations resulted in systemic biomechanical responses in the lumbar spine. Vertebral translations were similar in magnitude, regardless of whether the manipulation was applied distally or locally. This was in contrast to an in vivo study by Nathan and Keller [14], where L3-4 translations in a patient free of spine pathology increased nearly linearly as the load was applied closer to the joint (manipulations applied to T11 through L3). It is difficult to compare these results to those of the current study, since the prior study was limited to a single normal patient. Vertebral displacements probably would have decreased in the current study as well if the manipulations were applied more distally. In contrast to the vertebral translations, the magnitude of vertebral rotation in the current study depended upon whether the manipulation was applied locally or distally, particularly the Z-axis rotations.

These results concur with those of Powers et al. [37], where manipulation site had a significant effect on both the magnitude and direction of rotation.

FJC strains

The FJC strain magnitudes were at the high end of the range that occurred during physiological motions. Because human FJCs are innervated with low threshold mechanoreceptors and nociceptors [43], it suggests that the FJC could contribute to the theorized beneficial neurophysiological effect of SM [7]. In cat knee joint capsules, stretch-activated mechanoreceptors (Group II or Ruffini) had relatively low thresholds (~ 1-5 kPa) [44]. As the modulus of elasticity of human FJC is roughly 3 MPa [45], this threshold would be exceeded at even 1% strain of FJC. To the extent that human FJC afferents are similar to cat knee joint capsule afferents, it suggests that human low threshold capsule afferents would be stimulated during physiological motions and/or SM. The magnitude of the FJC strains developed during SM in the current study provides biomechanical evidence that supports the theory for the FJC's involvement in the beneficial neurophysiological effects of SM.

FJC strains during simulated SM did not exceed those that occurred during physiological motions, so it is also likely that SM is a procedure that is biomechanically safe and provides a stimulus that is sub-threshold for FJC mechano-nociceptors. Although FJC strain magnitudes during SM were similar to those that occurred during physiological motions, the high strain rates that occurred during SM could provide a novel mechanical stimulus for capsule mechanoreceptors. Mechanoreceptors

innervating rabbit lumbar FJC and paraspinal muscles responded to joint loading and loading rate, suggesting that these afferents could function as “velocity detectors” [20]. The high strain rates that occur during SM could provide a nonphysiological (yet, biomechanically safe) stimulus for human FJC afferents.

Although the paraspinal tissues overlying the FJCs were removed in order to measure FJC strains, the strain magnitudes in the current study were probably similar in magnitude to those that occur in vivo. Paraspinal static muscle tone and reflex contractions stiffen the spine, which could potentially decrease intervertebral motions during in vivo SM, and hence decrease FJC strains. Conversely, contraction of multifidus muscles, which have insertions on the FJC surface, could generate strain independent of those resulting from intervertebral motion itself [24]. However, the muscle reflex response during in-vivo HVLA SM is delayed by 50 - 200 ms after the application of the thrust [46], and the peak strains measured in the current study occurred at peak displacement. Hence, it is likely that the FJC strain magnitudes in this study were reasonable estimates of the FJC strains that occur during SM in vivo.

Despite the fact that vertebral rotations varied significantly in magnitude and/or direction with manipulation site, FJC strain magnitudes were similar regardless of where the manipulation was applied. This implies that segmental specificity may not be as important as previously postulated in the efficacy of SM [47,48]. Patients with neck pain who received SM had the same beneficial results regardless of whether the SM was targeted at a specific involved motion segment or performed generally to the cervical

spine [49]. During in vivo lumbar SM, cavitation phenomena (i.e., the audible “crack”) occurred in distal lumbar facet joints as frequently as in targeted joints [50]. Hence, the benefits of SM may not arise solely from the events that occur local to the manipulated facet joint.

There are several methodological factors to consider when interpreting the results of this study. First, the cadaver spines were obtained from an older population; lumbar spines from younger subjects tend to be more flexible and the FJC strain magnitudes for a given joint moment are larger (unpublished observations). Second, although every effort was taken to keep the specimens moist using PBS-soaked gauze and by misting the specimens with PBS, the FJCs were exposed directly to air for significant periods of time. Third, the tissues overlying the FJCs, as well as the spinous processes and its associated ligaments, were removed to enable viewing of FJC markers. Because the protocol was run under displacement control, this would not have affected the measurement of FJC strains or vertebral motions, but removal of these supporting structures could have resulted in smaller loads than develop in vivo. Because the vertebral motions in the current study were similar in magnitude to those that occur during SM in vivo [34-36], and as the magnitudes of intervertebral motion and FJC strain are related [23], it is likely that the FJC strains measured in the current study were similar to those that occur in vivo.

In conclusion, site-specific SM resulted in systemic biomechanical responses of the lumbar vertebrae. FJC strain magnitudes were at the high end of the range that

occurred during physiological motions; hence SM is likely a biomechanically safe procedure and sufficient to stimulate low threshold capsule mechanoreceptors. The high strain rates that occur during SM may provide a “non-physiological” stimulus that affects a pattern of mechanoreceptor firing, which may contribute to the theorized beneficial neurophysiological effect of SM. FJC strain magnitudes at the manipulated joint did not differ significantly from those that occurred when the manipulation was applied distally, suggesting that successful treatment of patients with LBP using SM may not require precise lumbar segmental specificity. Clinical and/or neurophysiological studies should be conducted in order to determine the efficacy of targeted manipulation in the lumbar spine.

Acknowledgement

The authors would like to thank Jesse Little for her assistance in data collection and processing. This project was funded by National Institutes of Health (NIH), National Center for Complementary and Alternative Medicine (NCCAM), Consortial Center for Chiropractic Research (CCCR) AT001701-05; CCCR subcontract (Khalsa).

Reference List

1. Hicks, G. S., Duddleston, D. N., Russell, L. D., Holman, H. E., Shepherd, J. M., Brown, C. A. Low back pain. Am.J.Med.Sci. 2002; 324(4):207-211.
2. Wolsko, P. M., Eisenberg, D. M., Davis, R. B., Kessler, R., Phillips, R. S. Patterns and perceptions of care for treatment of back and neck pain: results of a national survey. Spine 2003; 28(3):292-297.
3. Assendelft, W. J., Morton, S. C., Yu, E. I., Suttorp, M. J., Shekelle, P. G. Spinal manipulative therapy for low back pain. A meta-analysis of effectiveness relative to other therapies. Ann.Intern.Med. 2003; 138(11):871-881.
4. Bronfort, G. Spinal manipulation: current state of research and its indications. Neurol.Clin. 1999; 17(1):91-111.
5. Koes, B. W., Assendelft, W. J., van der Heijden, G. J., Bouter, L. M. Spinal manipulation for low back pain. An updated systematic review of randomized clinical trials. Spine 1996; 21(24):2860-2871.
6. Triano, J. The Mechanics of Spinal Manipulation, in Clinical Biomechanics of Spinal Manipulation, eds. Herzog, W.; New York: Churchill Livingstone 2000;(4):92-190.
7. Pickar, J. G. Neurophysiological effects of spinal manipulation. The Spine Journal 2002; 1(2):357-371.
8. Hessell, B. W., Herzog, W., Conway, P. J., McEwen, M. C. Experimental measurement of the force exerted during spinal manipulation using the Thompson technique. J.Manipulative Physiol Ther. 1990; 13(8):448-453.
9. Harms, M. C. , Bader, D. L. Variability of forces applied by experienced therapists during spinal mobilization. Clin.Biomech.(Bristol., Avon.) 1997; 12(6):393-399.
10. Harms, M. C., Innes, S. M., Bader, D. L. Forces measured during spinal manipulative procedures in two age groups. Rheumatology.(Oxford) 1999; 38(3):267-274.
11. Triano, J. , Schultz, A. B. Loads transmitted during lumbosacral spinal manipulative therapy. Spine 1997; 22(17):1955-1964.
12. Lee, R. , Evans, J. An in vivo study of the intervertebral movements produced by posteroanterior mobilization. Clin.Biomech.(Bristol., Avon.) 1997; 12(6):400-408.
13. Keller, T. S., Colloca, C. J., Beliveau, J. G. Force-deformation response of the lumbar spine: a sagittal plane model of posteroanterior manipulation and mobilization. Clin.Biomech.(Bristol., Avon.) 2002; 17(3):185-196.
14. Nathan, M. , Keller, T. S. Measurement and analysis of the in vivo posteroanterior impulse response of the human thoracolumbar spine: a feasibility study. J.Manipulative Physiol Ther. 1994; 17(7):431-441.
15. Cramer, G. D., Gregerson, D. M., Knudsen, J. T., Hubbard, B. B., Ustas, L. M., Cantu, J. A. The effects of side-posture positioning and spinal adjusting on the lumbar Z joints: a randomized controlled trial with sixty-four subjects. Spine 2002; 27(22):2459-2466.
16. Brodeur, R. The audible release associated with joint manipulation. J.Manipulative Physiol Ther. 1995; 18(3):155-164.
17. Cavanaugh, J. M., el Bohy, A., Hardy, W. N., Getchell, T. V., Getchell, M. L., King, A. I. Sensory innervation of soft tissues of the lumbar spine in the rat. J.Orthop.Res. 1989; 7(3):378-388.

18. Pickar, J. G. , McLain, R. F. Responses of mechanosensitive afferents to manipulation of the lumbar facet in the cat. Spine 1995; 20(22):2379-2385.
19. Pickar, J. G. , Wheeler, J. D. Response of muscle proprioceptors to spinal manipulative-like loads in the anesthetized cat. J.Manipulative Physiol Ther. 2001; 24(1):2-11.
20. Avramov, A. I., Cavanaugh, J. M., Ozaktay, C. A., Getchell, T. V., King, A. I. The effects of controlled mechanical loading on group-II, III, and IV afferent units from the lumbar facet joint and surrounding tissue. An in vitro study. J.Bone Joint Surg.Am. 1992; 74(10):1464-1471.
21. Ianuzzi, A., Little, J., Khalsa, P. S. Human Lumbar Facet Joint Capsule Strains during Simulated Spinal Manipulation. Paper presented at: Transactions of the Annual BMES Conference, 10-4-2003, Biomedical Engineering Society, Landover, MD, 31:11.5.3.
22. Ianuzzi, A. Comparison of Human Lumbar Facet Joint Capsule Strains during Impulse Loading versus Physiological Motions. 2003 M.S. Thesis in Biomedical Engineering. Stony Brook University.
23. Ianuzzi, A., Little, J., Chiu, J., Baitner, A, Kawchuk, G., Khalsa, P. S. Human lumbar facet joint capsule strains: I. During physiological motions. The Spine Journal 2004; 4(2):141-152.
24. Little, J., Ianuzzi, A., Chiu, J., Baitner, A, Khalsa, P. S. Human lumbar facet joint capsule strains: II. Alteration of strains subsequent to anterior interbody fixation. The Spine Journal 2004; 4(2):153-162.
25. Panjabi, M. M., Krag, M., Summers, D., Videman, T. Biomechanical time-tolerance of fresh cadaveric human spine specimens. J Orthop.Res. 1985; 3(3):292-300.
26. White, AA , Panjabi, M. M. Clinical Biomechanics of the Spine, Philadelphia:JB Lippincott, 1990.
27. Soderkvist, I. , Wedin, P. A. Determining the movements of the skeleton using well-configured markers. J.Biomech. 1993; 26(12):1473-1477.
28. Winkelstein, B. A., Nightingale, R. W., Richardson, W. J., Myers, B. S. The cervical facet capsule and its role in whiplash injury: a biomechanical investigation. Spine 2000; 25(10):1238-1246.
29. Mansour, M., Spiering, S., Lee, C., Dathe, H., Kalscheuer, A. K., Kubein-Meesenburg, D., Nagerl, H. Evidence for IHA migration during axial rotation of a lumbar spine segment by using a novel high-resolution 6D kinematic tracking system. J Biomech. 2004; 37(4):583-592.
30. Pearcy, M. J. , Bogduk, N. Instantaneous axes of rotation of the lumbar intervertebral joints. Spine 1988; 13(9):1033-1041.
31. Yamashita, T., Minaki, Y., Ozaktay, A. C., Cavanaugh, J. M., King, A. I. A morphological study of the fibrous capsule of the human lumbar facet joint. Spine 1996; 21(5):538-543.
32. Gudavalli, M. R. , Triano, J. J. An analytical model of lumbar motion segment in flexion. J.Manipulative Physiol Ther. 1999; 22(4):201-208.
33. Herzog, W., Kats, M., Symons, B. The effective forces transmitted by high-speed, low-amplitude thoracic manipulation. Spine 2001; 26(19):2105-2110.

34. Gal, J., Herzog, W., Kawchuk, G., Conway, P., Zhang, Y. T. Measurements of vertebral translations using bone pins, surface markers and accelerometers. Clin.Biomech.(Bristol., Avon.) 1997; 12(5):337-340.
35. Gal, J., Herzog, W., Kawchuk, G., Conway, P. J., Zhang, Y. T. Movements of vertebrae during manipulative thrusts to unembalmed human cadavers. J.Manipulative Physiol Ther. 1997; 20(1):30-40.
36. Gal, J. M., Herzog, W., Kawchuk, G. N., Conway, P. J., Zhang, Y. T. Forces and relative vertebral movements during SMT to unembalmed post-rigor human cadavers: peculiarities associated with joint cavitation. J.Manipulative Physiol Ther. 1995; 18(1):4-9.
37. Powers, C. M., Kulig, K., Harrison, J., Bergman, G. Segmental mobility of the lumbar spine during a posterior to anterior mobilization: assessment using dynamic MRI. Clin.Biomech.(Bristol., Avon.) 2003; 18(1):80-83.
38. Colloca, C. J., Keller, T. S., Gunzburg, R. Biomechanical and neurophysiological responses to spinal manipulation in patients with lumbar radiculopathy. J.Manipulative Physiol Ther. 2004; 27(1):1-15.
39. Keller, T. S., Colloca, C. J., Gunzburg, R. Neuromechanical characterization of in vivo lumbar spinal manipulation. Part I. Vertebral motion. J.Manipulative Physiol Ther. 2003; 26(9):567-578.
40. Maigne, J. Y. , Guillon, F. Highlighting of intervertebral movements and variations of intradiskal pressure during lumbar spine manipulation: a feasibility study. J.Manipulative Physiol Ther. 2000; 23(8):531-535.
41. Lee, R. Y. W. , Evans, J. H. Load-displacement-time characteristics of the spine under posteroanterior mobilisation. Australian Journal of Physiotherapy 1992; 38:115-123.
42. Blader, D. L. , Bowker, P. Mechanical characteristics of skin and underlying tissues in vivo. Biomaterials 1983; 4(4):305-308.
43. McLain, R. F. , Pickar, J. G. Mechanoreceptor endings in human thoracic and lumbar facet joints. Spine 1998; 23(2):168-173.
44. Khalsa, P. S., Hoffman, A. H., Grigg, P. Mechanical states encoded by stretch-sensitive neurons in feline joint capsule. J.Neurophysiol. 1996; 76(1):175-187.
45. Khalsa, P. S., Chiu, J. B., Aliberti, N., Sileo, M. Biomechanical evidence for proprioceptive function of lumbar facet joint capsule. Proceedings of the 4th World Congress on Biomechanics 2002; 4:5059.
46. Herzog, W., Scheele, D., Conway, P. J. Electromyographic responses of back and limb muscles associated with spinal manipulative therapy. Spine 1999; 24(2):146-152.
47. Jull, G., Bogduk, N., Marsland, A. The accuracy of manual diagnosis for cervical zygapophysial joint pain syndromes. Med.J Aust. 1988; 148(5):233-236.
48. Haas, M. , Panzer, D. Palpatory diagnosis of subluxation, in Foundations of Chiropractic Subluxation, eds. Gatterman, M. I.; New York, NY: Mosby 1997;56-67.
49. Haas, M., Groupp, E., Panzer, D., Partna, L., Lumsden, S., Aickin, M. Efficacy of cervical endplay assessment as an indicator for spinal manipulation. Spine 2003; 28(11):1091-1096.
50. Beffa, R. , Mathews, R. Does the adjustment cavitate the targeted joint? An investigation into the location of cavitation sounds. J.Manipulative Physiol Ther. 2004; 27(2):e2.

Appendix III. Photogrammetric calibration using a modified DLT-approach

Using the method of Hatze (Hatze, 1988), a modified direct linear transform (DLT) was used to compute object space coordinates from image coordinates. The Matlab program to perform the calibration was written by Tomislav Pribanic, and the Matlab program used to perform object space reconstruction was written by Christoph Reinschmidt. Both programs were obtained from the International Society of Biomechanics website (http://www.isbweb.org/software/movanal.html). Using these programs as a template, a custom program was written in Matlab to perform the modified DLT transform from object space coordinates to image pixel coordinates.

The following summary of the theory underlying the modified DLT approach was obtained from (Hatze, 1988). Theoretically, the object space coordinates (X, Y, Z) of a point P can be related to its image coordinates (η, ζ) appearing on a comparator plane by the following relationship:

$$\begin{bmatrix} -\mu c \\ \eta - \eta_0 \\ \zeta - \zeta_0 \end{bmatrix} = \lambda A \begin{bmatrix} X - X_0 \\ Y - Y_0 \\ Z - Z_0 \end{bmatrix} \qquad \text{Eq. A3.1}$$

where λ is the scale factor for the size reduction of real objects to their image; A (with elements $a_{ij} = a_{ij}(\phi_1, \phi_2, \phi_3)$) denotes the orientation matrix of the object space coordinate system O'X'Y'Z' relative to the image coordinate system $\Omega'\xi'\eta'\zeta'$; (X_0, Y_0, Z_0) are the object space coordinates of the perspective center of a hypothetical camera; μc denotes the principal distance of that hypothetical camera; and (η_0, ζ_0) is the principal point at which the optical axis intersects the comparator plane.

The theoretical image coordinates differ from the observed image coordinates because of errors induced by systematic errors (e.g., non-orthogonality of image axes).

The observed image coordinates (η^*, ζ^*) of a point P and the non-linear distortions $(\Delta\eta, \Delta\zeta)$ can be defined by:

$$\Delta\eta = \eta'(K_1\varepsilon^2 + K_2\varepsilon^4 + K_3\varepsilon^6) + M_1(3\eta'^2 + \zeta'^2) + 2M_2\eta'\zeta' \qquad \text{Eq. A3.2}$$

$$\Delta\zeta = \zeta'(K_1\varepsilon^2 + K_2\varepsilon^4 + K_3\varepsilon^6) + M_2(3\zeta'^2 + \eta'^2) + 2M_1\eta'\zeta' \qquad \text{Eq. A.3}$$

where

$$\eta' = \eta^* - \eta_0 \qquad \text{Eq. A3.4}$$

$$\zeta' = \zeta^* - \zeta_0 \qquad \text{Eq. A3.5}$$

$$\varepsilon^2 = \eta'^2 + \zeta'^2 \qquad \text{Eq. A3.6}$$

K_1, K_2, K_3, denote the coefficients of symmetrical lens distortion, and M_1 & M_2 are the coefficients of asymmetrical lens distortion.

The linear and non-linear image distortions can be expressed as $(\eta - \eta_0)$ and $(\zeta - \zeta_0)$:

$$(\eta - \eta_0) = \lambda_n(\eta^* + \Delta\eta - \eta_0) \qquad \text{Eq. A3.7}$$

$$(\zeta - \zeta_0) = \lambda_\zeta(\zeta^* + \Delta\zeta - \zeta_0) \qquad \text{Eq. A3.8}$$

where λ_η and λ_ζ are the scaling factors of the respective axes.

Substituting Eq. A3.7 and A3.8 in Eq. A3.1, λ can be eliminated, resulting in the following relationships:

$$\eta^* + \Delta\eta - \eta_0 = -\frac{\mu c}{D\lambda_\eta}[a_{21}(X - X_0) + a_{22}(Y - Y_0) + a_{23}(Z - Z_0)] \qquad \text{Eq. A3.9}$$

$$\zeta^* + \Delta\zeta - \zeta_0 = -\frac{\mu c}{D\lambda_\zeta}[a_{31}(X - X_0) + a_{32}(Y - Y_0) + a_{33}(Z - Z_0)] \qquad \text{Eq. A3.10}$$

where

$$D = a_{11}(X - X_0) + a_{12}(Y - Y_0) + a_{13}(Z - Z_0) \qquad \text{Eq. A3.11}$$

By neglecting, at first, the non-linear distortions $\Delta\eta, \Delta\zeta$, equations A3.9 and A3.10 become:

$$\eta^* = \frac{(L_1 X + L_2 X + L_3 Z + L_4)}{G} \qquad \text{Eq. A3.12}$$

$$\zeta^* = \frac{(L_5 X + L_6 X + L_7 Z + L_8)}{G} \qquad \text{Eq. A3.13}$$

where

$$G = L_9 X + L_{10} Y + L_{11} Z + 1 \qquad \text{Eq. A3.14}$$

Equations A3.12-A3.14 demonstrate that once the 11 DLT calibration parameters L_1 through L_{11} are known, the object space coordinates (X, Y, Z) of a point P can be computed if the image coordinates of that point are known for at east two cameras $((\eta_i^*, \zeta_i^*), i = 1,..., \kappa; \kappa \geq 2)$.

During a calibration procedure, control points having known object space coordinates are imaged and their image coordinates recorded. The known object space coordinates and measured image coordinates can be used to compute the DLT parameters L_1 through L_{11}. Rearranging Equations A3.12-A3.14 results in a matrix equation where the unknowns appear as a vector. In conventional DLT calibration, the least-squares technique to compute the DLT parameters from the overdetermined system.

However, Equations A3.12-A3.14 are derived from A3.9-A3.11, and the latter equations contain only ten unknown parameters:

$$\{\eta_0, \zeta_0, -\mu c / \lambda_\eta, -\eta c / \lambda_\zeta, \phi_1, \phi_2, \phi_3, X_0, Y_0, Z_0\},$$

while the DLT parameters comprise a set of 11 constraints. It can be shown that if the transformation matrix A from Eq. A3.1 satisfies the orthogonality condition, then the non-linear relation

$$(L_1L_5 + L_2L_6 + L_3L_7) * (L_9^2 + L_{10}^2 + L_{11}^2) = (L_1L_9 + L_2L_{10} + L_3L_{11}) * (L_5L_9 + L_6L_{10} + L_7L_{11}) \quad \text{Eq. A3.15}$$

must be included as a nonlinear restraint in computing the DLT parameters.

In the algorithm developed by Pribanic (1999), the initial values of the 11 DLT parameters are estimated using the conventional DLT method. For the second and subsequent iterations, the parameter L_1 is set equal to its value from the previous iteration to reduce the system to 10 unknowns. The system is solved for the remaining unknown DLT parameters (L_2 through L_{11}). L_1 for the current iteration is computed based on the nonlinear restraint (Eq. A3.15). The system of equations is solved iteratively until the solution converges satisfactorily. Reconstruction of object space coordinates from known image pixel coordinates (and vice versa) is performed similarly.